Remote Sensing of Environment 242 (2020) 111769

Contents lists available at ScienceDirect

Remote Sensing of Environment

journal homepage: www.elsevier.com/locate/rse

Review

Sea surface salinity estimates from spaceborne L-band radiometers: An overview of the first decade of observation (2010–2019)

N. Reul[a,*], S.A. Grodsky[m], M. Arias[f], J. Boutin[b], R. Catany[f], B. Chapron[a], F. D'Amico[f], E. Dinnat[l], C. Donlon[o], A. Fore[j], S. Fournier[j], S. Guimbard[d], A. Hasson[b], N. Kolodziejczyk[a], G. Lagerloef[i], T. Lee[j], D.M. Le Vine[l], E. Lindstrom[n], C. Maes[a], S. Mecklenburg[h], T. Meissner[k], E. Olmedo[c], R. Sabia[g], J. Tenerelli[d], C. Thouvenin-Masson[b], A. Turiel[c], J.L. Vergely[e], N. Vinogradova[n], F. Wentz[k], S. Yueh[j]

[a] *Ifremer, Univ. Brest, CNRS, IRD, Laboratoire d'Oceanographie Physique et Spatiale (LOPS), IUEM, Brest, France*
[b] *Sorbonne Université, CNRS, IRD, MNHN, Laboratoire d'Océanographie et du Climat: Expérimentations et Approches Numériques (LOCEAN), Paris, France*
[c] *Institut de Ciencies del Mar -CMIMA (CSIC), Barcelona, Spain*
[d] *OCEANDATALAB, Brest, France*
[e] *ACRI-st, Guyancourt, France*
[f] *ARGANS, Plymouth, UK*
[g] *Telespazio-Vega UK Ltd for ESA, ESRIN, Frascati, Italy*
[h] *European Space Agency, ESA-ESRIN, Frascati, Italy*
[i] *Earth and Space Research, Seattle, WA, USA*
[j] *NASA, Jet Propulsion Laboratory, California Institute of Technology, Pasadena, CA, USA*
[k] *Remote Sensing Systems, Santa Rosa, CA, USA*
[l] *NASA Goddard Space Flight Center, Greenbelt, MD, USA*
[m] *Department of Atmospheric and Oceanic Science, University of Maryland, College Park, MD, USA*
[n] *NASA Headquarters, Washington, DC, USA*
[o] *European Space Agency, ESA-ESTEC, Netherlands*

ARTICLE INFO

Edited by Menghua Wang

Keywords:
Sea surface salinity
Ocean microwave remote sensing
Radiometer
L-band
SMOS
Aquarius/SAC-D
SMAP

ABSTRACT

Operated since the end of 2009, the European Space Agency (ESA) Soil Moisture and Ocean Salinity (SMOS) satellite mission is the first orbiting radiometer that collects regular and global observations from space of two Essential Climate Variables of the Global Climate Observing System: Sea Surface Salinity (SSS) and Soil Moisture. The National Aeronautics and Space Administration (NASA) Aquarius mission, with the primary objective to provide global SSS measurements from space operated from mid-2011 to mid-2015. NASA's Soil Moisture Active-Passive (SMAP) mission, primarily dedicated to soil moisture measurements, but also monitoring SSS, has been operating since early 2015. The primary sensors onboard these three missions are passive microwave radiometers operating at 1.4 GHz (L-band). SSS is retrieved from radiometer measurements of the sea surface brightness temperature (T_B). In this paper, we first provide a historical review of SSS remote sensing with passive L-band radiometry beginning with the discussions of measurement principles, technology, sensing characteristics and complementarities of the three aforementioned missions. The assessment of satellite SSS products is then presented in terms of individual mission characteristics, common algorithms, and measurement uncertainties, including the validation versus in situ data, and, the consideration of sampling differences between satellite SSS and in situ salinity measurements. We next review the major scientific achievements of the combined first 10 years of satellite SSS data, including the insights enabled by these measurements regarding the linkages of SSS with the global water cycle, climate variability, and ocean biochemistry. We also highlight the new ability provided by satellites to monitor mesoscale and synoptic-scale SSS features and to advance our understanding of SSS' role in air-sea interactions, constraining ocean models, and improving seasonal predictions. An overview of satellite SSS observation highlights during this first decade and upcoming challenges are then presented.

* Corresponding author.
E-mail address: Nicolas.Reul@ifremer.fr (N. Reul).

https://doi.org/10.1016/j.rse.2020.111769
Received 8 October 2019; Received in revised form 2 March 2020; Accepted 10 March 2020

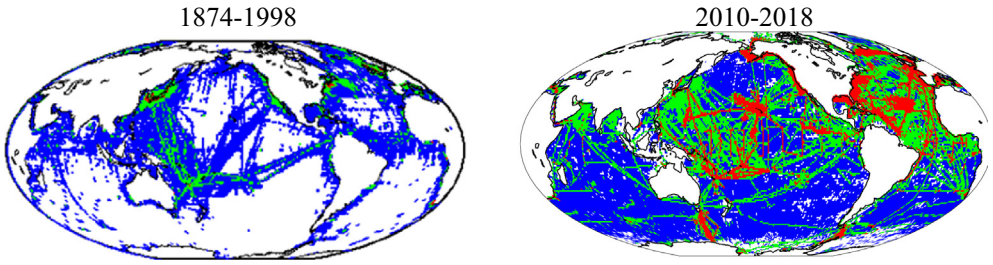

Fig. 1. (Left) Number of historical in situ SSS observations over 125 years from 1874 to 1998 per 1° square (from Bingham et al., 2002). Note that only few WOCE lines were available into the NODC database used to build the density map (personal exchanges with F. Bingham). (Right) Number of historical in situ SSS observations per 1° square during the first 9 years of the satellite salinity era from 2010 to 2018. Blue, > 10 observations; green, > 100 observations; and red, > 1000 observations. No color means < 10 observations. (For interpretation of the references to color in this figure legend, the reader is referred to the web version of this article.)

1. Introduction

Ocean salinity is a key physical-chemical variable that critically contributes to the density-driven global ocean circulation and the Earth's climate (Siedler et al., 2001). The SSS is affected by (and thus reflects) the air-sea freshwater fluxes (Wust, 1936; Schmitt, 2008; Durack et al., 2012; Skliris et al., 2014; Zika et al., 2015), ice formation/melting, river runoff, horizontal advection and vertical exchanges through mixing and entrainment. It also provides fundamental information for ocean bio-geochemistry through its links with the carbonate system (Land et al., 2015, 2019; Fine et al., 2017). Stable fresh surface salinity layers (such as river plumes, rain-induced lenses) on top of saltier and denser deep waters can inhibit the upper-ocean mixing generated by intense atmospheric events (e.g., wind bursts, tropical cyclones) due to so-called barrier layer effect (e.g., Lukas and Lindstrom, 1991; Balaguru et al., 2012). This suggests that mixed layer salinity can actively impact air-sea interactions from local to synoptic scales. Given its importance for many key ocean and climate processes, the SSS has been recognized as an Essential Climate Variable (ECV) by the Global Climate Observing System (GCOS) program.

Bingham et al. (2002) examined the global distribution of historical (1874–1998) in situ SSS observations measured at 5 m or less in depth from the World Ocean Database 1998 (WOD98). Their results give a good indication of how poorly SSS was sampled by the end of the 1990s (Fig. 1), despite a peak period of ocean sampling (including near surface salinity) during the World Ocean Circulation Experiment (WOCE, 1990–1998). This is especially true given that about 28% of WOD98 measurements are located within coastal waters.

This analysis was a strong driver and justification for the need for increased efforts in obtaining SSS measurements. It has been illustrated that 27% of non-Arctic 1° squares have no SSS measurements at all (Bingham et al., 2002) while 70% of squares had 10 or fewer measurements in the 125 years. By the end of the 1990s, the global large scale time mean SSS field was known but with almost unexplored interannual and decadal variations (e.g., O'Kane et al., 2016). The Global Ocean Data Assimilation Experiment (GODAE) group, therefore, estimated that it would be necessary to develop global SSS measurements from both in situ sensor networks and dedicated satellite missions to reach an accuracy of about 0.1–0.2 pss[1] at monthly and 100 × 100 km^2, or 10-day and 200 × 200 km^2 scales.

Tremendous efforts to reach this goal using in situ sensor networks have been carried out by the ocean science community since the early 2000s. At global scale, the large increase in salinity data sampling (Fig. 1) is dominantly associated with the invention and deployment of the Argo profiler network. Since reaching its full planned capacity in 2007, the network includes ~3000 Argo floats in the global Ocean providing at least one salinity cast every 10 days in a 3°x3° cell (see Argo, 2000). In addition to Argo floats which profile to the top 2 km of the global ocean column, near surface salinity is monitored by thermosalinographs (TSG) on board numerous ships of opportunity and research vessels. These TSGs are installed and maintained on board ships via international programs such as the Global Ocean Surface Underway Data (GOSUD; Alory et al., 2015) and the Shipboard Automated Meteorological and Oceanographic System (SAMOS; Smith et al., 2009), as well as a growing number of deployments of surface drifters equipped with salinity sensors.

Despite its oceanographic importance, SSS is an ocean ECV that only started to be estimated from space about ten years ago (Fig. 2) with the launch of the Soil Moisture and Ocean Salinity (SMOS) mission by the European Space Agency (ESA) in November 2009. The SMOS mission was then followed by the NASA/CONAE Aquarius/SAC-D mission also focused on the sea surface salinity. Both missions had an overlapping period between June 2011 and mid-2015. Next came the NASA Soil Moisture Active-Passive (SMAP) mission launched in early 2015, which also monitors SSS. SMOS and SMAP operation periods overlapped with Aquarius only during about four months (February to June 2015). The primary sensors onboard these three missions are L-band microwave radiometers operating at ~1.4 GHz (wavelength = 21 cm). When accurate corrections for external contributions to the measured radiometer signal are applied (e.g., radiation from the Sun and celestial radio sources, reflection/emission due to sea surface roughness, and temperature), the SSS can be estimated from L-band brightness temperature T_B (Font et al., 2004; Lagerloef et al., 1995). The feasibility of the measurement of SSS at L-band was demonstrated in the 1970s in a number of field campaigns from aircraft (Droppelman et al., 1970), from a bridge which spans the Cape Cod canal (Swift, 1974), and even with a satellite radiometer from the short-lived (2-week) Skylab S-194 mission (Lerner and Hollinger, 1977).

It took > 40 years after the aforementioned pioneer experiments to develop and implement instruments to measure SSS regularly from space with sufficient accuracy and spatial resolution to address the GODAE recommendation. Two major technological factors limit L-band SSS measurements from space. First, at low microwave frequencies (decimeter wavelengths), classical radiometer sensors require large antenna size of ~3 to 8 m in diameter to meet a useful spatial resolution on the ground (100–150 km at most, 30–50 km wished for). Such large antenna technologies were not available before the late 1990s. Second, while being optimal in low microwave frequencies (see Fig. 3), the sensitivity of the sea surface brightness temperature to salinity at 1.4 GHz and vertical (VV) polarization varies only between $\partial T_B/\partial SSS$ ~ −0.5 to −1 K/pss for incidence angles from 0° to 60° at characteristic ocean conditions (SSS = 35pss and Sea Surface Temperature (SST) = 15 °C). This sensitivity to SSS remains relatively small compared to (i) noise characteristics of available radiometers (~0.3 to 2 K) and (ii) the small range of natural variability of SSS in the open ocean (32 to 38 pss). Finally, as illustrated in Fig. 3b, $\partial T_B/\partial SSS$ also decreases with decreasing SST from ~ −0.7 K/pss at 30 °C to ~ −0.2 K/pss at 0 °C making SSS estimation in the high latitude cold waters even more challenging than in the tropics. Given the sensitivity of T_B to salinity at

[1] Practical Salinity Scale 1978 (PSS-78) are used, following UNESCO guidelines "*The Practical Salinity Scale 1978 and the International Equation of State of Seawater 1980.*" Although salinities measured using PSS-78 do not have units, the suffix "pss" is sometimes used in the text and figures to distinguish the values of salinity, rates, and variance.

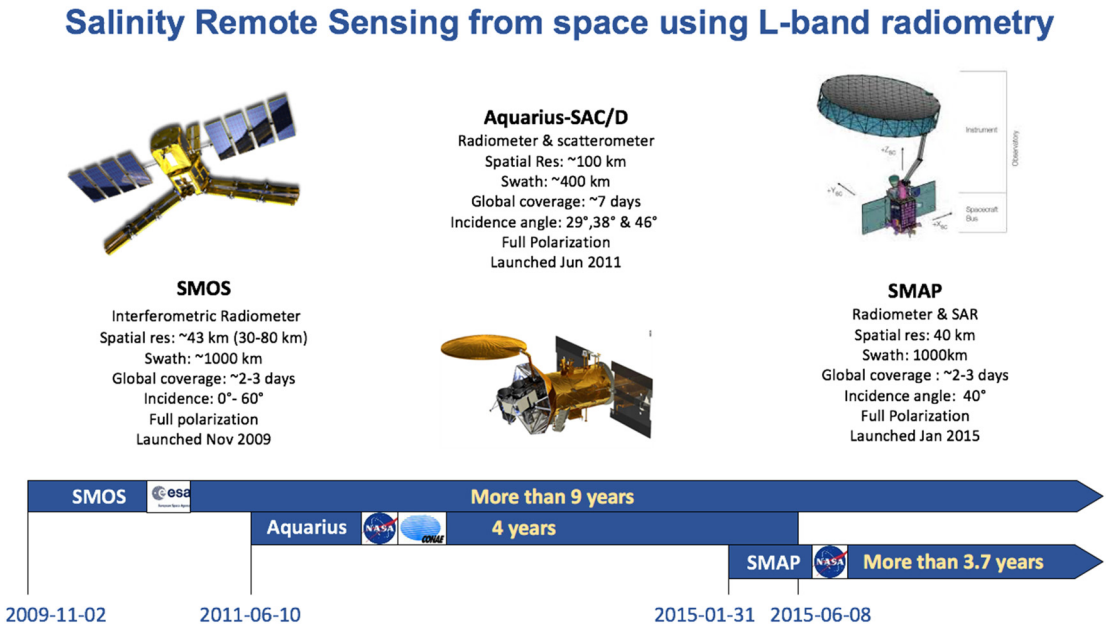

Fig. 2. Overview of the timeline of satellite salinity missions.

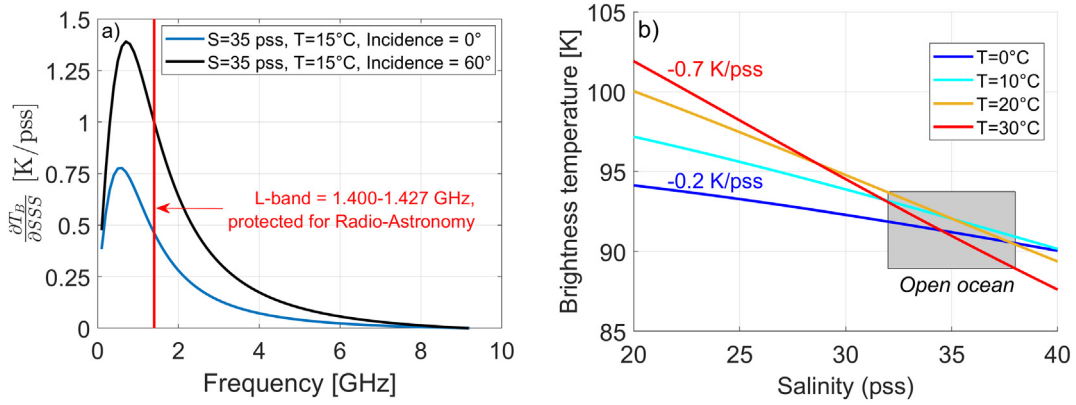

Fig. 3. (a) sensitivity of the ocean surface microwave brightness temperature to Salinity (First Stokes parameter) as a function of electromagnetic frequency and incidence angle (blue curve = 0°, black curve = 60°) and for a water body with salinity of 35 pss and temperature of 15 °C. (b) Brightness temperature ($(T_H + T_V)/2$) changes at 1.4 GHz and nadir as a function of salinity (x-axis) and temperature (colors). The gray domain indicates the range of SSS values mostly encountered in the open ocean. (For interpretation of the references to color in this figure legend, the reader is referred to the web version of this article.)

1.4 GHz, very low noise radiometers and/or a large number of T_B observations for a given ocean scene within short integration times (~a few seconds) are required for accurate SSS estimations.

Therefore, salinity satellite mission objectives are generally expected to be reached for SSS products obtained after spatio-temporal averaging of in-swath instantaneous data. SMOS, Aquarius, and SMAP missions have provided the first SSS data from space now spanning 10 years (2010–2019). This paper aims to provide an overview of what was learned from each of these missions and also from their respective differences and complementarities. A historical review of SSS remote sensing from L-band radiometers is first presented. We describe the technical characteristics of each of the three satellite missions. The measurement principles and algorithms are then reviewed. The quality status of satellite SSS products from the three missions is further presented in terms of individual mission characteristics, common algorithms, and measurement uncertainties, including the validation against in situ data and the representativeness of these comparisons. We then review the major scientific achievements of these first 10 years of data, including the insights into the linkages between SSS and the global water cycle, the imprints of large-scale climate variability on SSS, and the effects of salinity on ocean bio-geochemistry. We also highlight the new ability provided by satellite SSS to monitor mesoscale to synoptic scale processes, better understand SSS role in air-sea interactions, constrain ocean models, and improve seasonal/inter-annual predictions. Finally, we provide a synthesis of this initial satellite SSS observation era and its scientific discoveries together with discussions of upcoming challenges. A list of all abbreviations and acronyms used in the paper is given in the Appendix B.

2. Historical heritage

In the late 1960s, Sirounian (1968) and Paris (1969) recognized that ocean surface microwave emission in the 1 to 3 GHz range had measurable sensitivity to changes in ocean SSS. The first airborne salinity measurements were demonstrated in 1970 by Droppelman et al. (1970). Combining aircraft mounted 1.4 GHz microwave and 11 μm infrared radiometers, they were able to observe strong SSS gradients near the mouth of the Mississippi River, and thus demonstrate the feasibility of 1.4-GHz passive radiometers to detect sea water salinity gradients.

Multi-frequency (L-, X- and K-bands) microwave radiometer observations conducted by Hollinger (1971) from a research tower located

off the island of Bermuda revealed the potential effect of sea surface roughness on L-band T_B for wind speed conditions varying from calm to 15 m/s. Thomann (1976) used a system similar to Droppelman et al. (1970) to map ocean surface salinity in the Gulf of Mexico. As reviewed in Goodberlet et al. (1997), these early instruments could achieve an acceptable measurement accuracy only by averaging over time periods from 12 to 16 s. The averaging time was later reduced below 1 s using a NASA Langley built precise radiometer system (Blume et al., 1978; Blume and Kendall, 1982) operating at 1.4 GHz (L-band) and 2.65 GHz (S-band). Its improved noise characteristics (and lower integration times) allowed improvement in spatial resolution and measurements in the Chesapeake Bay SSS that resolved ~0.5 km spatial scales. The dual-frequency radiometer system was also successfully operated from an aircraft (Kendall and Blanton, 1981) to measure quasi-synoptic salinity changes induced by the Savannah River plume along the coast of Georgia.

A key model component for the salinity retrieval algorithm from microwave radiometer data is the model for the sea water dielectric constant, ϵ. The semi-empirical Debye model was first proposed by Stogryn (1971) and re-analyzed by Klein and Swift (1977) to include new S-band and L-band data from the NASA 2-band radiometer. Shutko et al. (1982) further examined and refined the dependencies of ϵ on electromagnetic frequency, water temperature, and salinity. In addition, near nadir L-band measurements from the Bering Sea aircraft experiments as reported by Webster et al. (1976) allowed for better characterization of wind speed dependence of the surface emissivity.

First attempts to measure SSS from space took place in 1968 aboard the Soviet Cosmos 243 and in 1973 aboard the Skylab S-194 satellite missions (Lerner and Hollinger, 1977). They utilized nadir looking L-band horizontal (HH) microwave radiometers with 3 dB beam width of 15° corresponding to ~110 km ground footprint. Unfortunately, only a very limited amount of L-band radiometer data were collected and there were no in situ measurements available to validate SSS retrievals estimated from the satellite data. Nevertheless, the retrieved SSS was found correlating with climatological in situ salinity. Overall, these experiments showed that open sea SSS (i.e., away from the land and coasts) could be measured with an accuracy of ~2 pss, a promising early result.

Based on these first aircraft and satellite experiments, Swift and McIntosh (1983) suggested a revised satellite concept to achieve an ideal precision of about 0.25 pss with a footprint spatial resolution of ~100 km. However, at that time, space agencies were primarily devoting efforts to develop missions to measure surface temperature (Advanced Very High Resolution Radiometers (AVHRRs) and Along-Track Scanning Radiometers (ATSRs); e.g. see the overview given in Merchant et al., 2019), surface dynamic topography (Geosat (GEOdetic SATellite), Cheney et al., 1989), wind stress (SEASAT A Scatterometer (SASS), Brown, 1983), ocean color (Coastal Zone Color Scanner (CZCS), Hovis et al., 1980), and sea ice (scanning multichannel microwave radiometer (SMMR), Gloersen et al., 1984). Mainly because of the technological challenges associated with the launch of sensors with large antenna size and the need for high radiometric sensitivity, salinity remote sensing was considered too costly and not given a high priority in the early 1980s.

Interest in salinity remote sensing was renewed in the late 1980s with the development of an airborne demonstration instrument called the Electrically Scanning Thinned Array Radiometer (ESTAR), which was operated at 1.4 GHz and used the concept of aperture synthesis (Le Vine et al., 1990) allowing an increase in cross-track spatial resolution. Small salinity variations typical of the open ocean were retrieved from the data acquired by the ESTAR interferometer during flights across a coastal current in Delaware and the Gulf Stream (Le Vine et al., 1998). Such a system demonstrated that it was feasible to achieve high spatial and radiometric resolution at a reasonable cost for a potential 1.4 GHz satellite radiometer design.

By the mid-1990s, the Scanning Low Frequency Microwave Radiometer (SLFMR) was built (Goodberlet and Swift, 1993) based on the similar concept as the ESTAR but with an improved radiometric resolution and adapted for light aircraft. Salinity in coastal and estuarine waters on the U.S. Atlantic coasts, as well as in the Australian Great Barrier reef waters have been mapped successfully using the SLFMR data acquired during several airborne campaigns (Robinson, 1994; Le Vine et al., 1998; Miller et al., 1998; Burrage et al., 2003; Miller and Goodberlet, 2004; Perez et al., 2006). A detailed review of remote sensing of SSS in coastal waters is provided in Klemas (2011).

A Passive-Active L-band System (PALS) (Wilson et al., 2003) providing coincident scatterometer and radiometer airborne L-band data was developed to better characterize the sea surface roughness impact on L-band T_B. This instrument was deployed on ocean flights across the Gulf Stream in an attempt to illustrate the use of active scatterometer data to correct the impact of surface roughness on passive radiometer data (Yueh et al., 2001). The PALS design and data provided the basis for the NASA Aquarius and SMAP instrument designs.

In 1995, during the “Soil Moisture and Ocean Salinity” Workshop organized at the ESA ESTEC (European Space Research and Technology Centre, Noordwijk, the Netherlands), possible techniques to remotely measure SSS from space were discussed. The two most suitable approaches were identified to be L-band microwave radiometry using either real or synthetic, aperture antenna design. The use of a real aperture antenna with moderate size (diameter $<$ 3 m) eases sensor integration into a launch vehicle and better fulfills satellite weight constraints but results in lower spatial resolution on the ground. This option was realized for the Aquarius mission with a moderately large antenna (reflector diameter ~2.5 m) used in the push broom mode (Fig. 4). Another concept was realized for the SMAP mission, which has a relatively large deployable mesh antenna reflector of 6 m in diameter (Fig. 5). Both Aquarius and SMAP instruments were designed with combined active and passive measurements.

The second approach involves the use of interferometric radiometers with a synthetic aperture antenna allowing T_B measurements at higher spatial resolution than with a real-aperture antenna of the same size. The ESTAR interferometric 1-D imaging concept evolved into a 2-D imager in the mid-1990s (Goutoule et al., 1996). Its airborne prototype was made and operated (Bayle et al., 2002) and then further evolved into the Microwave Imaging Radiometer with Aperture Synthesis (MIRAS), the instrument carried by the SMOS mission (Fig. 6).

Technical characteristics of each of the three first satellite SSS missions are described in the following.

3. SMOS, Aquarius, and SMAP technical specifications

The SMOS satellite mission (Kerr et al., 2010; Mecklenburg et al., 2012) follows a sun-synchronous polar orbit (equator crossing time of 6 AM (ascending)/6 PM (descending)). MIRAS is the first 2D L-Band interferometric radiometer operated from an orbiting platform. The instrument measures so-called ‘visibilities’ that are complex cross-correlations between signals collected by pairs of antennae located within an array of 69 receivers installed on a deployable Y-shape structure, each arm of the former being about 4 m long (see Fig. 6). Two-dimensional images of the earth emitted T_B can be reconstructed from the visibilities (through an inverse spatial Fourier transform of the latter in the ideal case when decorrelation effects are negligible and all the antennas have the same voltage radiation pattern).

As a result, MIRAS data processing provides T_B images (or ‘snapshots’) acquired along the orbit track after temporal integration (from ~1.2 to 3.6 s, depending on the polarized acquisition cycle) and, when combined, forms a swath on the ground of approximately 1200 km width (Fig. 6).

A T_B image on a distorted hexagonal grid is reconstructed for each integration cycle with spatial resolution varying within the Field Of View (FOV) from ~35 to 60 km (43 km on average) and with varying

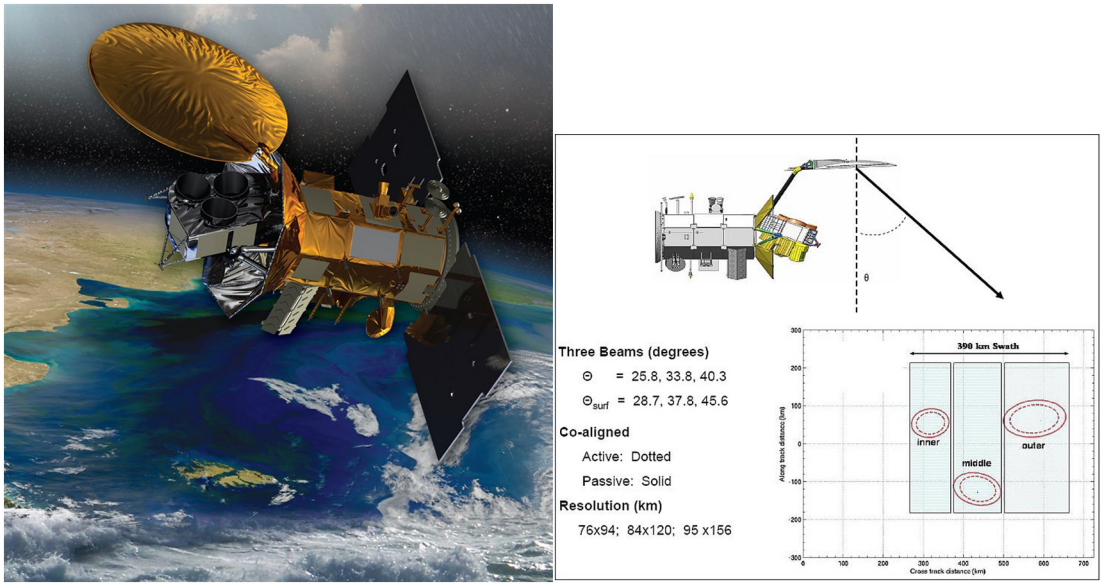

Fig. 4. (Left) Artistic view of Aquarius mission, (Right) schematic indicating the ~390 km wide swath formed by the three radiometer and scatterometer beams of Aquarius.

earth incidence angle ranging from 0° at the sub-satellite point, to 40°-60° at the FOV borders. As the satellite moves, an earth target is imaged multiple times at different observation angles that depend on the Earth target cross-track location. The four Stokes parameters can be reconstructed from the samples of the four polarimetric visibilities that are sequentially measured by MIRAS using a polarization-switching scheme. The radiometric resolution ranges from ~2.6 K at boresight to 5 K at the swath edges. Despite the almost 1200 km swath-width, the useful domain of the swath for SSS retrieval is usually limited to the alias-free part of the reconstructed brightness temperature images which extends about ± 400 km across-track (see Fig. 6, black domain) because the number of multiple-angle T_B observations and the signal to noise ratio are too small to accurately infer SSS outside of this domain.

The NASA/CONAE Aquarius/SAC-D (Lagerloef et al., 2008) mission launched on June 10, 2011, is based on a measurement approach that is different from that of the SMOS satellite. The Aquarius payload includes

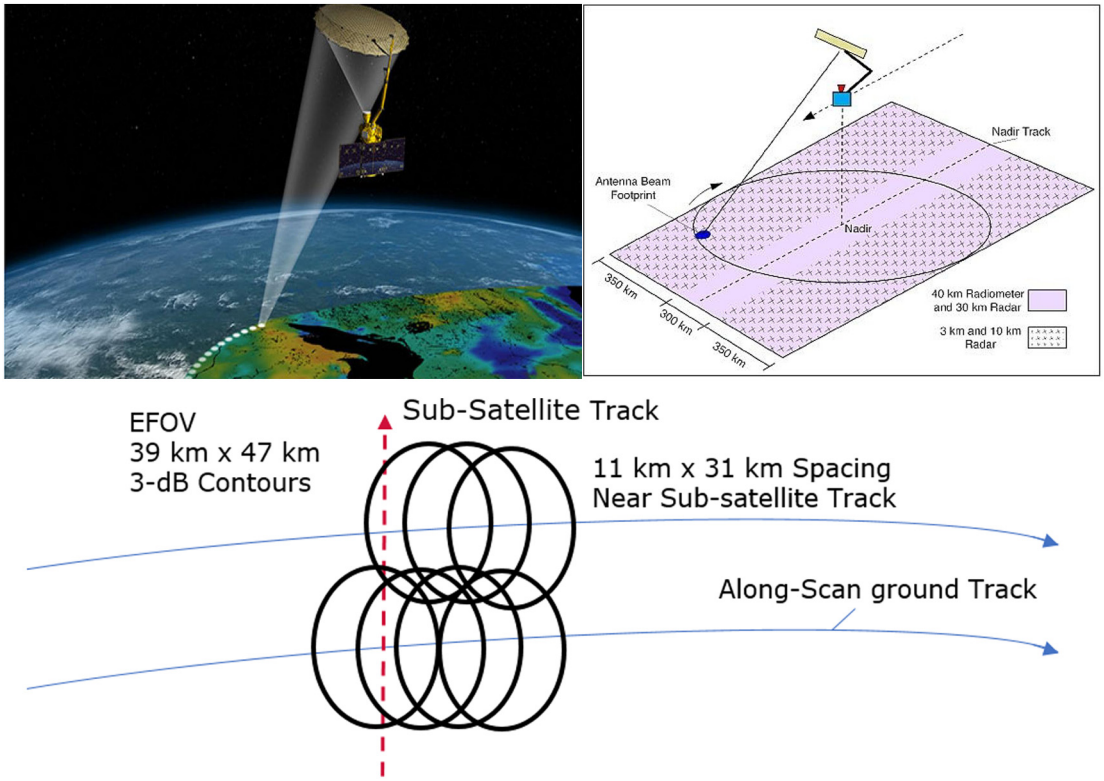

Fig. 5. (Top Left) Artistic view of NASA/SMAP mission, (Top Right) schematic indicating the ~1000 km wide swath formed by the scanning radiometer and radar beams of SMAP. (Bottom) Radiometer Extended FOV spacing. The sub-satellite point is moving in the direction of the red dashed arrow. The blue curves indicate the azimuthal scanning directions and the black ellipses illustrate the successive 3-dB footprint of the radiometer in that direction. (For interpretation of the references to color in this figure legend, the reader is referred to the web version of this article.)

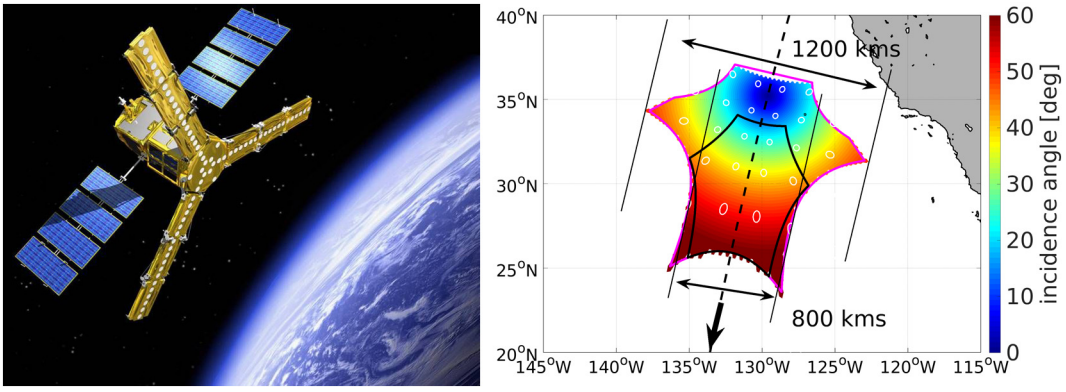

Fig. 6. (Left) Artistic view of SMOS sensor, (Right) shape of a snapshot brightness temperature image as reconstructed from SMOS observations, the color indicates the varying Earth incidence angle, the thick dash line and large arrow indicate the sub-satellite track and satellite propagation direction, respectively. The widths of the extended FOV and alias-free FOV are indicated by the pink and black hexagonal shapes, respectively. White ellipses give an indication of the varying footprint sizes from about 35 km at boresight to ~60 km at the FOV borders. (For interpretation of the references to color in this figure legend, the reader is referred to the web version of this article.)

four L-band sensors: three radiometers (center frequency of 1.413 GHz) and a scatterometer (center frequency of 1.26 GHz). The instrument antenna is an offset parabolic reflector with a diameter of 2.5-m diameter equipped with three feed horns (Fig. 4). The three beams image in pushbroom fashion and point ~90° with respect to the spacecraft heading. The local incidence angles at the Earth's surface at beam centers are about 29, 38 and 46°, respectively (Le Vine et al., 2007).

A dedicated radiometer was operated for each feed horn together with a scatterometer that cycled among the three feeds. The 3 dB beam width is similar for the radiometer and scatterometer and the footprint is in the form of ellipses with axes (minor times major) of size ranging from 76 × 94 km for the inner beam to 96 × 156 km for the outer beam. Combined, the three beams formed a swath of about 390 km width. All linearly polarized channels complied with the required Noise Equivalent Differential Temperature (NEDT) of 0.16 K. The NEDT slightly increased to 0.22 K for the third Stokes parameter. The equatorial crossings of Aquarius' orbit were at 6 PM (ascending) and 6 AM (descending) local time, the opposite of SMOS. A hardware failure occurred onboard the Aquarius/SAC-D on June 7, 2015, which unfortunately resulted in the mission operation end. The full Aquarius dataset record spans the period from 8/25/2011 to 6/7/2015 (i.e., a full 3 years and 9 months period).

The SMAP instrument architecture (Entekhabi et al., 2014) is a conically scanning, wide swath single channel L-band radiometer. SMAP includes a radar and radiometer, both operating in the L-band at a center frequency of 1.26 GHz and 1.41 GHz, respectively. Both instruments share a single feedhorn and a large parabolic mesh reflector (Fig. 5) 6 m in diameter and offset from nadir. The Earth surface is scanned at a constant incidence angle at the spacecraft of approximately 40° through the rotation of the reflector around the nadir axis and at a speed of 14.6 rpm.

This is the first time such a large rotating antenna has been used for Earth observations and it marks a significant technological milestone. A full 360° scan is obtained from SMAP in < 5 s so that the radiometer observes each ground location in both forward (fore) and backward (aft) direction. Both fore- and aft- measurements are acquired within a couple of minutes and can be combined to derive a more robust SSS retrieval. The satellite was launched early in 2015 into a 685 km near-polar, sun-synchronous orbit with an 8-day repeat cycle and Equator crossings at 6 PM (ascending) and 6 AM (descending) local time. The SMAP radiometer provides T_B data within ~1000-km wide swath with a spatial resolution of about 40 km (see Fig. 5), and the instrument almost fully covers the globe within 3 days. The radar, unfortunately, stopped transmitting mid 2015 due to an anomaly in the high-power amplifier. The primary requirement of SMAP is to provide estimates of soil moisture in the top 5 cm of soil with an accuracy of 0.04 cm^3/cm^3 volumetric soil moisture. This requires a relatively low radiometric accuracy for the radiometer of about1 Kelvin. Note that Aquarius antenna emissivity was negligibly small while the SMAP mesh reflector emissivity is about 0.2%, which is small enough and thus only a relatively minor correction is needed for salinity retrieval.

The first 10 years of SSS measurements from space have successfully explored different technological approaches to sensor design (pushbroom, interferometer, and conical scanner). Depending on antenna aperture implementation and size, the spatial resolution of the SMOS and SMAP (~40 km) is a factor of 2–3 higher than that of the Aquarius (~100 km - 150 km).

Each ground location is observed by SMOS under a wide range of incidence angles as the spacecraft moves forward, while Aquarius and SMAP observe ground targets at approximately fixed incidence angles. For each ground point, SMOS SSS is estimated from a large number of T_B measurements (~200). SMAP provides both fore- and aft-looking observations for each in-swath ground point.

Thanks to their large swaths, the SMOS and SMAP provide nearly global coverage in approximately 3 days, while 7 days are needed in case of the Aquarius (e.g., see Fig. 7). Large swath radiometers can thus provide more frequent monitoring of strong SSS contrasts in highly dynamical oceanic zones. However, Aquarius offers some advantages over SMOS and SMAP because of significantly lower radiometric noise (~0.12 K) in comparison with the SMOS (from ~2.6 K to 5 K) and the SMAP (~1 K). In addition, the simultaneous Aquarius scatterometer and radiometer acquisition significantly improves the sea surface roughness correction and provides more accurate individual SSS measurements. For this correction (see Section 4), SMOS and SMAP retrieval algorithms rely on external auxiliary wind speed data to indirectly characterize the sea surface roughness state in the radiometer footprint.

Finally, the L-band window used is a frequency range protected for passive observations since the 1960s under International Telecommunication Union (ITU) Radio Regulations. However, SMOS measurements first revealed that man-made sources emit above legal thresholds in this part of the spectrum, thus interfering with the satellite observations. Such Radio Frequency Interferences (RFI) are frequent near land, and result in loss of data or introduction of errors in the retrieved SSS. Several approaches have been developed by the SMOS team and implemented in the image reconstruction processing to mitigate the measurement contamination by RFI (e.g. Oliva et al., 2016). While most RFI sources are located on the land, they often induce strong perturbation at distant locations over the ocean because of large sidelobes in the impulse response of the reconstructed T_B due to a

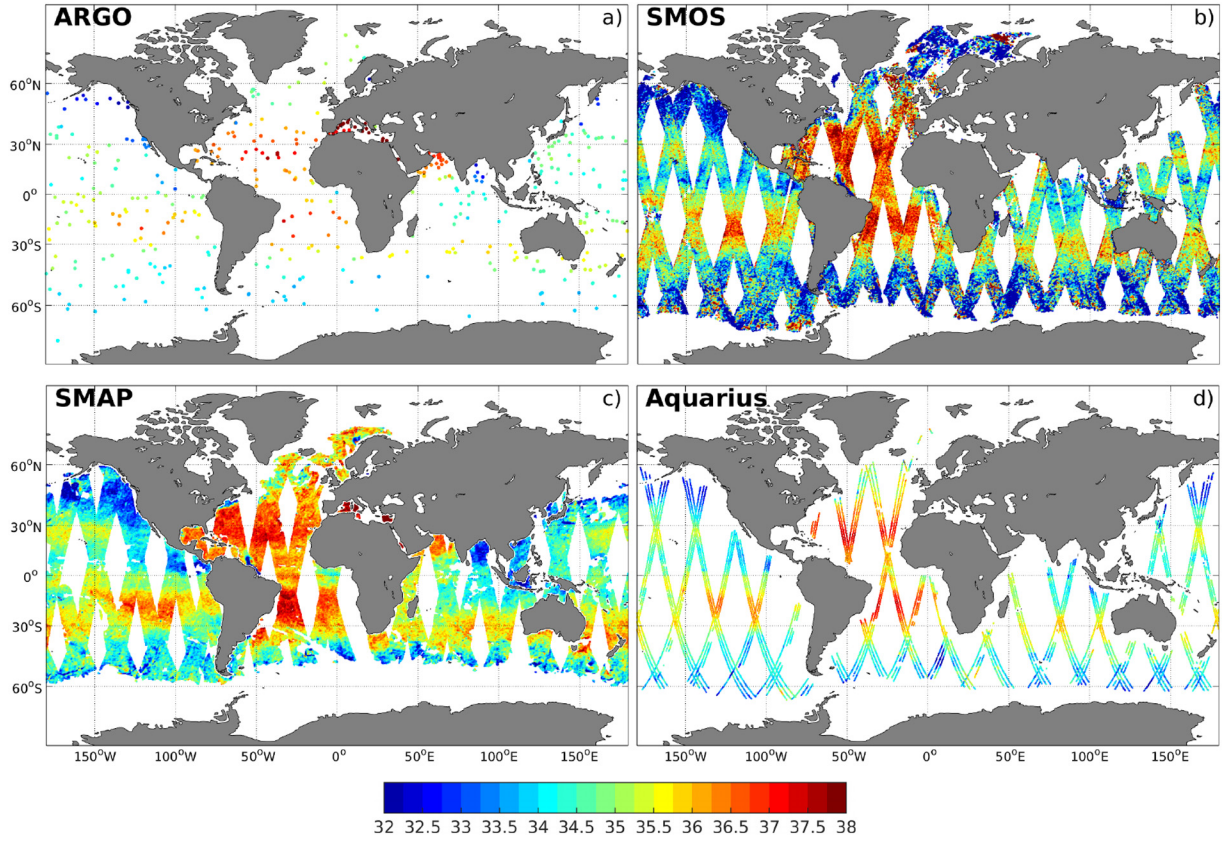

Fig. 7. Daily sampling of the global SSS field by (a) Argo floats upper-level measurements (depth less or equal to 5 m), (b) SMOS, (c) SMAP and (d) Aquarius satellite missions on 15 May 2015.

Gibbs-like phenomena in the impulse response function of the instrument. These strong sources can contaminate the reconstructed brightness images and the retrieved SSS, even in purely open ocean scenes. Taking advantage of the first experience of the SMOS, the Aquarius instrument design included an RFI filtering processing based on the high sampling rate of the radiometer (Misra and Ruf, 2008). A "glitch" detection algorithm is used to remove anomalous outliers from the ensemble of T_B samples which are acquired every 10 milliseconds (and averaged to produce a datum each 1.44 s) (Vine et al., 2014). The SMAP radiometer includes dedicated special onboard hardware (Piepmeier et al., 2016): a digital backend which enables a variety of RFI detection and associated filtering strategies (Mohammed et al., 2016). In parallel, significant efforts by space agencies have resulted in the considerable reduction in RFI emissions through coordinated approach within the regulations of the ITU. Many operators of high-power terrestrial radar systems were unaware of out-of-band emissions and were able to rectify their systems. However, in some areas of the world (e.g., Asia) further progress is still required to eliminate RFI in the L-band.

4. Basic principles of salinity remote sensing

A brief background of the physics underlying the measurement of salinity using microwave radiometry and of the specific issues associated with estimating salinity from space are presented in this section.

4.1. SSS retrieval over a specular sea surface

The dependence of *TB* on SSS is contained in the emissivity, *e*: TB = T x *e*, where T is the sea surface temperature. The emissivity is a quantity that depends on physical and chemical properties of the water (e.g. salinity and temperature), observational conditions (incidence angle, electromagnetic frequency, polarization), as well as sea surface roughness. For a perfectly flat ocean surface with salinity, S, temperature, T, and observed at incidence angle θ, the emissivity at polarization, p (horizontal or vertical), and electromagnetic frequency, f, (note that we quote the center of a microwave frequency bandwidth associated with a given radiometer) is given by Peake (1959):

$$e_p(\theta,f,S,T) = 1 - |R_p(\theta,f,S,T)|^2 \quad (1)$$

where R_p is the Fresnel reflection coefficient given by:

$$R_v(\theta,f,S,T) = \frac{\sqrt{\{\varepsilon_{sw} - \sin^2\theta\}} - \varepsilon_{sw}\cos\theta}{\sqrt{\{\varepsilon_{sw} - \sin^2\theta\}} + \varepsilon_{sw}\cos\theta} \text{ for vertical polarization,} \quad (2)$$

and,

$$R_h(\theta,f,S,T) = \frac{\sqrt{\{\varepsilon_{sw} - \sin^2\theta\}} - \cos\theta}{\sqrt{\{\varepsilon_{sw} - \sin^2\theta\}} + \cos\theta} \text{ for horizontal polarization.} \quad (3)$$

In the expression above, $\varepsilon_{sw}(f, S, T)$ is the dielectric constant of sea water. In its simplest form, SSS remote sensing, therefore, consists of measuring the L-band TB together with SST. The intersection of the two values on a graph such as shown in Fig. 3b can be used to retrieve SSS. It is also important to note that the penetration depth of electromagnetic wave into the sea water (defined as the e-folding attenuation of the energy flux transported by electromagnetic radiation into water, see Ulaby et al., 1986) is < 1 cm at 1.4 GHz for typical open ocean salinity and temperature. Given that the majority of in situ measurements of SSS are obtained at depth ranging from 0.5 to 20 m (e.g., Argo floats, TSG, surface drifters, etc.), understanding the vertical distributions of salinity in the upper ocean is critical for many applications. These applications include the assimilation of satellite SSS in numerical ocean models which requires dedicated treatment of shallow stratifications (Large and Caron, 2015; Fine et al., 2015) and the validation of satellite SSS with in situ data (Boutin et al., 2016).

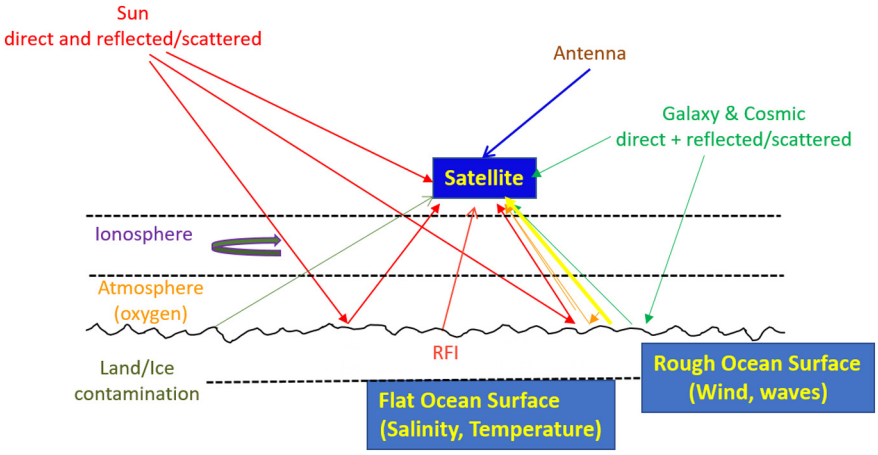

Fig. 8. Signals received by a Space borne L-band radiometer.

There are also other issues that complicate the remote sensing of salinity from space. Several geophysical parameters other than sea-water salinity and temperature contribute significantly to L-band T_B measured by satellite sensors (e.g., see Yueh et al., 2001; Font et al., 2004). These contributions need to be accurately known and used in corrections of measured antenna T_B to properly retrieve SSS. As illustrated in Fig. 8, they include: the direct and earth-reflected solar and sky emission (Le Vine et al., 2005; Reul et al., 2007, 2008a, 2008b; Tenerelli et al., 2008; Dinnat and Le Vine, 2008), the Faraday rotation in the ionosphere (Yueh, 2000; Le Vine and Abraham, 2002; Vergely et al., 2014), the impact of the atmosphere (Liebe et al., 1992; Skou and Hoffman-Bang, 2005; Wentz and Meissner, 2016), and the effect of sea surface roughness on L-band emissivity (Meissner et al., 2014, 2018; Yin et al., 2016; Yueh et al., 2010, 2014). For all L-band radiometers, SSS retrievals algorithms are therefore based on:

- an empirical sea-water dielectric constant model at 1.4 GHz,
- a surface roughness correction model,
- a Radiative Transfer Model for Atmospheric corrections,
- a scattering model to correct for sea surface scattered Solar and celestial radiation, and,
- a model to correct for Faraday rotation and geometric rotation associated with the finite beam width of the antenna.

We review these models and corrections in the following subsections.

4.2. Models of the dielectric constant of seawater at 1.4 GHZ

The model function $\varepsilon_{sw}(f, S, T)$ is a key component of the radiative transfer forward model used for sea surface salinity retrieval from L-band radiometer data. The relative permittivity (also called dielectric constant) of the seawater, is a complex function dependent on temperature and salinity. The accuracy of SSS retrievals from L-band T_B strongly depends on how well the dielectric constant is known as a function of these two geophysical parameters (Lang et al., 2016). It can be estimated at any frequency within the microwave band from the Debye (1929) expression:

$$\varepsilon = \varepsilon_\infty + \frac{(\varepsilon_s - \varepsilon_\infty)}{1 - i\omega\tau} - i\frac{\sigma}{\omega\varepsilon_0} \quad (4)$$

in which i is the imaginary unit, ε_∞ is the electrical permittivity at very high frequencies, ε_s is the static dielectric constant, τ is the relaxation time, σ is the ionic conductivity, and ε_0 is the permittivity of free space, where ε_s, τ and σ are functions of T and S. At the time the first salinity mission was developed, these functions had been evaluated historically by Stogryn (1971), Stogryn et al. (1995), Klein and Swift (1977), and Ellison et al. (1998). Klein and Swift (denoted KS hereafter) modified the Stogryn (1971) model by using a different expression for the static dielectric constant ε_s(S,T), based on Ho and Hall (1973) and Ho et al. (1974) measurements at 2.6 and 1.4 GHz, respectively. The KS and Stogryn ε_{sw} models are valid for frequencies ranging from L- to X-bands (Meissner and Wentz, 2004, 2012; Meissner et al., 2014). Following pre-launch comparisons and analyses (Camps et al., 2004; Wilson et al., 2004; Blanch and Aguasca, 2004), the KS model was selected in the Level 2 Ocean Salinity (OS) processor (SMOS-Ocean Expert Support Laboratories, 2016).

An alternative model function developed by Meissner and Wentz (2004, MW hereafter) fits the dielectric constant data to a double Debye relaxation polynomial that performs best at higher frequencies. The seawater dielectric data were obtained by inverting T_B measurements from the Special Sensor Microwave Imager (SSM/I) at frequencies higher than 19 GHz; measurements from Ho et al. (1974) were used to derive the model at the lower frequencies. The MW model function was recently updated by providing small adjustments to the Debye parameters based on including results for the C-band and X-band channels of WindSat and AMSR (Meissner and Wentz, 2012, Meissner et al., 2014). The MW model is used in the Aquarius and SMAP SSS retrieval algorithms (Meissner et al., 2018).

Dinnat et al. (2014) analyzed the difference in SSS retrieved by SMOS and Aquarius radiometers and found that both instruments observe similar large scale patterns, but also reported significant regional discrepancies (mostly between ± 1 pss). SMOS SSS was found generally fresher than Aquarius SSS (within 0.2–0.5 pss depending on latitude and SST), except at the very high southern latitudes near the ice edge and in a few local (mostly coastal) areas. It was found that the differences exhibit large-scale patterns similar to SST variations. To investigate its source, Dinnat et al. (2014) reprocessed the Aquarius SSS, including the calibration, using the KS ε_{sw} model that is used in SMOS processing. This reprocessing decreases the difference between Aquarius and SMOS SSS by a few tenths of a pss for SST between 6 °C and 18 °C while warmer waters show little change in the difference. Water colder than 3 °C shows mixed results, probably due to a complex mix of error sources, such as the presence of sea ice and rough seas. The comparison of the reprocessed Aquarius SSS with in situ data from Argo shows an improvement of a few tenths of a pss for temperatures between 6 °C and 18 °C. In warmer waters, both the nominal and reprocessed Aquarius data, as well as SMOS data, have a fresh SSS bias. For very cold waters (< 3 °C), the reprocessed Aquarius data using the KS model show significant degradation of the SSS in comparison with the Argo, in turn suggesting that the KS model might be in error in the lowest sea surface temperature regime.

Direct laboratory measurements of the ε_{sw} at 1.413 GHz and SSS = 30, 33, 35, and 38 (Lang et al., 2016) were used to develop a new

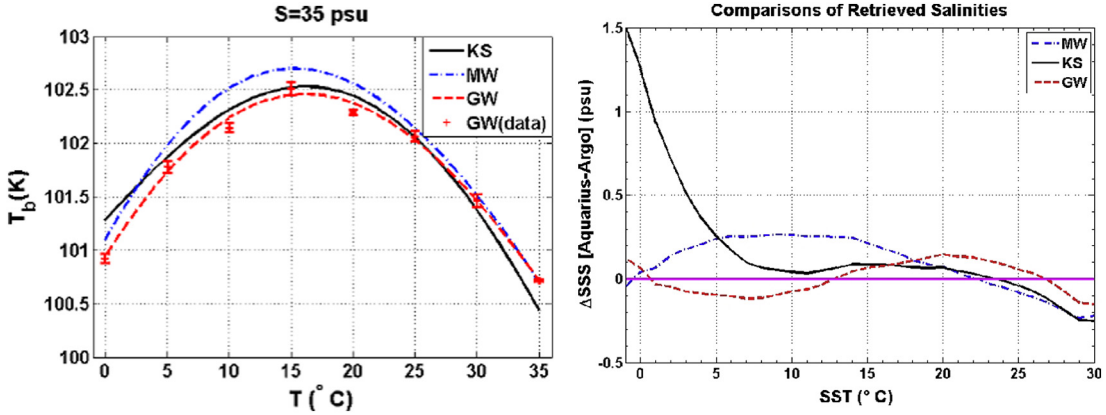

Fig. 9. (Left) Comparison of flat surface T_B at 1.4 GHz (V-pol, incidence angle =28.7°) as function of SST for SSS = 35 and different dielectric constant models (KS = Klein and Swift; MW = Meissner and Wentz; GW = George Washington (data & fit)); (Right): Difference between the salinity retrieved from Aquarius observation and in situ salinity (Argo data), using three model functions for the dielectric constant: KS, MW, and GW. Aquarius residuals have been recomputed using each model function (figures from Zhou et al., 2017).

model (Zhou et al., 2017) by fitting the measurements with a third-order polynomial. This new L-band ε_{sw} model has been compared with KS and MW. The authors claimed that this new model function (see Fig. 9) gives more accurate SSS at high (25 °C to 30 °C) and low (0.5 °C to 7 °C) SSTs than other existing model functions. Laboratory measurements at low SSS lead to a small increase in the accuracy of the model function. New measurements at 34 and 36 pss have been recently made and will be incorporated in the model function. This work is still in progress.

Despite its importance for SSS remote sensing, uncertainties remain in the 1.4 GHz seawater dielectric constant model. The new laboratory measurements combined with satellite data, will certainly help to minimize those remaining uncertainties.

4.3. L-band emissivity of a wind-roughened sea surface

Sea surface microwave emission for a given frequency and viewing geometry depends upon the sea water dielectric constant as well as sea surface roughness and sea foam. From detailed analyses presented in Johnson and Zhang (1999), the sea roughness contribution to the surface emissivity can be treated as the product of an electromagnetic weighting function and the sea surface roughness spectrum integrated over all surface wavelengths. The weighting function shows resonance peaks in the neighborhood of surface wavelengths with scales comparable to the electromagnetic wavelength (i.e., 21 cm for the L-band). The sea surface roughness spectrum around these small surface wave scales and associated wind-induced emissivity contributions generally correlate with the local surface winds. The sea surface roughness effect on microwave emissivity is therefore generally characterized as a function of the local surface wind speed and direction. These effects largely dominate the error budget of satellite SSS retrieval from L-band radiometers (Yueh et al., 2001). Hence, very accurate roughness correction models are needed. Furthermore, roughness measurements must be available in near real time for use in ground segment processors. In this respect, the spatial and temporal collocation of these auxiliary measurements with the satellite observations is also crucial. Various electromagnetic models have been developed to estimate the effects of wind-induced roughness on sea surface emission in the L-band. These include rigorous (Reul et al., 2005), asymptotic (Yueh, 1997; Johnson and Zhang, 1999; Dinnat et al., 2002, 2003; Vall-llossera et al., 2003) and empirical or semi-empirical model types (Camps et al., 2004, 2005; Boutin et al., 2004; Gabarró et al., 2004; Guimbard et al., 2012; Font et al., 2013; Yueh et al., 2013, 2014, 2015; Yin et al., 2012, 2016; Fore et al., 2016; Meissner and Wentz, 2012, Meissner et al., 2014, 2018).

In the latest algorithms implemented at ESA and NASA data centers, L-band Geophysical Model Functions (GMF) used for correction for the roughness-induced emissivity (Meissner et al., 2014, 2018; Yin et al., 2016; Fore et al., 2016) are all rather similar in shape and provide consistent results as a function of the 10 m height neutral wind speed, U_{10}, incidence angles and polarization (Fig. 10). They usually include an even 2nd order harmonic representation of relative wind azimuth dependence (Meissner et al., 2014), $\varphi_r = \varphi_w - \alpha$, where φ_w, is the wind direction and α the radiometer azimuthal look direction relative to North:

$$\Delta T_{rough,p}(U_{10},\theta) = \Delta T_{o,p}(U_{10},\theta) + \Delta T_{1,p}(U_{10},\theta)\bullet\cos(\varphi_r) + \Delta T_{2,p}(U_{10},\theta) \bullet\cos(2\varphi_r) \quad (5)$$

In Fig. 10, we reproduce the isotropic function term $\Delta T_{o,p}(U_{10})$ used for Aquarius v5.0, RSS SMAP v3, SMOS v662 and JPL SMAP v4 last release algorithms (Meissner et al., 2018; Yin et al., 2016; Yueh et al., 2014). The sensitivity of L-band T_B to surface roughness, expressed in terms of U_{10}: $\left(\frac{\partial T_B}{\partial U_{10}}\right)_L$, varies in the 0.1–0.5 K/(m/s) range. An uncertainty of 2 m/s on U_{10}, therefore, translates into a 0.2–1 K error in the correction of T_B for roughness or a 0.3–5 pss error on the retrieved

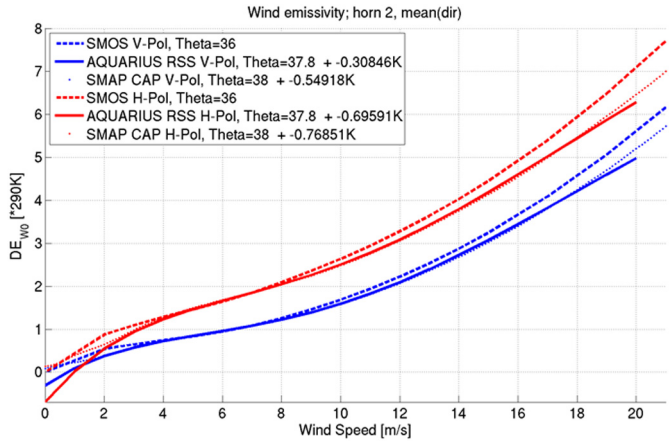

Fig. 10. Isotropic wind-induced emissivity contributions at L-band as modeled as function of surface wind speed for the last releases of the Aquarius v5.0 and SMAP v3 algorithms (solid curves, Meissner et al., 2018), for the SMOS v662 algorithm (dash curves, Yin et al., 2016), and dotted lines for the JPL Aquarius/SMAP CAP processing algorithm (Yueh et al., 2013, 2014). A sea surface temperature of 290 K has been used to compute the wind-induced brightness temperature.

salinity. To address this issue, a dedicated scatterometer was included onboard Aquarius to minimize such potentially significant correction errors.

Some remaining small differences in the roughness GMFs used in SMOS, SMAP, and Aquarius algorithms still exist and are subject of ongoing research. These differences are related to:

- The differences in auxiliary wind data used in the sea surface roughness correction algorithm. Depending on a particular mission, the winds are either the 10 m-height wind velocities from the European Center for Medium-range Weather Forecast (ECMWF) model forecast (SMOS), or the on-board scatterometer winds (Aquarius), or, the WindSat, F17/SSMIS satellite winds and the National Center for Environmental Prediction's model wind data (SMAP),
- Azimuth dependence of the roughness correction is a function of the relative wind direction φ_r (terms $\Delta T_{1,\,p}(U_{10})$ and $\Delta T_{2,\,p}(U_{10})$ in Eq. (5)). Its magnitude is significant for $U_{10} > 12$ m/s in the Aquarius and SMAP algorithms (with a peak-to-peak T_B change ~1.5 K at $U_{10} = 20$ m/s) but is much lower in the SMOS algorithm (Yin et al., 2016). The relative contribution of the first and second azimuth harmonics also varies among the algorithms, with Aquarius and SMAP CAP first harmonics $\Delta T_{1,\,p}$ (Yueh et al., 2014) being stronger than that for SMOS, especially at high wind speed. The second harmonics $\Delta T_{2,\,p}$ has a weak (< 0.1 K) impact for SMAP and Aquarius CAP algorithm up to 11 m/s. In contrast, the SMOS algorithm has significantly stronger second harmonics magnitude at $U_{10} > 12$ m/s.
- An option to account for some sea state dependencies in the GMFs (e.g., significant wave height (SWH) dependence of $\Delta T_{o,\,p}$) was introduced in Yueh et al. (2015) and Meissner et al. (2014). As discussed in Yueh et al. (2015), the empirical estimation of the second-order sea-state effects on L-band T_B (i.e., $\Delta T_{rough,\,p}(U_{10}, \theta, SWH)$) strongly depends on the choice of wind and wave products used to build up the GMF. As long as consistent wind and wave products are used, the SWH correction can reduce some regional SSS biases (Yueh et al., 2015). Local impacts of sea-state on L-band T_B can certainly be non-negligible (e.g. at wave fronts, within storm sectors, in wave-current interaction zones, in areas of calm seas …) as shown, for an example, by the swell-induced T_B modulations measured during a storm in the Mediterranean Sea (Camps et al., 2004). However, these effects are rather small in 'average' and difficult to correct. At this time, they are not accounted for by the last versions of either the SMOS, Aquarius, or SMAP GMFs.
- Sea surface temperature dependencies in the wind emissivity are also a source of algorithmic differences (Eq. (5) is thus multiplied by a correcting temperature dependent term ρ(SST) in the GMF of Meissner et al., 2018).

4.4. Atmospheric contributions

In the L-band, the effect of atmospheric scattering as well as clouds, and water vapor attenuation are all small thanks to relatively long electromagnetic wavelength (~21 cm) in comparison with typical atmospheric hydrometeor size (Yueh et al., 2001). However, the effect of atmospheric emission must be corrected to achieve accurate salinity retrievals. This contribution includes both upwelling and downwelling components of atmospheric radiation (the latter is reflected from the surface). The atmosphere emits and absorbs L-band radiation mostly due to molecular oxygen (O_2) with small contributions from water vapor, cloud liquid water, and rain (Blume et al., 1978; Ulaby et al., 1981; Blume and Kendall, 1982; Swift and McIntosh, 1983; Rosenkranz, 1998). The net atmospheric emission varies from about 2.4 to 2.8 K and is proportional to atmospheric pressure (Yueh et al., 2001). The approach adopted to correct SMOS, Aquarius, and SMAP, T_B for atmospheric impacts consists in using the conventional radiative transfer theory to model atmospheric attenuation and emission (e.g., Liebe et al., 1992). Atmospheric temperature and pressure profiles are needed in the transfer model and are usually obtained from meteorological models such as those provided by the ECMWF, or the NCEP. In general, the atmospheric impacts in the L-band can be corrected to within 0.3 K error (Meissner et al., 2018).

4.5. Sky and solar radiations

Downwelling L-band radiation from the sky (Le Vine and Abraham, 2004) can be scattered by the rough ocean surface towards the radiometer and contribute to the signal measured at the antenna level. The sources of celestial sky radiation comprise the constant Cosmic Microwave Background (CMB) radiation at 2.75 K, the contribution from galactic hydrogen (line emission) and the continuum radiation from extra-galactic sources. The distribution of these two last sources varies across the sky with local maxima found in the direction of the plane of the galaxy. This so-called "celestial" radiation reflects at the sea surface into the satellite radiometer aperture, but can be corrected using data obtained from all sky surveys using L-band radiometers (Le Vine and Abraham, 2004; Dinnat and Le Vine, 2008; Tenerelli et al., 2008; Reul et al., 2008a). If not well accounted for, this radiation can significantly affect the salinity measurement from Aquarius (Le Vine and Abraham, 2004), SMOS (Tenerelli et al., 2008) or SMAP (Meissner et al., 2018). The approach used to model the sky brightness scattered by the sea surface and reflected towards the radiometer involves integration of the sea surface bi-static scattering coefficients at the radiometer frequency weighted by the incident sky brightness temperatures at 1.4 GHz. Then the estimate- of the signal scattered towards the radiometer is weighted by and summed over the antenna gain pattern to produce a correction for the measured antenna temperature, T_A. Bi-static sea surface scattering coefficients at L-band are generally modeled using physical optics (Reul et al., 2007), or geometric optics (Meissner et al., 2014, 2018) with an effective mean square slope about half of that of Cox and Munk (1954). Meissner et al. (2018) have shown that this approach matches well with the observed sky and sun radiation scattering in the L-band, and is consistent with GNSS-Reflectometry studies (e.g., Garrison et al., 2002). Independently, the JPL PALS (Wilson et al., 2003, 2004) and the ESA/COSMOS (Reul et al., 2008b) aircraft data verified that this approach is accurate to within a few tens of a Kelvin. Nevertheless, satellite salinity fields still exhibit remaining ascending – descending biases with spatio-temporal patterns that can correlate with the reflection of galactic radiation from the ocean surface, indicating potential residual errors in this correction. Attempts to use sky maps derived from SMOS data itself obtained when the instrument performs cold sky calibration manoeuvers (Martin-Neira et al., 2008) instead of L-band sky survey maps are currently on-going. The fore – aft look capability of SMAP makes it possible to observe the Earth with the reflected galaxy only present in either the fore or the aft look. This has helped to fine-tune and improve the galactic reflection model for both Aquarius and SMAP (Meissner et al., 2018).

At L-band, the sun is also a very hot thermal source with effective temperatures on the order of 10^6 during active periods of the solar cycle (Le Vine et al., 2005; Reul et al., 2007) with even higher amplitude emission is reached during solar flares. Even though the sun is relatively small in angular extent, it is such a strong source of radiation at L-band that solar effects remain one of the most important potential sources of uncertainty on salinity retrieval (Le Vine et al., 2005; Reul et al., 2007), particularly for SMOS and SMAP missions. In the case of Aquarius/SAC-D mission, the antenna boresights were directed across track towards the night-time side of the ground track (i.e. away from the sun) to minimize the impact of reflected solar radiation.

For a real-aperture radiometer such as the Aquarius and SMAP radiometers, sun glint (i.e. reflection at the sea surface) impacts the measurements through its contribution to the antenna temperature. Dinnat and Le Vine (2008) estimated that this contribution does not

exceed about 0.14 K for Aquarius mission in quiet sun conditions (i.e., the sun brightness temperature equal about 500,000 K). Because the antenna boresight of the rotating real-aperture radiometer of SMAP enters the day side of the Earth's terminator (i.e., the moving curve that divides the daylight side and the dark night side on Earth), the solar effects on the antenna brightness can be of much higher amplitude for this mission, potentially exceeding 15 K. Observations with large sun glint are flagged in both the Aquarius and SMAP salinity retrievals.

Two main mechanisms are responsible for the contamination of the reconstructed T_B images by sunglint in the case of an interferometric radiometer like SMOS. The specular point on Earth from the sun towards the radiometer antenna never enters the spatial domain within which the salinity is retrieved (the so-called Extended Alias Free-Field Of View or EAF-FOV) during the year (Reul et al., 2008a, 2008b). However, the closer the ground target at which SSS is retrieved is to the sun specular point, the higher the sunglint signal obtained by the radiometer. For the SMOS, this occurs on the western edges of the swath on descending passes. Sunglint contamination reaches maximum amplitude during winter solstices in the southern hemisphere with interannual variability related to the sun spot solar cycle. Owing to the relatively very high T_B of the sun at L-band, the solar radiation scattered by the rough sea surface towards the radiometer can be critical for salinity remote sensing even at angles far away from the specular point.

Second, because the spacing between elementary receivers on the 3 arms of MIRAS does not satisfy the Nyquist-Shannon sampling criterion, there is spatial aliasing in the reconstructed T_B image. Aliases of the bright zone surrounding the sun specular point may thus contribute to an interferometric SMOS reconstruction bias far away from the actual location of the sun specular point (Anterrieu, 2007; Khazaal et al., 2009). Combined, these two mechanisms may contribute in excess of 10 K to the reconstructed brightness image used for salinity retrieval (Reul et al., 2007). While observations with large sun glint are also flagged in the SMOS salinity retrievals, the impact has a strong seasonal cycle and a strong dependence upon both latitude and across-swath position. The Kirchhoff scattering forward model developed prior to launch (Reul et al., 2007) to predict sunglint contamination in SMOS data has been recently compared to observation (Khazaal et al., 2016). It was found, that the application of the correction efficiently reduces the average and Root Mean Square (RMS) differences between the data and the full ocean-scene forward model.

A key variable of all sun glint corrections for SSS remote sensing is the solar flux at L-band. It can be derived (Guidice et al., 1981) from the data of the United States Air Force Radio Solar Telescope Network (RSTN) observatories around the globe. As discussed in Khazaal et al. (2016), there are remaining uncertainties of about ~10% in the one-second or daily noon solar flux data among the available radio-telescopes of the RSTN network. To minimize such uncertainties, alternative methods to directly estimate the solar flux from the sun images in the satellite antenna brightness T_A data itself are currently being developed (Crapolicchio et al., 2018).

The Moon has much lower L-band T_B than the Sun. At ~280 K, it does not contribute any significant signal when it reaches the antenna directly through low gain side- or back-lobes during nominal Earth pointing operations. It can potentially contaminate ocean observations when entering the main beam after reflection at the sea surface. Dinnat et al. (2009) estimated contributions of ~1 K, ~0.1 K and 0.03 K for a smooth surface and rough surfaces at 3 m/s and 8 m/s wind speed, respectively. In the case of Aquarius, there is only a short time each month when the spacecraft position allows for such contaminations and the potential contaminations are flagged and discarded.

4.6. Faraday rotation

For satellite sensors, the propagation path from the sea surface to the satellite radiometer also includes the ionosphere. Attenuation and emission in the ionosphere are not important in the L-band (Le Vine and Abraham, 2002) but the polarized fields rotate across the ionosphere (Faraday rotation) with an angle that depends on the Earth's magnetic field and on the electron density of the ionosphere (Total Electron Content, TEC). This is an issue because the surface emissivity also depends on polarization. The orbits of SMOS, Aquarius, and SMAP (sun-synchronous with equatorial crossings at 6 AM/6 PM) avoid the mid-day maximum TEC, but the potential remains for enough rotation of the polarization vector to warrant correction (Le Vine and Abraham, 2002), especially at 6 PM local time. All salinity missions operated during solar cycle #24 which had a sunspot number peak and increased ionization in April 2014. Models of the ionosphere, especially over the ocean where data are limited, are improving but still not sufficiently accurate. For SMOS, SMAP, and Aquarius data processing, the Faraday rotation angle is derived from the third Stokes parameter (correlation between vertical and horizontal polarization) plus a measurement of radiation at vertical and horizontal polarization. In particular, the ratio of the third Stokes parameter to the difference between vertical and horizontal polarization can be used to retrieve the rotation angle (Yueh, 2000; Waldteufel et al., 2004). For SMOS, the main issue comes from the absolute calibration of the third Stokes parameter using a so-called Ocean Target Transformation (OTT, see Vergely et al., 2014). The corrections also rely on external information providing an a-priori guess of the ionospheric and geomagnetic fields (such as the 13th Generation International Geomagnetic Reference Field available at https://www.ngdc.noaa.gov/IAGA/vmod/igrf.html, see Thébault et al., 2015). The Vertical ionospheric Total Electron Content (VTEC) gives the TEC of the ionosphere over the Earth at 2 h intervals. Both the geomagnetic field and TEC maps are interpolated at the line of sight coordinates for 400 km spacecraft altitude. A correction to account for the actual satellite altitude and interpolation using 2-hour TEC maps is also applied.

4.7. Land and ice contamination

Remote sensing of salinity from space is complicated by the presence of land or sea ice in the antenna 3 dB field of view or through side-lobe contamination. In the L-band, land and sea ice are radiometrically much warmer than the ocean. The characteristics T_B of land, ice, and open ocean varies within ~250–300 K (Amazon rainforest and Sahara desert), ~180–220 K (Dome-C in Antarctica) and ~70–130 K (open ocean), respectively. Hence, the salinity retrieval quality degrades quickly as the footprint approaches land when its signal starts entering the antenna side lobes. As soon as the fraction of land or sea ice within the footprint exceeds 1%, the T_B can be significantly affected and bias the retrieval of salinity. As a result, the required accuracy can be achieved only over open ocean several beam footprints away from the land (or sea ice), or after thorough corrections.

To provide a correction for the spurious effects from land in the SMOS Level 2 salinity algorithm (Spurgeon et al., 2017), radiative transfer simulations of the antenna radiometer T_B (using climatologies for land and ocean characteristics derived over the SMOS operation period 2010–2019) were compared with time-mean satellite observation of the ocean-land contrasts. The systematic biases observed over the mission lifetime between radiative transfer model predictions and observations are used to build the correction. These corrections depend on the radiometer look angle, pass direction (ascending/descending), polarization, position in the field of view, pixel center latitudes/longitudes, and the fraction of land in the pixels. They provide means (i) to estimate the ocean pixels that are affected by the land signal entering the antenna side lobes and/or (ii) to correct for the land contamination effects. In addition to the side-lobe effects, SMAP data are also affected by grating lobes associated with the inevitable faceting incorporated into SMAP large deployable mesh reflector (Rosenkranz de Lasson et al., 2017) These are also included in the corrections (SMOS-Ocean Expert Support Laboratories, 2016).

While similar types of empirical approaches are used to correct for the land-sea contamination at the brightness temperature level in the

official SMOS, SMAP and Aquarius in-swath salinity retrieval algorithms (Fore et al., 2016; Spurgeon et al., 2017; Meissner et al., 2018), the sources for land-contamination of SMOS interferometric data are more complex than for real aperture radiometers. In addition to the side-lobe effects, the land-sea contamination observed in SMOS T_B is found to have two main other contributions (Corbella et al., 2015): a floor error inherent in image reconstruction and a multiplicative error either in the antenna temperature or in the visibility samples[2] measured by the correlator. Methods to mitigate these land-sea contamination effects during image reconstruction processing are the focus of on-going research (e.g., Gonrález-Gambau et al., 2018).

Alternative methods were recently developed for SMOS (Kolodziejczyk et al., 2016; Alvera-Azcárate et al., 2016; Olmedo et al., 2017, 2018a; Boutin et al., 2018) in which empirical land sea contamination correction and/or filtering methods to mitigate the coastal biases are applied after the salinity is retrieved from the measured swath T_B. This new mitigation produces SMOS SSS estimates which are closer to SMAP SSS in coastal areas. Because SMAP is a real aperture radiometer, SSS in coastal areas from that sensor are less affected by land masses than SMOS SSS data which are also affected by image reconstruction artefacts, in addition to the land-sea transition effects. This improvement was confirmed by a better matching between river plume signatures observed in SMOS SSS with those reported from SMAP data in the Bay of Bengal and the Gulf of Mexico (Boutin et al., 2018). The new correction/filtering methods also provide useful SSS retrievals from SMOS in semi-enclosed basins such as the western Mediterranean Sea (Alvera-Azcárate et al., 2016; Olmedo et al., 2018a).

In general, satellite SSS can be estimated close to the coast but with reduced accuracy in comparison with open ocean waters. The SSS variability in the coastal domain is, however, much higher than in the open ocean which allows for a useful signal to noise ratio in most coastal cases. The distance from coastlines at which land effects start affecting the T_B varies from ~400 km (Aquarius) to ~1000 km (SMOS, SMAP).

The corrections to minimize Gibbs oscillations near sea ice/open ocean transitions in SMOS data are still under development (Khazaal et al., 2018). Statistical and empirical bias corrections are indeed much more complex in case of seasonally moving ocean/sea ice interface. There is a correction for the ocean-sea ice transition in Aquarius and SMAP algorithms (Fore et al., 2016), but it remains unsatisfactory mainly because L-band sea ice T_B is variable and poorly modeled. Hence, observations with even small amounts of suspected ice contamination are flagged and discarded in the higher level SSS products. Even with this stringent treatment, SSS retrievals in the high latitudes can suffer from sea ice contamination due to the uncertainty in ice fraction from ancillary products, especially for low ice concentrations.

5. Satellite SSS products quality assessment

Since the early 2000s, the global density of near-surface salinity measurements from in situ platforms has increased notably with the advent of the global Argo array of profiling floats (Riser et al., 2016, Figure 1), a period that includes the first decade of operation of the L-band salinity radiometer missions. Satellite SSS can now be systematically validated against co-localized measurements from an ensemble of in situ sensors. These include near-surface salinity taken by Argo profiling floats (usually at ~5 m), Thermo-SalinoGraph (TSG) sensors installed onboard ships of opportunity (Alory et al., 2015), research vessels (Gaillard et al., 2015), or sailing ships (Reynaud et al., 2015), upper level data from salinity equipped moorings (McPhaden et al., 2010), surface drifters measuring SSS in the upper 50 cm (Morisset et al., 2012), and marine mammals (Treasure et al., 2017) equipped with Conductivity-Temperature-Depth (CTD) sensors. The respective density of each of these in situ data since 2010 is illustrated in Fig. 11.

5.1. General consideration for the validation of satellite SSS

As discussed in Boutin et al., 2016, there are three important issues to be considered in assessing the accuracy of satellite SSS using in situ data.

First, adequate sampling of the ground truth salinity field remains a challenge as the density of measurement is not always sufficient to capture some of the important time and space (horizontal and vertical) scales of salinity variability (Lindstrom et al., 2015, 2019).

Secondly, sampling differences between satellite and in-situ measurements need to be properly accounted for (Vinogradova and Ponte, 2012, 2013a; Vinogradova and co-authors, 2019). Quasi-instantaneous swath measurements of satellite SSS correspond to spatial averages over radiometer footprints (with typical scales varying from 40 to 150 km) while most of in situ measurements are generally pointwise samples (e.g., from Argo or moorings). In addition, in situ salinity data acquired at a high spatial resolution within the radiometer footprint (e.g., TSG, surface drifters) need to be spatially averaged at the radiometer resolution before being compared to satellite SSS data. Moreover, the space-time composite of swath satellite SSS (i.e., the so-called level 3 SSS data) can be week- to –month-long averages while most of in situ salinity data are 'quasi-instantaneous' (a few seconds to few minute averages). Significant differences between the two types of measurements can, therefore, occur in regions of strong spatio-temporal variability (e.g., rain bands, river plumes, strong eddy currents, as discussed in Lindstrom et al., 2015, 2019). These representation errors (in both spatial and temporal domains) need to be properly taken into account when assessing satellite SSS accuracy.

Third, satellite radiometers provide SSS estimates averaged over the upper first centimeter while most in situ measurements are performed at a depth of about 5 m (e.g., Argo, TSG) or ~1 m (e.g., moorings). In calm wind conditions but high rain rates, within river plumes, or, for example, in the vicinity of shallow (5–10 m) Equatorial Undercurrents, the near surface salinity can be significantly fresher than at depth (Boutin et al., 2016 and references therein). Using auxiliary data (e.g. satellite precipitation and winds), it is, therefore, important to systematically characterize the conditions in which salinity vertical stratification in the upper meter might be a source of differences and systematic bias between the very near-surface satellite SSS and the deeper in situ salinity data.

Keeping in mind these important considerations, we review the respective quality status of the latest SMOS, Aquarius, and SMAP SSS products in the sections below.

5.2. SMOS SSS product quality assessment

In the following, we distinguish the quality assessment of the swath SSS data retrieved from SMOS (so-called level 2) and of the space-time composite (so-called level 3) of the swath products.

5.2.1. SMOS Level 2 swath SSS data quality

A new Version (662) of the SMOS Level 2 in-swath SSS was released by ESA in May 2017 including reprocessing of the full SMOS mission lifetime (Spurgeon et al., 2017). Compared to the previous version (v622), the Level 2 SSS evolved from three very similar retrieved SSS values (which corresponded to three separate roughness correction models, see Font et al., 2010) to one SSS value using the roughness correction model of Yin et al. (2016).

In addition, a new salinity product empirically corrected for land-sea contamination (LSC) is now included. The correction is applied to the SMOS measured brightness temperatures before SSS retrieval. Other

[2] The cross correlation of the analytic signals collected by each pair of receivers "k,j" forming a baseline gives a sample of the visibility function, V_{kj}, that develops into a brightness temperature map by means of a Fourier synthesis technique.

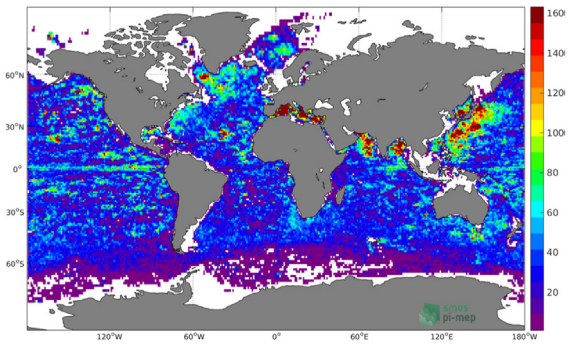

(a) ARGO floats

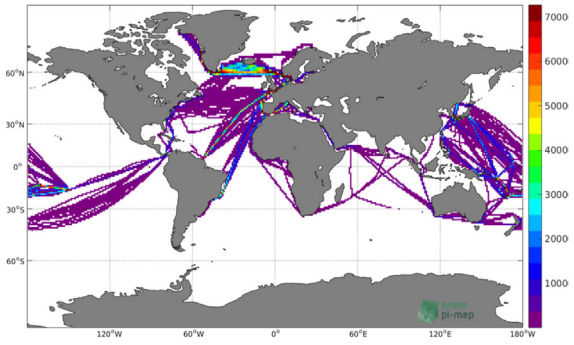

(b) TSG-LEGOS

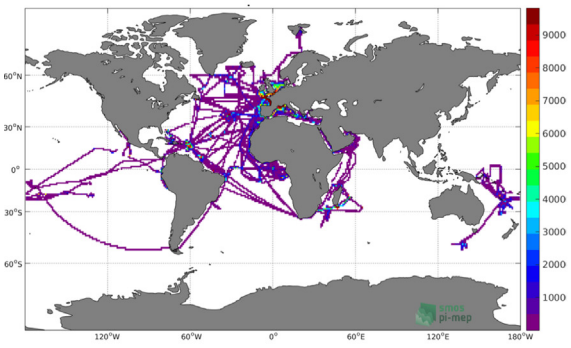

(c) TSG GOSUD research vessels

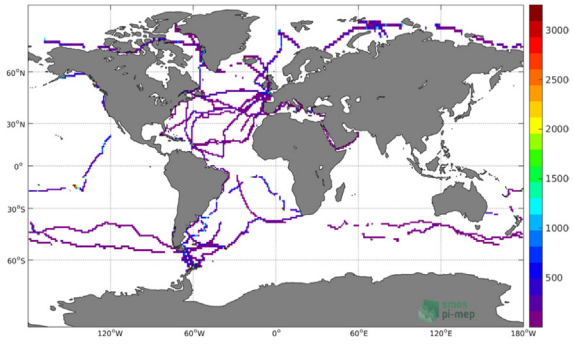

(d) TSG-GOSUD sailing ships

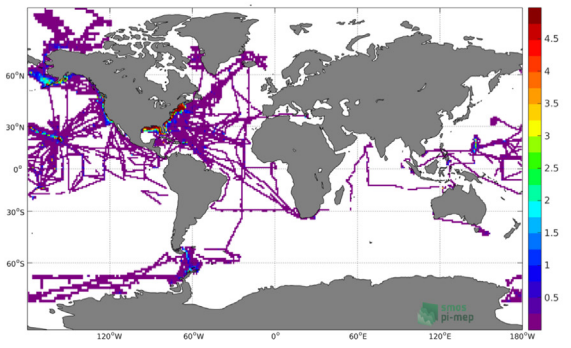

(e) TSG SAMOS

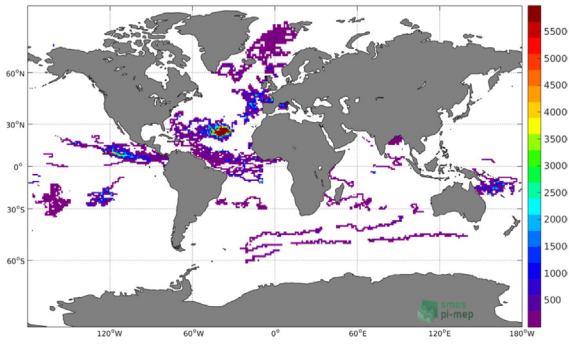

(f) Surface Drifters

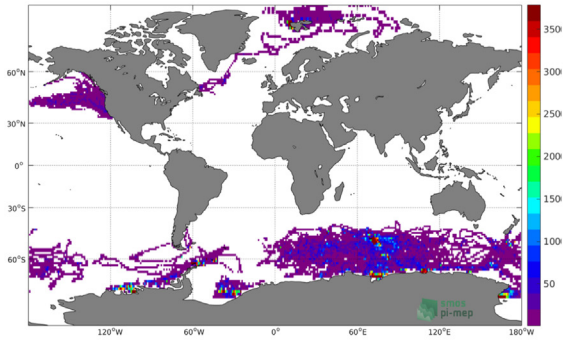

(g) Marine Mammals

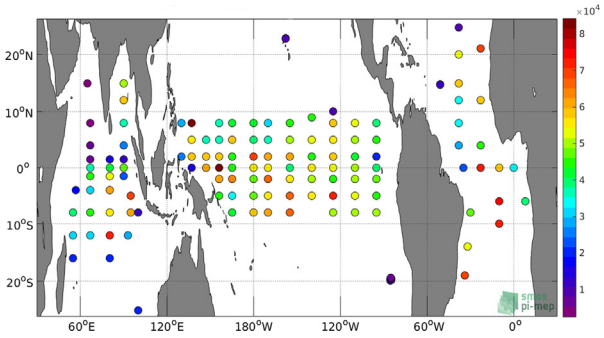

(h) Global Tropical Moored Buoy Array

Fig. 11. Density of *in situ* SSS observations per 1°x1° square, per type of *in situ* sensor, as collected during 2010–2019.

algorithm improvements include filtering to mitigate contamination from RFI, new sun glint and roughness correction models at high winds, and retrieval of the Total Electronic Content from SMOS 3-rd Stokes parameter.

Systematic comparisons between SMOS L2 SSS data and available co-located in situ salinity were performed for 2010–2018 data by LOCEAN and more recently using the ESA SMOS Pilot Mission Exploitation Platform (PI-MEP, see also Section 5.5). Concerning the latter, the complete in situ salinity database is first filtered based on quality flags provided by in situ data centers (e.g., Coriolis Data Assembly Centre) so that only valid ground truth data remain. High-spatial resolution in situ measurements, such as those from TSG or surface drifters, are also spatially filtered (using a running median window) to match with the ~43 km SMOS ground footprint. For each in situ data sample collected in the Pi-MEP database, the platform searches for all SMOS L2 satellite SSS data at grid nodes located within 22 km of the in situ data location and acquired with a time-lag ≤6 h. If several satellite SSS samples are found to meet these criteria, the final satellite/in situ SSS match-up point is selected to be the closest in time from the in situ data measurement date. An ensemble of geophysical and observation parameters (SST, wind, rain, distance to coasts, etc.) are also collected to characterize the conditions of each in situ/satellite co-located pair. As revealed by Fig. 12, the Root Mean Square Differences (RMSD) $\Delta SSS = SSS_{SMOSL2}\text{-}SSS_{ARGO}$ between SMOS L2 swath and collocated Argo salinity is 1.1 pss for data within 80°S-80°N. It decreases to 0.6 pss for the open ocean tropical band, which partly reflects the higher radiometric measurement sensitivity in warm waters.

The monthly-average SMOS level 2 SSS data which are non-corrected for land-sea contamination exhibit an almost systematic 1–2 pss fresh bias with respect to in situ data within a band of about 800 km from coastlines (e.g. see Fig. 12 for descending passes. Very similar results were found for ascending passes). Note that because of the interferometric principle of SMOS, the land-contamination effects and needed correction extend far from the coast (see details in Section 4.7). After applying the correction developed at T_B level, the mean bias of retrieved SSS is almost cancelled over coastal regions (> 40 km and < 800 km) and the standard deviation error estimated at global scale is reduced by ~0.1 pss. However, in regions with high probability of RFI events (e.g. China Sea, Sea of Japan, North Indian Ocean, …), or high natural horizontal SSS variability (e.g., large tropical river plumes, inter-tropical convergence zone, major current areas), the empirical land-sea contamination correction is either unavailable (due to insufficient data to statistically compute a robust empirical land-sea correction) or unreliable (due to a mismatch between the reference SSS

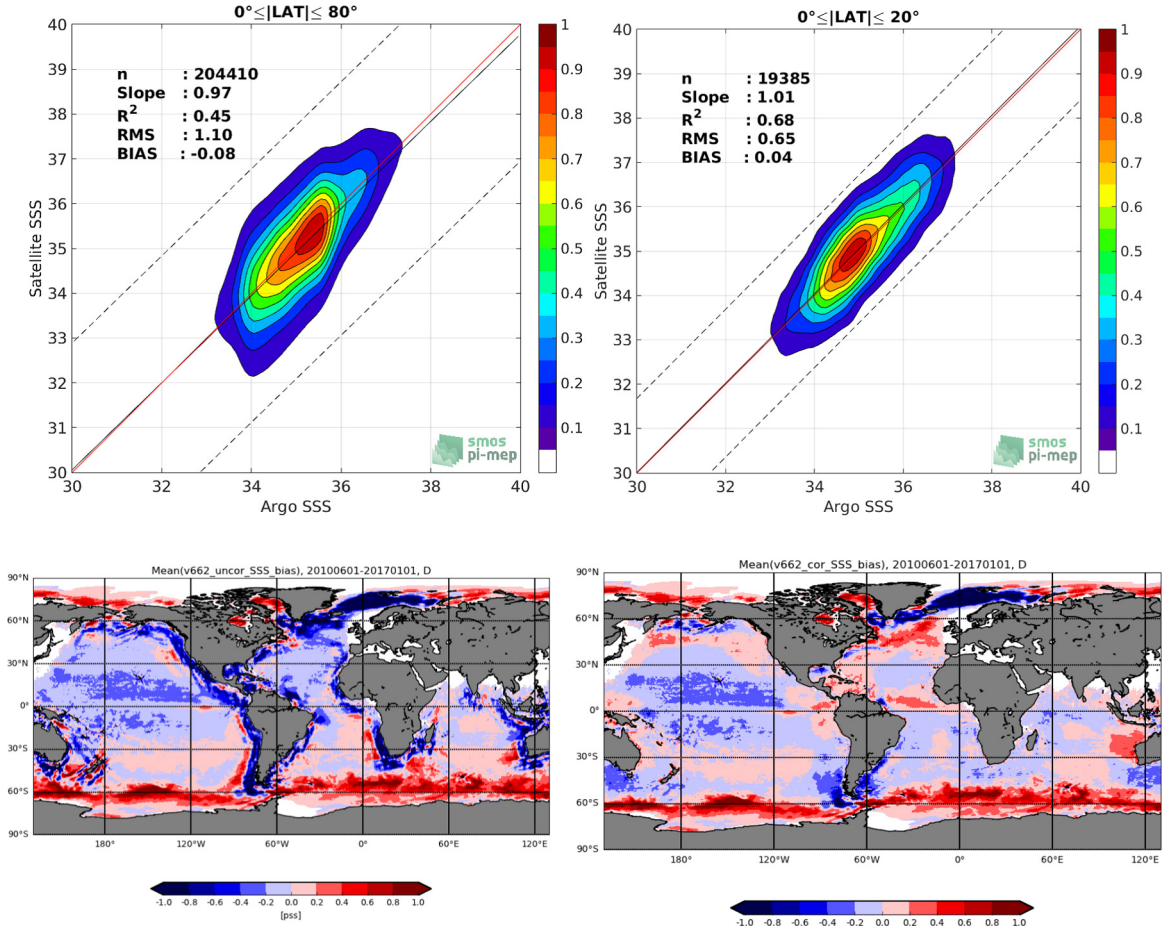

Fig. 12. (Top) Contour maps of the concentration of the co-localized SMOS Level 2 SSS v662 data (y-axis) versus Argo SSS (x-axis) at match-up pairs for latitude bands within ± 80° (left) and ± 20° (right) apart of the equator. For each plot, the red line shows x = y. The black thin and dashed lines indicate a linear fit through the data cloud and the ± 95% confidence levels, respectively. The number of match-up pairs n, the slope and R^2 coefficient of the linear fit, the root mean square (RMS) and the mean bias between satellite and in situ data are indicated for each latitude band in each plots. (Bottom) Mean differences between the temporally averaged SMOS Level 2 v662 SSS descending pass data over the month of June 2010 and the optimally interpolated in situ ISAS field for the same month. The differences were aggregated into spatial domains of size ¼°x ¼° and are shown for SMOS data without land sea contamination correction (left) and with land sea contamination correction (right). (For interpretation of the references to color in this figure legend, the reader is referred to the web version of this article.)

field climatology and the actual average SSS). In these regions, the corrected SSS is prone to inaccuracies. Note that the SMOS L2 satellite SSS is significantly saltier than in situ observations even after LSC correction in the vicinity of sea ice in the Southern Ocean, a likely effect of the KS dielectric constant model that seems to underperform below 4 °C.

Thanks to the new scene-based RFI filtering (described in Section 3) and empirical correction for the land-sea contamination applied at the brightness temperature level, the number and quality of SSS retrievals significantly increased in the global region located < 1000 km from coasts. The implementation of the sunglint correction model resulted in increased number and improved quality of SSS retrievals at swath edges during periods of high sun glint (e.g., the winter solstice of 2014 during which the maximum in solar cycle #24 was reached). Despite these improvements, across- track biases and systematic differences between SSS from ascending and descending passes are still present in the SMOS level 2 SSS data. Retrievals near swath edges (cross-track distance ≥350 km) have higher uncertainties due to the smaller number of T_B measurements and contamination from various sources, especially sun aliases and associated ripples (tails). Stronger biases are observed for SSS retrieved from descending passes than from ascending in January–March and October–December. These differences are potentially related to remaining errors in the short-term seasonal stability calibration of the instrument or in the sea surface scattered solar and sky radiation corrections.

5.2.2. SMOS Level 3 composite SSS data quality

Kolodziejczyk et al. (2016) developed an approach to reduce SMOS systematic errors near continents and a Bayesian approach for mapping SMOS SSS L2 data on L3 Equal-Area Scalable Earth Grid (EASE-Grid), which greatly enhanced the quality of SMOS SSS. Boutin et al. (2018) revised this methodology with: a) less strict data filtration in areas of high natural variability (inferred from SMOS data) and b) a correction for seasonally and meridionally varying systematic errors. With this new approach, SMOS coastal SSS data became more consistent with the SMAP retrieved SSS, with both capturing concordant spatial and temporal variations of low salinity plumes in the Bay of Bengal and Gulf of Mexico. A systematic comparison between this 18-day CATDS SMOS Level 3 SSS (v3) product at 0.25° resolution and collocated Argo salinity is available in a dedicated Pi-MEP report (Pi-MEP, 2019).

As illustrated in Fig. 13, the RMS difference $\Delta SSS = SSS_{SMOSL3} - SSS_{ARGO}$ between composite SMOS L3 and collocated Argo salinity is 0.33 pss within 80°S-80°N belt and decreases to 0.28 pss in the tropics. The RMSD (see Table 2 in Pi-MEP, 2019) drops to 0.22 pss when the distance to the coast > 800 km. It increases to 0.33 pss within 150–800 km of the coast and rises to 0.5 pss closer to coasts (< 150 km). Although the RMS difference increases approaching land, the larger magnitude of natural SSS variability in the coastal ocean results in a favorable signal-to-noise ratio. As illustrated in Fig. 13, the STandard Deviation of the difference (STD) increases in highly dynamical regions where pointwise Argo measurements may misrepresent the ~25 km gridded Level 3 SSS. Increased STD is also observed along coasts of Asia where RFI events are numerous. Note also a remaining SSS bias in the SMOS Level 3 products over the Southern Ocean and north of 40°N where SSS is 0.2–0.4 pss saltier than Argo salinity. This issue is likely related to errors in the KS dielectric constant model at cold SST (as discussed in Section 4.2) and/or badly corrected storm-induced signals.

Other Level 3 SMOS products, including Olmedo et al. (2017), show RMSD patterns versus Argo similar to Boutin et al. (2018) RMSD. It is interesting to note that L3 SSS maps from different SMOS products show consistent SSS variations in many regions where no or little valid SSS retrievals are available, including semi-enclosed seas and high RFI areas (like the Mediterranean Sea, Arctic, and Antarctic Oceans).

Although in semi-enclosed seas and high RFI areas, the uncertainty of derived SSS is larger than in other ocean areas, the signal-to-noise ratio may be of sufficient quality for a wide range of applications (Isern-Fontanet et al., 2016; Olmedo et al., 2018a, 2018b). In particular, these areas show spatially coherent SSS structures, as evidenced by the singularity analysis of Olmedo et al. (2016), which reflects the overall consistency among the products.

5.3. Aquarius SSS product quality assessment

Aquarius project released its final version (Version-5) in December 2017 (see Meissner et al., 2018). Over most of the ocean, the RMSD between weekly SSS maps and collocated in situ data do not exceed 0.2 pss (Fig. 14). The monthly, global average RMSD between gridded Aquarius and Argo data is smaller than 0.2 pss (Fig. 15).

The RMS error of Aquarius Level-2 and Level-3 SSS data was estimated from a triple collocation analysis (Stoffelen, 1998) to be 0.17 pss and 0.13 pss, respectively (Kao et al., 2018). The JPL Aquarius CAP products have similar errors (Tang et al., 2014a, 2014b, Tang et al., 2015) in rain free conditions and slightly higher error 0.2–0.3 pss under heavy rain.

5.4. SMAP SSS product quality status

RSS (Remote Sensing Systems, Inc.) adapted the Aquarius Version 5 salinity retrieval algorithm to SMAP to produce the Version 3 salinity release (Meissner et al., 2018). The algorithm changes include taking into account the orbit and pointing, a correction for the emissive SMAP antenna and a change in the wind induced emissivity correction. The geographical distribution of the mean spatial bias between the 70 km SMAP V3 monthly SSS in rain-free conditions and the shallowest salinity from Argo profile analysis (Roemmich and Gilson, 2009) produced by the Scripps Institution of Oceanography (SIO) is shown in Fig. 16. As illustrated, the bias is, in general, < 0.2 pss, with larger positive values in the sub-polar North Pacific and Atlantic and in the Southern Ocean poleward of about 50°S, and rather stable in time (Fig. 16). From the triple point analysis (SMAP, in situ, and HYCOM SSS), the standard deviation error of SMAP V3.0 rain-filtered monthly composite at 1° x 1° spatial resolution is about 0.15 pss, slightly more than that for the Aquarius V5.0 (Fig. 16).

The JPL SMAP SSS algorithm (Fore et al., 2016, 2018) includes an improved land/ice correction and is able to retrieve SSS in ice-free regions within 35 km of the coast. Comparison with in situ Argo data, ARGO monthly gridded products, and tropical moorings has been made to assess its quality (Fore et al., 2018). The accuracy is about 0.2 pss between 40°N and 40°S. The correlation of JPL SMAP SSS with the salinity from tropical moorings (about 0.77) is better than that for the HYCOM assimilation model (about 0.67).

Over cold water, the accuracy is degraded to about 1 pss but remains sufficient for detection of freshwater plumes from larger rivers flowing into the Arctic Ocean (Tang et al., 2018).

5.5. The SMOS Pilot Mission Exploitation Platform

The SMOS Pilot Mission Exploitation Platform (Pi-MEP) for Salinity (see the dedicated web platform) is an ESA initiative with twofold motivation:

i) To serve as a generic satellite salinity validation and algorithm evolution platform,
ii) To offer a testbed to enable oceanographic process studies using SMOS SSS in synergy with other satellite data (e.g., SST, winds, SSH, precipitation).

The Pi-MEP Platform is fully operational as of the middle of 2019 and transitioning into a reference hub for satellite SSS missions by providing access to all satellite (SMOS, Aquarius, SMAP) SSS product validation and additional thematic datasets, including precipitation,

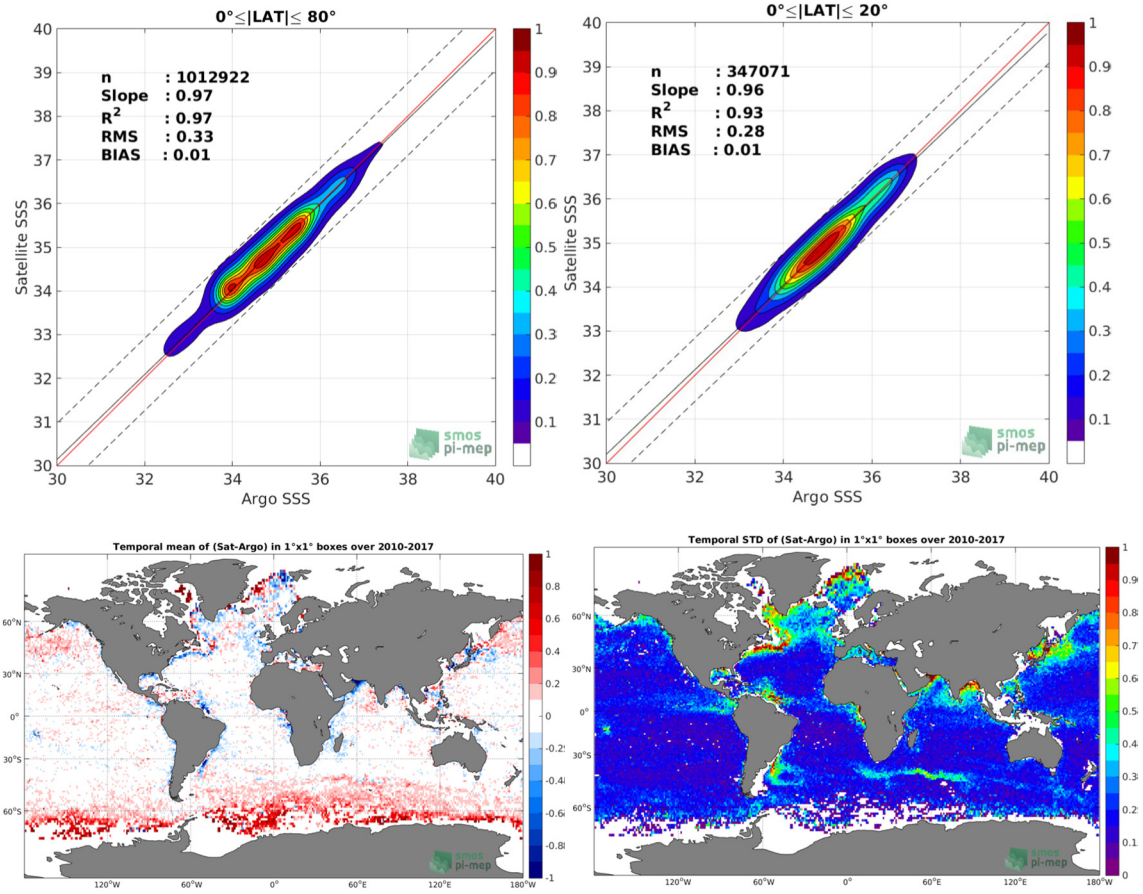

Fig. 13. (Top) Contour maps of the concentration of the co-localized SMOS Level 3 SSS data at 0.25°x 0.25° resolution and composite of the swath data over 18 day periods (Boutin et al., 2018) (y-axis) versus Argo SSS (x-axis) at match-up pairs for latitude bands within ± 80° (left) and ± 20° (right) of the equator. Same legend than in Fig. 12 top panels. Bottom: Temporal mean (left) and standard deviation (right) of the co-localized SSS differences between the SMOS Level 3 data and upper-level Argo float data given within 1°x1° square and over the 2010–2017 period.

evaporation, currents, sea level anomalies, winds, and SST. Collocated databases of SMOS, Aquarius, and SMAP products with in situ SSS from Argo, TSG, moorings, and drifters, and inter-comparison reports including quality assessments at different spatio-temporal scales are systematically generated by the platform. A list of the major satellite SSS products used by the platform together with some detailed information (product's name, level, spatial and temporal resolution, temporal coverage, update frequency, latest version, provider and a web access link towards each product) as available in January 2020 is available in Appendix A. Dedicated tools allow data visualization, metrics computation, and user-requested feature extractions. The Platform also allows monitoring SSS for selected oceanographic "case studies", ranging from tropical river plumes to high latitudes and semi-enclosed basins.

To maximize the effectiveness of the Pi-MEP platform to support the international ocean salinity science community, ESA and NASA have established a collaboration to further enhance the functionality of the platform that can better meet satellite SSS data user needs. This platform can also serve as an example for other potential joint efforts between ESA and NASA in terms of satellite data validation and exploitation.

5.6. Satellite SSS quality summary

The 3 satellite sensors exhibit RMSD from in situ data (SSS_{SAT}-SSS_{insitu}) ranging between 0.15 and 0.25 pss for ~2 week or monthly time scales and within 0.25°x0.25° to 1°x1° boxes in the mid and tropical latitudes and sufficiently far away from coasts, where they fulfill the objectives of the GODAE requirements. Thanks to its scatterometer data and better radiometric sensitivity and stability, the Aquarius SSS is the most accurate swath product among the 3 missions. The data from this satellite, however, suffer from relatively poor spatial and temporal resolution.

All 3 sensors show degraded SSS quality in cold waters of high latitudes. This reduced accuracy in cold water conditions is related to the decreased sensitivity, uncertainties of the dielectric constant model and the roughness correction in stormy high latitude conditions, as well as the vicinity to land (Arctic) and sea-ice. Nevertheless, recent studies (Matsuoka et al., 2016; Tang et al., 2018; Olmedo et al., 2018b) show that satellite SSS has a great capability in monitoring fresh water plumes in the Arctic region (Lee et al., 2016), as well as changes in fresh water content associated with seasonal changes in sea ice extent (Garcia-Eidell et al., 2017), providing an unprecedented look into regions poorly covered by in situ measurements.

T_B from all three sensors is affected by land-sea transitions, resulting in degraded SSS quality along the coasts (up to 1000 km from the coast). All three sensors also show residual seasonal and latitudinal large-scale biases, due to instrument thermal drifts and solar effects. These biases are corrected empirically using reference fields (e.g. HYCOM, Argo Optimal Interpolation).

Finally, SMOS and Aquarius data are in general more affected by RFI than SMAP data in several key oceanic regions (e.g., Asian coastlines, Bay of Bengal, Arabian Sea, Mediterranean Sea). Because the SMAP sensor is equipped with a dedicated onboard RFI filtering device, the SSS from this instrument provide better viewing of main river plumes in highly RFI contaminated areas such as the northern Bay of Bengal (e.g. Fournier et al., 2016b, 2017a). On the other hand, SMAP T_B

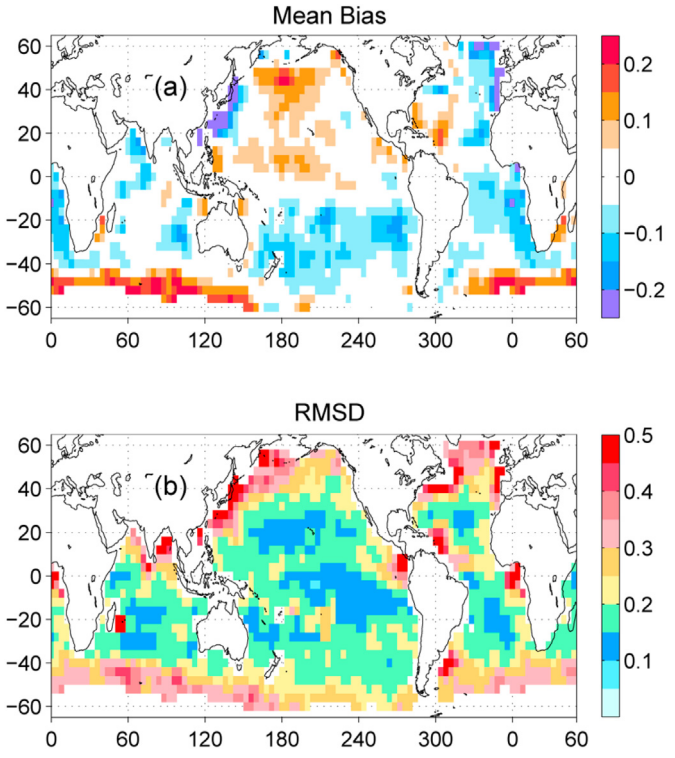

Fig. 14. Geographical distribution of (a) mean spatial bias (pss), and (b) root-mean-square deviation (RMSD) (pss) between the Aquarius weekly Level-3 SSS product and Argo float observations. The error statistics were computed by comparing Argo float measurements for a given week with SSS values at the same locations obtained by interpolation of the corresponding Level-3 SSS maps. The geographical distributions are computed in 8°-longitude by 8°-latitude bins. This is a reproduction of Fig. 3 from Kao et al., 2018.

calibration is more challenging than Aquarius (Fore et al., 2016; Meissner et al., 2018) and the SMAP salinity retrieval algorithms require empirical adjustments. The absolute value of SMAP SSS may include biases up to 0.2 pss in low- to middle-latitude open ocean (Fore et al., 2018).

Nevertheless, regardless of the challenges of satellite SSS validation (e.g. related, in part, to the representativeness of in situ measurements on temporal, horizontal and vertical scales), satellite SSS data provide extremely useful measurements that have hitherto eluded broad oceanographer attention.

6. An overview of the major scientific achievements from satellite SSS

Thanks to their global coverage and frequent revisit time, the unique data from satellite salinity missions definitively improve our knowledge of the global SSS field and provide new information on its variability on spatial and temporal scales that were not globally accessible before. In particular, satellites allow the frequent panoramic observations of SSS imprints of large-scale anomalies, such as El Niño Southern Oscillations (ENSO), Indian Ocean Dipole, and Madden Julian Oscillation among many others. In addition, L-band radiometers sample the very near surface and therefore provide for the first time a view of the upper ocean response to atmospheric freshwater forcing. But it should be mentioned that it is challenging to interpret the wealth of complexity of rapid geophysical processes that define instantaneous SSS of individual imagery (e.g., Wurl et al., 2019). Systematic monitoring reveals the persistence of features with both smaller spatial scales (< 100 km) and shorter periods (less than a month) important for understanding ocean-land-atmosphere interactions (fronts, large-scale eddies, meanders, fresh river plume dispersal, planetary and tropical instability waves, etc.). The SMAP and SMOS satellite salinity products have also reached a relatively high skill level with temporal consistency that allows the identification of anomalous mooring data and inadequate temporal sampling in the Argo-monthly-gridded and HYCOM products (Fore et al., 2018). Compared to in situ sensor networks, satellite SSS gives more uniform spatio-temporal sampling, improves the ability to estimate horizontal gradients, which is important for frontal genesis, eddy-mean flow interaction, and biogeochemistry. We highlight these major achievements in the sections below.

6.1. Large scale SSS anomaly monitoring and relationships with climate variability

ENSO is the leading interannual mode of the Earth climate system with global atmospheric, oceanic, ecosystem, and human impacts. It has been found that upper ocean salinity plays an active role in ENSO behavior (Zhu et al., 2014). SSS variability associated with both El Niño (Hasson et al., 2018) and La Niña events (Hasson et al., 2014) has been demonstrated by analyses of SMOS data in the tropical Pacific. Besides a strong eastern equatorial Pacific fresh anomaly, mainly produced by local rainfall during the mature phase of 2014–2016 El-Nino (Fig. 17, see also Guimbard et al., 2017), negative SSS anomalies were also detected between 0° and 15°N around 170°W, from mid-2014 to mid-2015 (Boutin et al., 2016). Significant freshening was also observed around 20°N close to Hawaii during the last 2014–2016 El Niño (Hasson et al., 2018).

Eastward excursions of the eastern edge of the Eastern-Pacific Fresh Pool (EPFP) observed by Guimbard et al. (2017) in SMOS data reveal apparent ENSO-related extremes (in particular, during 2012 and 2015). These zonal shifts are not only associated with anomalies of precipitation but also in surface currents (Grodsky and Carton, 2001; Liu et al., 2009), and trade winds in the central Pacific.

Analysis of Aquarius SSS further confirmed the presence of a sharp SSS front (coinciding with the 34.8-pss isohaline) in the Pacific warm pool region (Qu et al., 2014). Zonal shifts of the eastern edge of the tropical Pacific warm pool (29 °C isotherm) and the SSS front (34.8 pss isohaline) correspond well to ENSO phases (Fig. 17) and correlate well (> 0.8) with the Southern Oscillation Index (SOI),which record the occurrence of El Niño (SOI $<$ 0) and La Niña (SOI $>$ 0) events. Negative interannual anomalies in the SSS averaged over 150°E-170°W and 2°S-2°N are found (Singh et al., 2011) during El Niño events, mostly reflecting the eastward displacements of the low-salinity western Pacific warm pool, and vice versa during La Niña events. Salinity variability in the southeastern Pacific characterized by a new Southeastern Pacific SSS Index (SEPSI) derived from satellite SSS data, is found to be highly correlated with the central Pacific El Niño and Trans-Niño indices (Qu and Yu, 2014). It has large positive anomalies during central Pacific El Niño, (Modoki) due to stronger zonal SST gradient between the central and eastern tropical Pacific, and thus is indicative of the type of El Niño.

The assimilation of satellite SSS in ocean circulation models is challenging because of various and complex biases present in these data. Nevertheless, it has been demonstrated that satellite SSS assimilation can significantly improve simulations of sea surface/subsurface properties (e.g., Köhl et al., 2014; Vernieres et al., 2014; Hackert et al., 2014; Toyoda et al., 2015; Vinogradova et al., 2014, Vinogradova, 2018; Martin, 2016; Lu et al., 2016; Martin et al., 2018; Tranchant et al., 2019). In particular, Hackert et al. (2014) explored satellite and in situ salinity assimilation in a coupled ocean-atmosphere model to demonstrate that using satellite SSS data in the Pacific region improves short-term ENSO prediction. Namely, the assimilation of Aquarius SSS improves the Niño3.4 SST index hindcast skill in terms of correlation and root-mean squared difference from observations (Fig. 18). The improved hindcast skill was attributed to better spatio-temporal sampling of SSS from Aquarius than from in-situ measurements, which provides a better constraint on interannual mixed-layer density

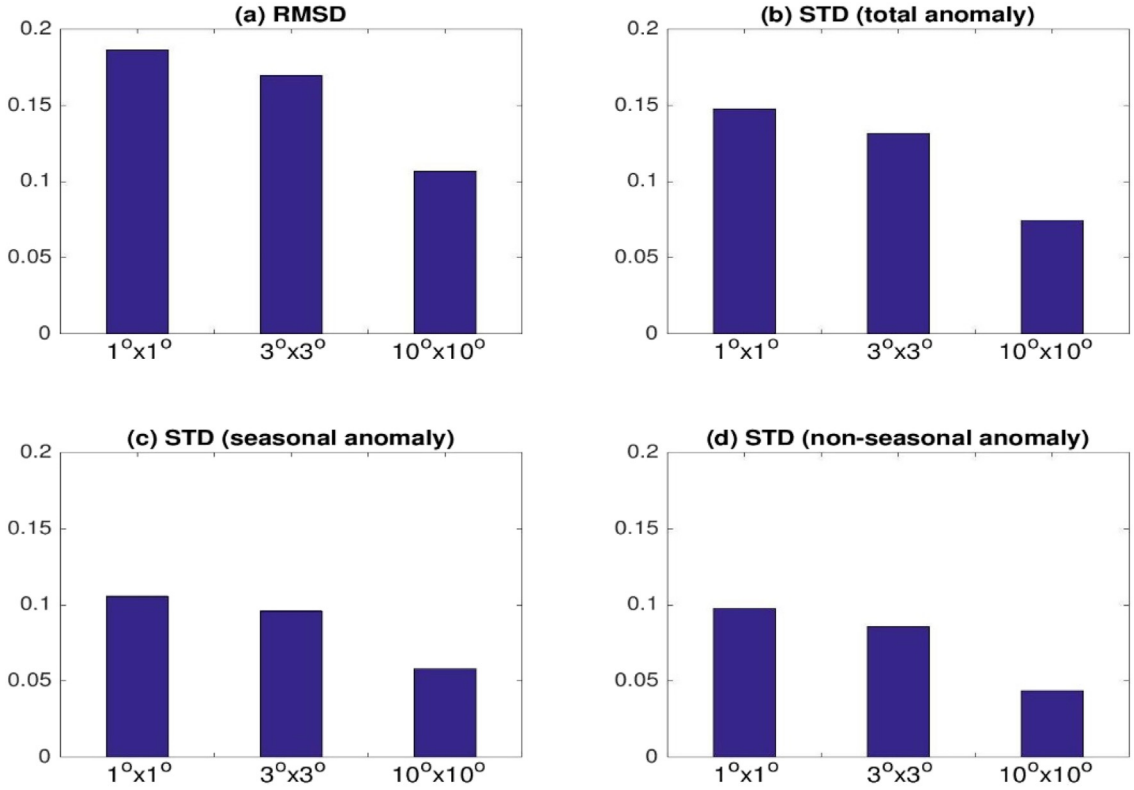

Fig. 15. Globally-averaged values [unit of pss] of the root-mean square (a) and standard deviation (b) of the temporal differences between Aquarius and Argo objectively-analyzed SSS fields estimated within boxes of varying sizes (x-axis). The std. is provided in (b) for total anomalies; (c) for composite seasonal anomalies; and (d) for non-seasonal anomalies. After Kao et al., 2018.

variations. Although longer records (covering multiple ENSO events) are still needed to establish the robustness of satellite SSS impact on model predictions, the first results based on the existing satellite SSS records are encouraging. Chakraborty et al. (2014) have shown that zonal migration of the eastern edge of the western Pacific warm pool and entire tropical Pacific currents are simulated more realistically if assimilating Aquarius SSS together with satellite SST. Surface data assimilation projects in the vertical and improves the subsurface salinity structure (Lu et al., 2016). Köhl et al. (2014) used SMOS SSS to inversely constrain the estimate of the net freshwater forcing (E-P) and found positive impacts of SMOS SSS assimilation on E-P estimates, particularly in the rainy tropical belt.

Recent coordinated simulations conducted by the UK Met Office and Mercator Ocean to investigate the impacts of assimilation of satellite SSS on simulations of the 2015/16 El Niño are described in Tranchant et al. (2019) and Martin et al. (2018). Globally, it is found that satellite SSS assimilation has a positive impact on the modeled salinity in the upper 30 m. The model amplitude of TIW during the El-Niño 2015/2016 event is also modified by the assimilation of satellite salinity, impacting the forecast sea surface height (SSH).

ENSO-related SSS response is not limited to the Pacific and extends into the Atlantic and the neighboring Indian Ocean. Despite similar magnitudes of rainfall response, Indian Ocean salinity response is generally stronger than Atlantic response, which is explained by the impacts of currents. Tropical Indian Ocean surface salinity responses to ENSO and Indian Ocean Dipole (IOD) are related to changes in both currents and rainfall. The important role of Indian Ocean zonal currents acting on the strong eastward zonal salinity gradient was suggested by Grodsky et al. (2001) who revealed a strong wind-induced impact of Pacific ENSO on the Wirtki jet, including its complete reversal during the 1997 El Nino. Further research has confirmed that ENSO and IOD salinity signatures are strongly related to impacts of these climate variability modes on zonal currents in the tropical Indian Ocean, with modifications of rainfall also contributing (Grunseich et al., 2011; Subrahmanyam et al., 2011; Zhang et al., 2013; Durand et al., 2013; Nyadjro and Subrahmanyam, 2014, 2016; Du and Zhang, 2015; Pant et al., 2015; Akhil et al., 2016; Fournier et al., 2017a; Yuan et al., 2018). Salinity variations associated with the IOD mode have been observed by the SMOS and Aquarius, with both instruments capturing well all stages of IOD evolution, to which salty upwelling along Java–Sumatra coasts is an important contributor (Du and Zhang, 2015). Satellite SSS (Akhil et al., 2016; Fournier et al., 2017a) also reveal that remote IOD forcing results in anomalous circulation in the Bay of Bengal that drives interannual SSS along the east coast of India and in the Southern Andaman Sea, areas that are not sampled well by in situ data (e.g., see Fig. 22). While interannual discharge fluctuations dominate salinity variations near the Ganga-Brahmaputra mouth, wind-driven interannual currents contribute significantly to interannual SSS in most of the river plumes (Akhil et al., 2016).

The seasonal variability of anomalous SSS in the Indian Ocean was also explored for its role as a precursor for the South Asian Summer Monsoon. Using both Aquarius SSS and Argo salinity, Yuan et al. (2018) revealed an elongated area of anomalously salty water in the southwestern Indian Ocean prior to the onset of the South Asian Summer Monsoon.

The Madden-Julian Oscillation (MJO) is the prevailing mode of tropical variability at intraseasonal time scales. The relative contribution of SSS and SST to the MJO-related changes in ocean surface density remains, however, poorly known. Shinoda et al. (2013) demonstrated that large-scale intraseasonal SSS patterns associated with the MJO are detectable in the Indian Ocean by satellite measurements (Aquarius) based on the comparison with in situ observations and with satellite-derived near surface velocity fields. Combining Aquarius SSS together with satellite SST over the equatorial Indian and Pacific Oceans, Guan et al. (2014) have shown that the SSS has a similar or even larger contribution to MJO-related surface density variations in comparison

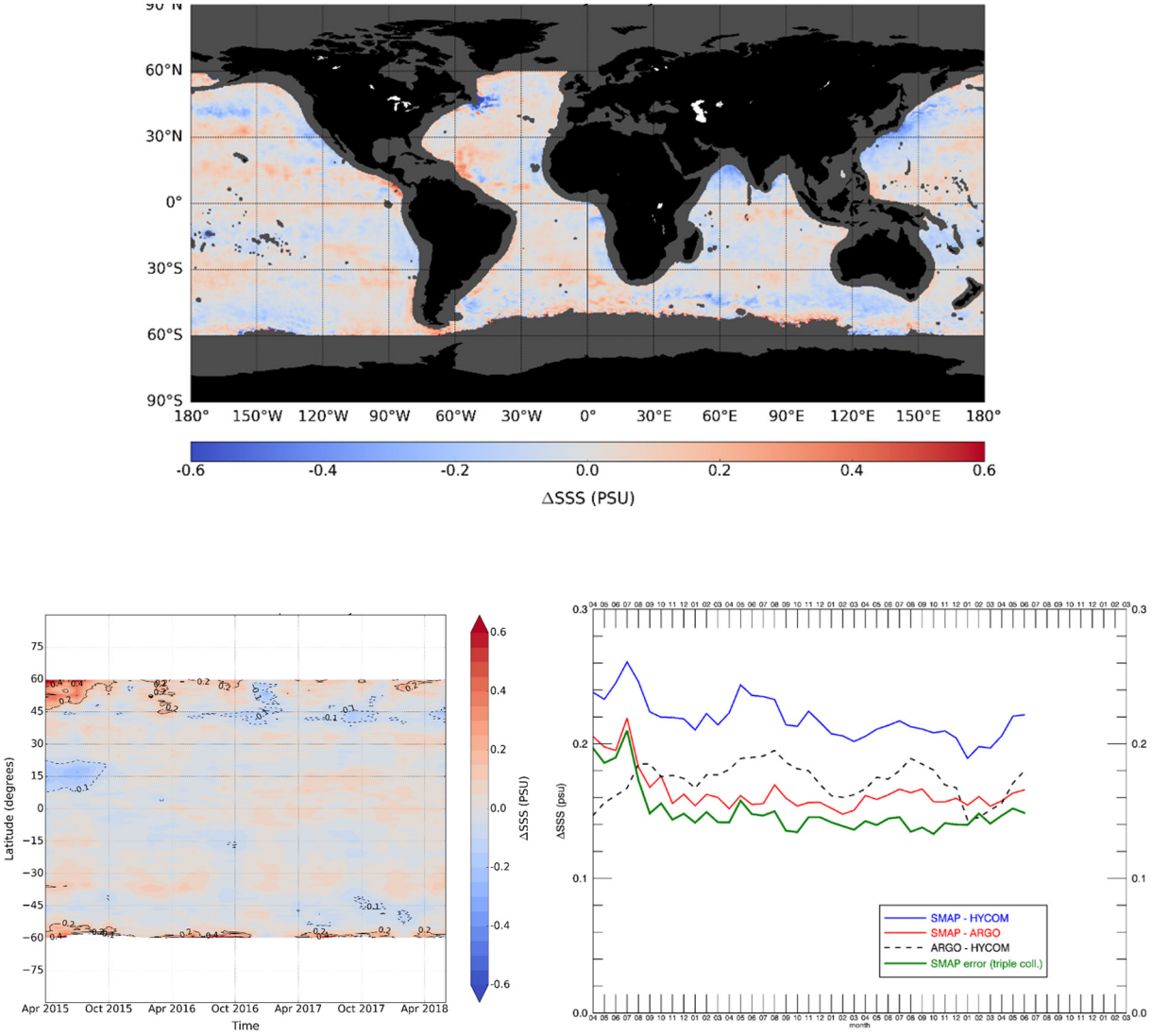

Fig. 16. Top: Map showing the time-averaged (April 2015–March 2018) differences between SMAP v3 and Argo SSS in 1˚X1˚ boxes. Bottom left: Hövmueller diagram showing the differences between SMAP v3 and Argo SSS as function of latitude and time. Right: monthly-averaged standard deviation of the differences between SMAP v3 and Argo SSS as function of time. The monthly time steps (x-axis) are provided from April 2015 to March 2018.

with the SST. Hence, air-sea coupled models need a proper account of SSS variations in order to simulate the variability associated with the MJO and the related ocean-atmosphere coupling.

Regardless of the complexity of coastal SSS retrieval, satellite salinity missions open new opportunities in shelf research. Despite still low spatial resolution (in comparison with other satellite products, like SST) and land contamination effects, both of which limit the usefulness of satellite SSS close to the land, Guerrero et al. (2014) have suggested that satellite SSS captures the detrainment of shelf waters and, for the first time, allows testing the hypothesis about their fate in the open southwestern Atlantic and to validate numerical simulations. In particular, the seaward transport of shelf waters from the Rio de la Plata region produces one of the strongest salinity signals of the South Atlantic, excluding the tropical belt.

Another hot spot of Atlantic salinity variability is located on the northwest shelf south of Nova Scotia where the SSS experiences a wide spectrum of oscillations. Focusing on this region, a consistent variability was found by Grodsky et al. (2017) in Aquarius and SMOS data, both showing a steady shelf SSS increase of ~1 pss south of Nova Scotia during 2011–2015. The primary cause of the transition to saltier conditions on the shelf was attributed to decreased upstream advection by the anomalously weak Scotian Shelf Current that conveys fresh and cold water from high latitudes into this region. At shorter, intra-annual time scales, the advection of salinity anomaly by mean currents also becomes important. This was illustrated by Grodsky et al. (2018b) who used the SMAP data to observe a few months long evolution of salty anomaly that propagated down northwestern Atlantic shelf along Nova Scotia and finally impinged into the Gulf of Maine.

Such high latitude satellite salinity observations are greatly complicated by the proximity of land and the cold background SST. While absolute values of satellite SSS are often biased in coastal regions, the satellite SSS anomaly has better fidelity and suitability to extend closer to the coasts. SMAP and SMOS data were recently used (Grodsky et al., 2018a, 2018b) to explore water inflow into the Gulf of Maine, which showed significant water intrusions in between Georges Banks and Nova Scotia in the winters of 2016/17 and 2017/18. Strong salinity patterns ($\geq$0.5–1 pss) associated with Gulf of Maine water intrusions are generally consistent between SMAP and independent SMOS observations. In the winter of 2016/2017, they revealed fresh SSS anomaly in the northeastern Gulf of Maine produced by a change in the wind-driven circulation and associated transport from the Scotian Shelf into the Gulf of Maine (Grodsky et al., 2018a).

Here we illustrate saltier than usual Gulf of Maine SSS in the winter of 2017/18 (Fig. 19). Its origin was linked with a salty outer shelf

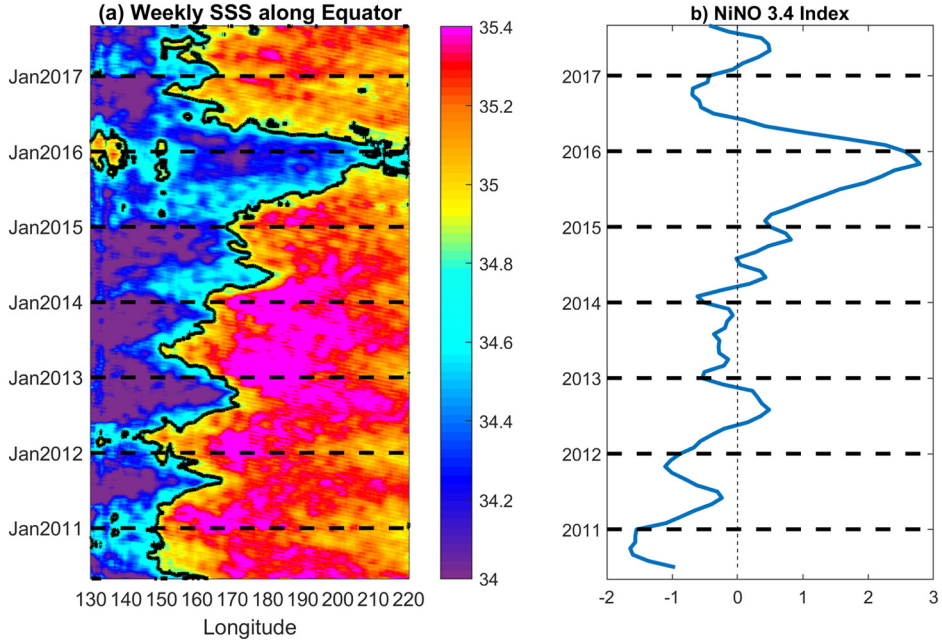

Fig. 17. a) SSS (pss) along the equator (3°S-3°N) in the Pacific on a monthly time scales from SMOS, compared with b) the Niño 3.4 index based on NOAA ERSSTv5 (in situ only) during the period May 2010–August 2017. The black contours in (a) indicate the 34.8-pss isohaline.

feature that penetrated into the Gulf due to a number of complex interactions with neighboring Gulf Stream warm core meanders/rings. Satellite altimetry, SSS, and SST analysis of Grodsky et al. (2018b) suggest that, before entering the Gulf, the salty surface water connected with Gulf Stream features several times, and was likely advected onto the shelf and then into the Gulf of Maine due to these interactions. According to satellite SSS data, this episode led to significant salinification (about 1pss) in the northeastern Gulf of Maine.

Salinity records from the Jordan Basin buoy in the interior of the Gulf of Maine agree with satellite SSS and confirm the salty feature intrusion in showing four months of the increased salinity of the upper 50 m starting in Nov. 2017 (Salisbury and Jönsson, 2018). Temperature-Salinity analyses of mooring data describe this satellite observed surface inflow as modified warm Atlantic slope water, normally present only below 100 m and previously not detected at the surface in the 15-year mooring record. The surface appearance of this salty feature was made possible by compensating effects of temperature and salinity on the density that allowed this salty shelf-sea water mass to be advected into the fresh and cold Gulf of Maine surface waters as surface trapped feature (Fig. 19). Although it was previously assumed that such salty features enter the Gulf in deeper layers and thus are not detectable by remote sensing techniques, these recent satellite salinity observations show that spatial SSS information from satellite sensors is able to provide a new tool for Gulf of Maine water mass exchange study that augments the existing observing system.

6.2. SSS signatures of oceanic features and processes at mesoscales

Thanks to their increased spatial and temporal resolution in comparison with the global in situ observing systems, satellites provide new information on the SSS field variability not only at large scale but also at meso-scale within the range 50–150 km, 10–30 days (Kolodziejczyk et al., 2016). This unprecedented capability allowed observing some key dynamic ocean features such as the surface signature of oceanic planetary waves, eddies, and fronts in a new and unique manner.

Observations of SSS by Aquarius provided the first space-borne observations of the salinity structure associated with TIWs in the tropical Pacific (Lee et al., 2012). The salinity patterns observed in regions

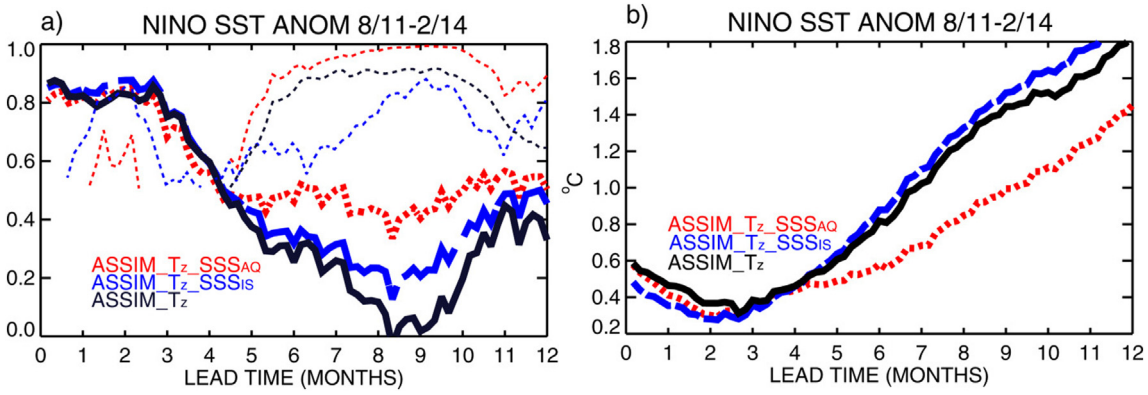

Fig. 18. (a) Correlation coefficient and (b) RMS difference of the model SST forecasts with the observed NINO3 SST anomaly. The period considered is August 2011 to February 2014. The solid black curve is initialized using assimilation of subsurface temperature (ASSIM_Tz), the thick dotted red curve from subsurface temperature and Aquarius SSS (ASSIM_Tz_SSSAQ) and the dash blue curve from subsurface temperature and weekly OI of all available near-surface salinity (ASSIM_Tz_SSSIS). The thin dotted curves indicate the corresponding significance of the differences from a Fisher Z test. After Hackert et al. (2014). (For interpretation of the references to color in this figure legend, the reader is referred to the web version of this article.)

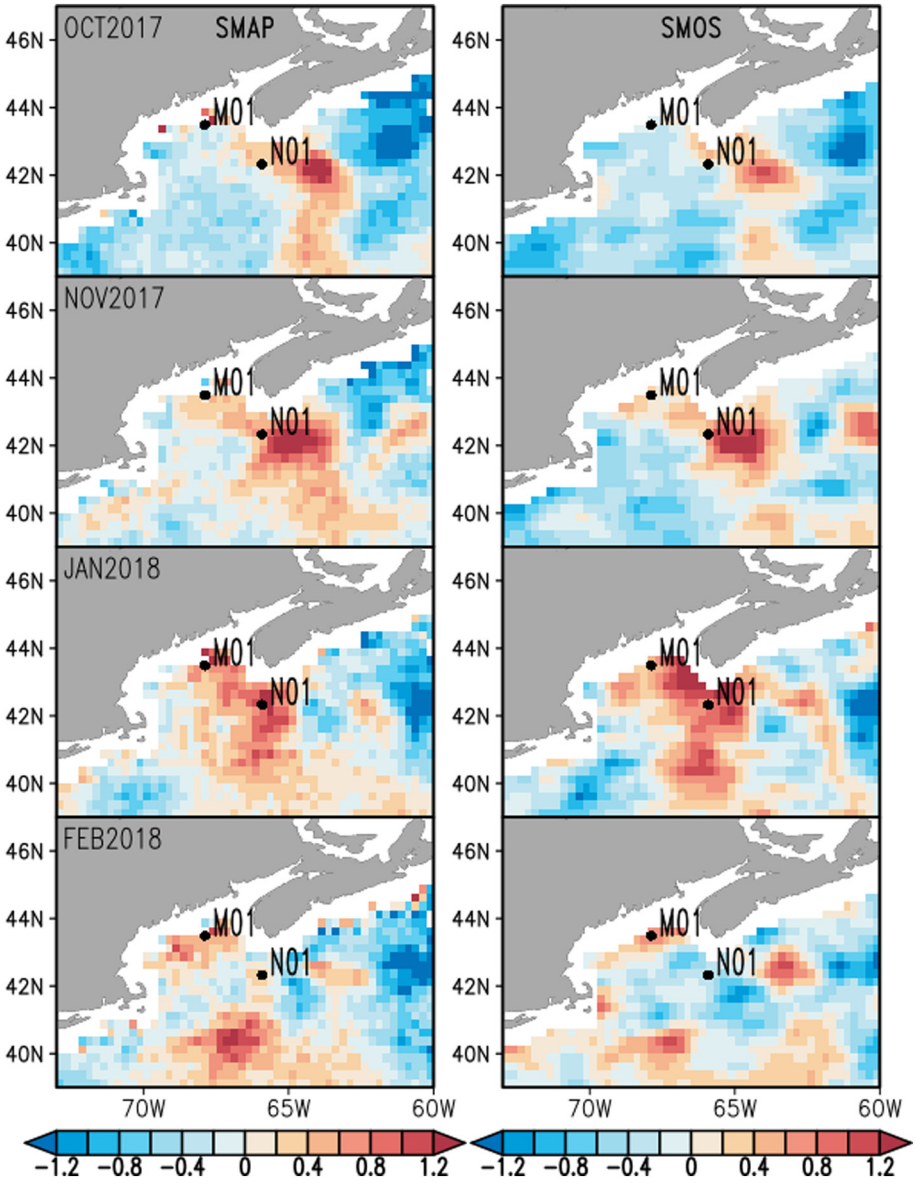

Fig. 19. SMAP (version 3) and SMOS (CATDS/LOCEAN version 2) anomalous SSS (pss) during salty anomaly intrusion into the Gulf of Maine. Gulf of Maine observing system buoys M01 and N01 are also shown.

of TIWs (Fig. 20) complement the suite of ocean satellite observations of these processes including SST, SSHA, surface current, ocean surface wind, and chlorophyll-a. The strongest TIW signatures in SST and SSHA are usually detected few degrees north of the equator. In contrast, the SSS signature is the strongest near the equator in the eastern equatorial Pacific where the meridional salinity gradient between saltier subtropical South Pacific water and fresher Inter-tropical Convergence Zone (ITCZ) water is located. The dominant speed of westward propagation of TIW SSS signatures is found to be about two times faster than TIW phase speed derived from SST and SSHA observations away from the equator. This difference is attributed to the prevalence of 17-day TIWs near the equator as revealed by Aquarius data. Yin et al. (2014) used longer SMOS SSS records to find that the magnitude, zonal extent, and the phase speed of equatorial 17-day TIWs decreased from 2010 to 2013, following the transition from a strong La Niña to non-La Niña conditions. Aquarius also helped to better identify the important contribution of salinity to the TIW energy budget (Lee et al., 2014), previously deducted from buoy observations (Grodsky et al., 2005). As shown, ignoring the SSS effect in the energy budget would under-estimate TIW-related Eddy Potential Energy (EPE) by a factor of three.

SMOS and Aquarius data were also used for the first time to characterize Rossby waves in SSS measurements. Westward salinity anomaly propagation induced by planetary waves was detected in Aquarius and SMOS SSS in the Indian Ocean (Menezes et al., 2014; Du and Zhang, 2015; Banks et al., 2016; Köhler et al., 2018) and North Pacific Ocean (Belonenko et al., 2018). In the southern Indian Ocean, the planetary wave structure is quite different in SSS and SSH anomalies, with the SSH reflecting mainly thermocline oscillations and the SSS being closer related to the dynamics of the mixed layer.

In addition to open ocean Rossby waves, SMOS and Aquarius revealed the SSS structure of major ocean fronts, including the Gulf Stream (Fig. 20), its meanders, and warm/cold-core rings (Reul et al., 2014b; Umbert et al., 2015) with unprecedented spatial and temporal resolutions. These examples may be extended by the monitoring of large scale to mesoscale salinity gradients in the Azores Current front region (Kolodziejczyk et al., 2015), as well as the monitoring of eddy dynamics of the Algerian Current in the western Mediterranean (Isern-Fontanet et al., 2016). Furthermore, combining satellite SSS and SST allows retrieving sea surface density and density compensated (so called spiciness) features even at mesoscales (Kolodziejczyk et al.,

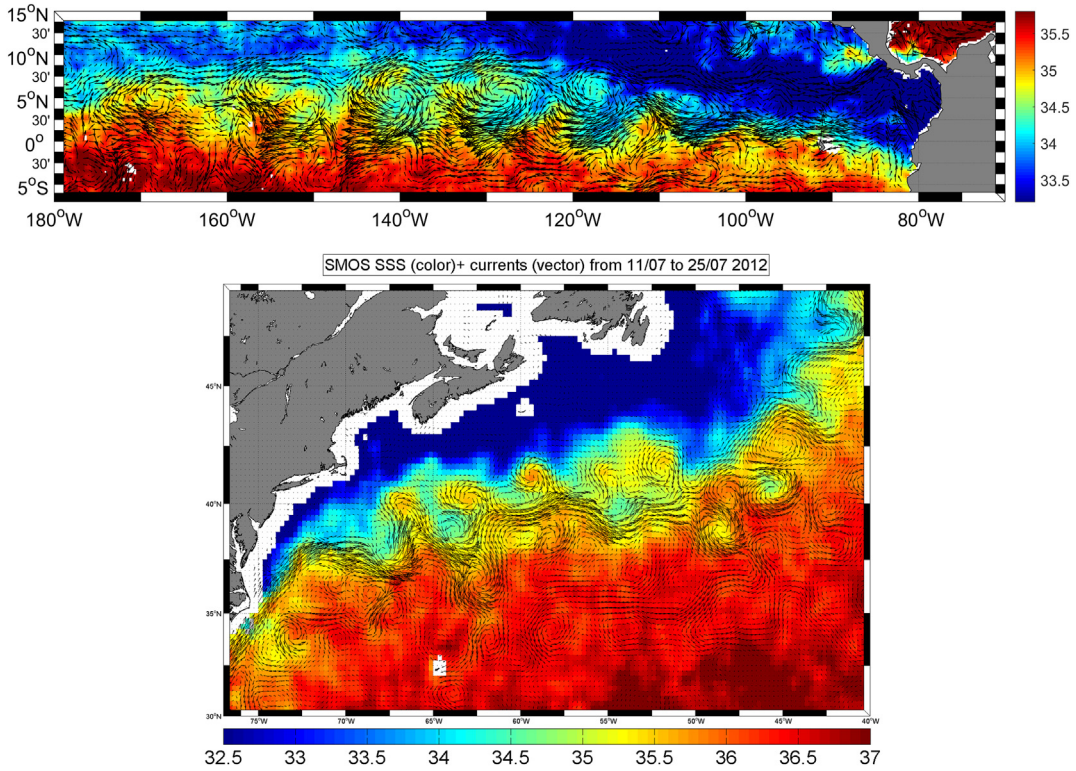

Fig. 20. (Top) SSS from SMOS (color shading) and surface currents (arrows) on Dec. 18, 2016 (9-day maps) showing Tropical Instability Wave signature in SSS. (Bottom) SMOS SSS (color shading), averaged from 11 to 25 July 2012 in the Gulf Stream region. OSCAR surface currents are indicated by black arrows.

2015). These derived quantities allow for assessing linkages between the water mass production and the ocean surface dynamics.

Satellite SSS firmly delineate current meanders that evolve in well-identified salty- (warm-) and fresh- (cold-) core rings, as illustrated in Fig. 20 for the Gulf Stream. Systematically higher correlation is found between SSS and SSH variability than between SST and SSH variability during warm seasons in the Gulf Stream and Azores Currents, a result of the mixed layer warming which masks the underlying structures in SST. Coherent signatures of mesoscale eddies in SSS and SSH were used by Melnichenko et al. (2017) to evaluate the eddy component of salinity advection. Their approach employed a covariance between satellite SSS and geostrophic current (SSH) variations, with the corresponding statistics at deeper layers inferred from Argo-based covariance between salinity and dynamic topography variations in eddy-following coordinates. Such estimates were conducted for two representative regions: the southern Indian Ocean and the North Atlantic subtropical gyre. For the first time, this provided a purely observational assessment of the role of mesoscale eddies in the ocean freshwater transport in the North Atlantic subtropical gyre. A similar composite analysis for the whole tropical Pacific (Delcroix et al., 2017) recently indicated that mesoscale variability in SSS accounts for 40 to 60% of the total variability in the central and eastern ITCZ region, providing new insight in the role of mesoscale eddies in the tropical mixed layer salinity budget.

Salinity fronts are common near river mouths. Satellite SSS shows that, in regions far away from coastlines, there exists an abundance of other types of SSS fronts, with significant, spatially concentrated salinity gradients (Martin, 2016; Kao and Lagerloef, 2015; Yu, 2015; Nyadjro and Subrahmanyam, 2016). The improved monitoring of these gradients thanks to satellite SSS reveal important dynamics between the ocean and atmosphere in tropical areas of importance for ENSO. As found by Yu (2015), the surface salinity minima in the tropical Pacific are thus not systematically located along the ITCZ maximum rainfall but along the poleward edges of SSS fronts, reflecting some impact of the upper ocean circulation on the SSS patterns. As revealed by combining satellite SSS surface signal and in situ data at depth, SSS fronts associated with the ITCZ penetrate down to 50–80 m and form a Salinity-Minimum Zone due to Ekman convergence of ITCZ-freshened surface waters. When the ITCZ starts seasonally moving southward, these fronts get detached from the main rain band and, due to wind-driven advection, keep propagating northward at ~3.5 km/day remaining detectable in next seasons (e.g. Grodsky et al., 2014b). Such studies emphasize the need to account for the impact of ocean circulation that normally plays a larger role in SSS anomaly patterns than does SST.

6.3. Satellite SSS and the water cycle

6.3.1. Satellite SSS as an ocean rain gauge?

It has long been assumed that, in many ocean regions such as tropical rain bands, patterns of rainfall and salinity are closely correlated, with low SSS induced by rainfall dilution (Wust, 1936). Surface salinity changes with coincident water cycle changes have been reported across various studies (e.g., Curry et al., 2003; Boyer et al., 2005; Hosoda et al., 2009; Durack and Wijffels, 2010; Helm et al., 2010; Durack et al., 2012; Skliris et al., 2014; Zika et al., 2015).

But, as seen from the previous section, such simple surface-driven 1D balance is complicated by ocean dynamics. To the first order, the large scale time-mean features of the freshwater cycle expressed as the Evaporation (E) minus Precipitation (P) budget (E-P) are indeed reflected in the time-mean SSS, with low SSS associated with tropical wet zones and high SSS associated with subtropical dry zones. Nevertheless, E-P extrema do not exactly collocate with salinity extrema (Vinogradova and Ponte, 2013b; Yu et al., 2017; Vinogradova and Ponte, 2017). This is an indication that the salinity is driven not only by the E-P but by the upper ocean dynamics as well. Satellite SSS has provided new insights into complex interplays between upper ocean salinity, atmospheric freshwater fluxes, and ocean circulation.

On one hand, in the rainy tropics and at very short time scales (less

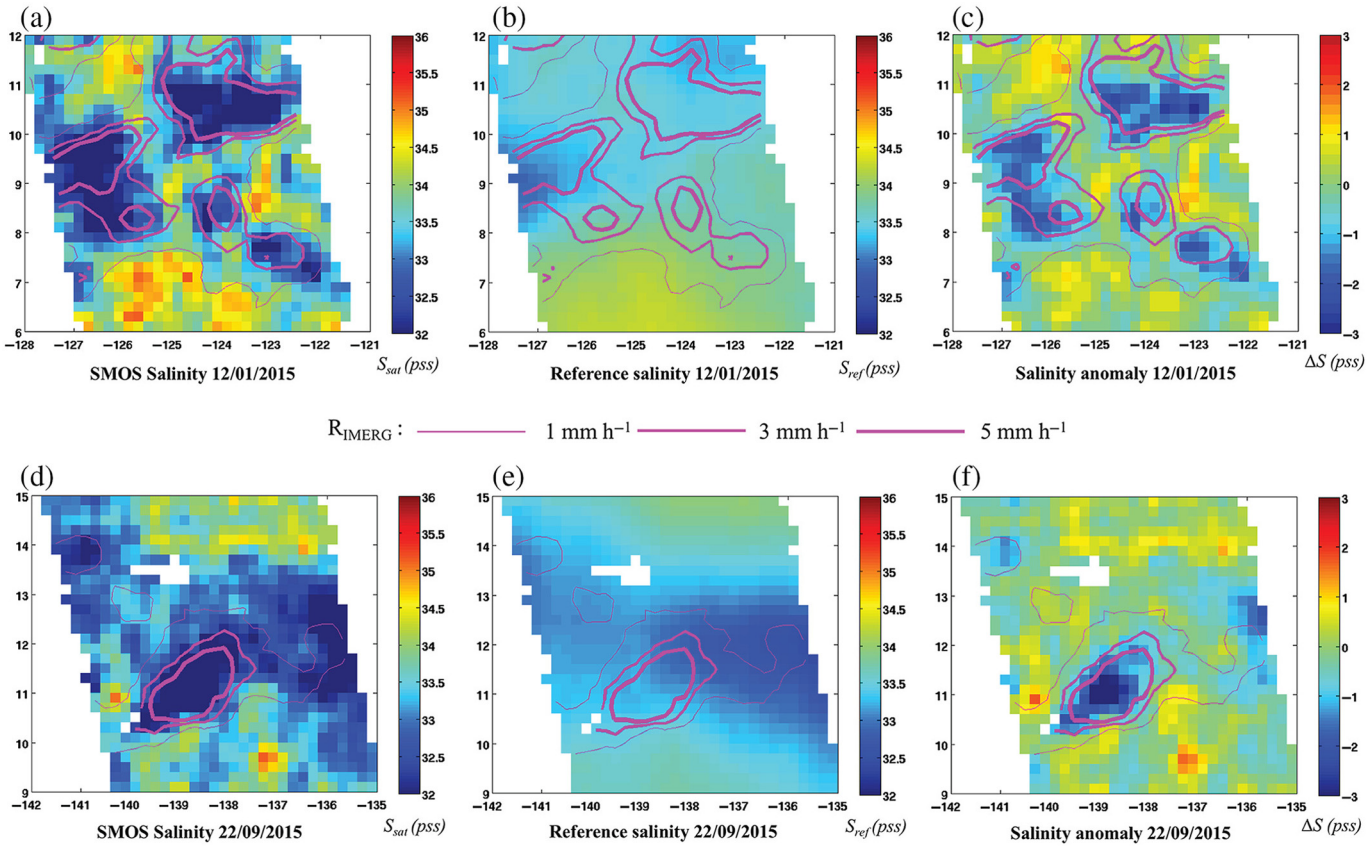

Fig. 21. SMOS ascending swath for two cases of rain-induced freshenings in the Tropical Pacific. (a–c) January 12, 2015 and (d–f) September 22, 2015. Left panels are showing the SSS measured by SMOS, middle are the reference SSS (mean of SMOS SSS in non-rainy conditions) and left is the SSSA. Magenta isolines are selected contours of Rain rate from IMERG (at 1, 3 and 5 mm/h). From Supply et al. (2018). (For interpretation of the references to color in this figure legend, the reader is referred to the web version of this article.)

than half an hour), the spatio-temporal SSS variability seems dominated by rainfall, with rain creating fresh lenses on top of the ocean (Boutin et al., 2016; Drushka et al., 2019). Satellite L-band radiometers are unique in detecting the very near surface salinity of the top centimeter (hereafter, S_{1cm}) and resolving rain-induced fresh lenses (Fig. 21), a piece of information not accessible by in situ global measurements, such as Argo. The quasi-linear relationship found between the surface freshening ΔS_{1cm} and the Rain Rate (RR) as detected in coincident (within < 1 h) satellite measurement has been highlighted in the Pacific ITCZ (Boutin et al., 2013, 2014). The freshening rate $\Delta S_{1cm}/\Delta RR \approx$ -0.2 pss/(mm/h), determined from satellite data at moderate winds (3–12 m/s) is consistent with the freshening rate derived from surface drifter data at 45 cm depth. Using the observed freshening rate, Supply et al. (2018) suggested an algorithm for RR estimation from instantaneous SMOS SSS measurements. If properly accounting for extremely short relaxation times (of the order of a few hours) due to mixing and advection, rain rate products based on instantaneous SSS anomaly observations can complement the existing rain products based on higher frequency microwave radiometry (e.g., GPM constellation).

But, this simplified approach cannot be directly applied to longer periods. As found by Yu (2014) and Yu et al. (2018), the SSS at longer time scales is not only affected by the local freshwater flux but by the ocean circulation as well (see also Tzortzi et al., 2016; Bingham and Lee, 2017). Although the source of the tropical upper ocean low salinity zone is the ITCZ rainfall, its behavior is also governed by the wind-driven Ekman dynamics (Yu, 2015). In fact, SSS variability is strongly affected by internal ocean processes such as mixing and currents (Bingham and Lee, 2017). As found from Aquarius SSS and collocated freshwater fluxes, the lack of correspondence between the dominant temporal and spatial SSS variability and the surface freshwater forcing confirms the key role of ocean processes in regulating SSS variability.

The existing uncertainty in ocean surface freshwater flux (E-P) is large, about 36% according to Yu et al. (2017), and is mostly attributed to the uncertainty in P in the tropical wet zone. As found by Köhl et al. (2014) and Yu et al. (2017), satellite salinity provides useful information to better constrain the E-P in several tropical areas, such as the eastern tropical Pacific east of 120°W, the eastern Atlantic east of 30°W, and the central southern Indian Ocean near 10°S. Nevertheless, only a small fraction of the global E-P variance can be directly explained by the local SSS variability, which complicates the potential use of satellite SSS for constraining atmospheric reanalysis estimates of E-P and would require a combination of SSS observations with ocean models. One way to reduce uncertainties in atmospheric reanalysis of E-P is through the inversion of the ocean state that is estimated based on the accurate ocean measurements of temperature, salinity, and sea level, guided by the dynamical constraints of the basic conservation principles (e.g., Fukumori et al., 2018; Vinogradova and co-authors, 2019). In particular, the use of salinity measurements proved to improve the estimates of air-sea fluxes, both the mean and time-varying surface fluxes of heat (Liang and Yu, 2016), freshwater, and runoff (Köhl et al., 2014).

6.3.2. *Large river plume variability monitoring*

Monitoring large river plume fresh water dispersal and mixing in the upper ocean is key for an ensemble of oceanographic processes, better characterization of air-sea and land-sea exchanges of water, heat, momentum, and sediment. However, in situ SSS data from global networks (e.g., Argo) are usually sparse in these highly dynamical zones. A common practice in ocean models is to use estimates of the seasonal climatology for river discharges. SSS variations near river mouths in ocean models typically have little interannual variations if not affected

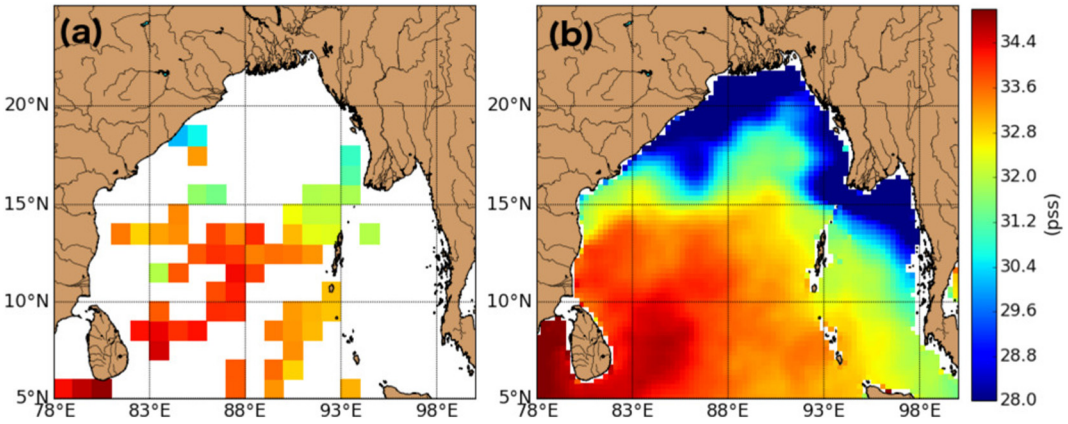

Fig. 22. (a) In situ SSS observations averaged over September to November 2015 within 1°x1° boxes and (b) SMAP SSS derived for the same period than in a). From Fournier et al., 2017a.

by strong currents. Being able to routinely monitor the dispersal patterns of large scale river plumes, satellite salinity based research of their spatial extension, mixing rates, and links with river discharge and land floods now has become feasible.

As detailed hereafter, the seasonal and interannual variations of SSS near major tropical river mouths have been extensively studied using satellite SSS data.

The Ganga-Brahmaputra river affects the seasonal SSS in the entire northern Indian Ocean (D'Addezio et al., 2015; Fournier et al., 2017a) and contributes significantly to the interannual SSS in the northern Bay of Bengal (Pant et al., 2015). While local variability of river runoff plays a pivotal role near the Ganga-Brahmaputra mouth, wind-driven interannual current anomalies associated with the IOD are responsible for a large fraction of interannual SSS throughout the entire basin (Akhil et al., 2016; Fournier et al., 2017a). As shown in Fig. 22, satellite SSS provides sufficient accuracy and spatial coverage of the Bay of Bengal to reveal a river-like fresh water dispersal along northwestern coasts of the bay (poleward of ~10°N).

Near river mouth and upstream seasonal and interannual SSS anomalies of the fresh Amazon/Orinoco river plume have been also extensively studied. A strong river plume salinification has thus been detected in 2012 (Grodsky et al., 2014a), caused by a deficit of rainfall over the inflow to the plume region in spring and a weaker North Brazil current in spring–summer. Satellite SSS sensors also helped to discover the presence of a local salinity maximum in the otherwise rainy northwestern tropical Atlantic during the low flow period of the Amazon river-runoff in winter (Grodsky et al., 2014b). Interannual SSS variations downstream of the Amazon/Orinoco plume in the Caribbean (Grodsky et al., 2015) and in the tropical Atlantic east of the Lesser Antilles (Fournier et al., 2017b) are all related to a number of dynamical causes, including variations of the Amazon River discharge, stochastic eddy-driven transport, and impacts of cross-shore winds on the plume dispersal.

SSS variability associated with the Mississippi (Gierach et al., 2013; Fournier et al., 2016a, 2016b; Rajabi et al., 2017) and Congo (Hopkins et al., 2013; Chao et al., 2015) river discharge has also been revealed using satellite SSS (Fig. 23). Strong interannual SSS freshening was observed at the Mississippi river mouth as responses to large-flooding events of the Mississippi River in 2011 and following the May 2015 Texas flood (Gierach et al., 2013; Fournier et al., 2016a, 2016b). As further demonstrated (Chao et al., 2015), combining the spatial area of strong negative SSS-discharge correlation together with the vertical length scale from nearby Argo casts allows for reasonable inferring of freshwater anomaly volume and anomalous river discharge.

Monitoring river plumes in cold waters is more challenging than in the tropics because of the reduced sensitivity to SSS in these conditions and the presence of both sea ice and land which both affect L-band T_B. Despite larger errors than in warm regions, large SSS gradients present in Arctic river plume regions and their seasonal/interannual variability were reported from satellite SSS products (Matsuoka et al., 2017; Tang et al., 2018; Olmedo et al., 2018b). In the Kara Sea, both SMAP and SMOS SSS show a consistent response to seasonal and interannual discharge variations in the Ob and Yenisei rivers (Kubryakov et al., 2016), thus providing an assessment of runoff impact in a region where no, or very little, in situ salinity data are available.

6.4. Satellite SSS and air-sea interactions

6.4.1. SSS, barrier-layers, and tropical cyclones

Besides polar oceans, the large scale upper ocean density stratification is primarily controlled by temperature variations at thermocline depths. However, there are multiple pieces of evidence that, in river plumes and rain-diluted areas, salinity variations can also regulate the mixed layer (e.g., Lukas and Lindstrom, 1991). The near-surface ocean heat budget and its exchanges with the atmosphere can be affected by the presence of the so-called barrier layer (BL). The BL extends between the halocline and the thermocline and forms in the presence of a shallow fresh lens located on top of the isothermal well-mixed layer. By increasing the upper ocean water stability, the BL limits the depth of penetration of the wind-driven mixing and attenuate the turbulent cooling from below. This vertical exchange attenuation promotes higher SST and consequently impacts many aspects of tropical convection, including the ENSO dynamics (Maes et al., 2002, 2005). Heavy precipitation and large tropical river plumes are among the main mechanisms accounting for the BL formation.

Combined with in situ profile of salinity and temperature, the new satellite SSS data allow refinement of our knowledge of the co-variability between SSS, BL thickness (BLT), as well as subsurface thermohaline properties (e.g., density stratification) in various regions of the tropical oceans. Geographical distribution and temporal variability of BL properties inferred from satellite SSS have been demonstrated along the western tropical Pacific warm pool SSS front (Qu et al., 2014), western tropical Atlantic (Moon and Song, 2014; Reul et al., 2014c), and Indian ocean (Felton et al., 2014; Moon and Song, 2014; Sengupta et al., 2016; Köhler et al., 2018). The established regional surface-to-subsurface relationships can be used to infer maps of subsurface properties from satellite SSS, such as BLT (Felton et al., 2014), mixed layer depth (Schlundt et al., 2014; Köhler et al., 2018), as well as haline and thermal stratification parameters (Schiller and Oke, 2015; Su et al., 2015; Chen et al., 2017; Reul et al., 2014c).

When Tropical Cyclones (TC) pass over oceanic regions with thick BLs (> 10 m in the north western tropical Atlantic), the increased stability and stratification of the ocean reduce TC-induced vertical mixing and resulting SST cooling that causes a faster TC growth

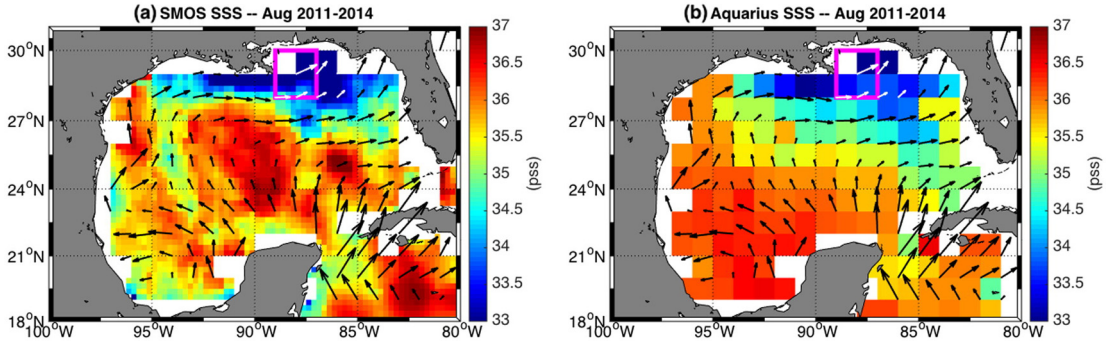

Fig. 23. Monthly averaged composite of (a) SMOS and (b) Aquarius SSS over 2011–2014. Arrows indicate the corresponding OSCAR currents. The pink box indicates an area where the SSS correlate well with the Mississippi river discharge. From Fournier et al., 2016a. (For interpretation of the references to color in this figure legend, the reader is referred to the web version of this article.)

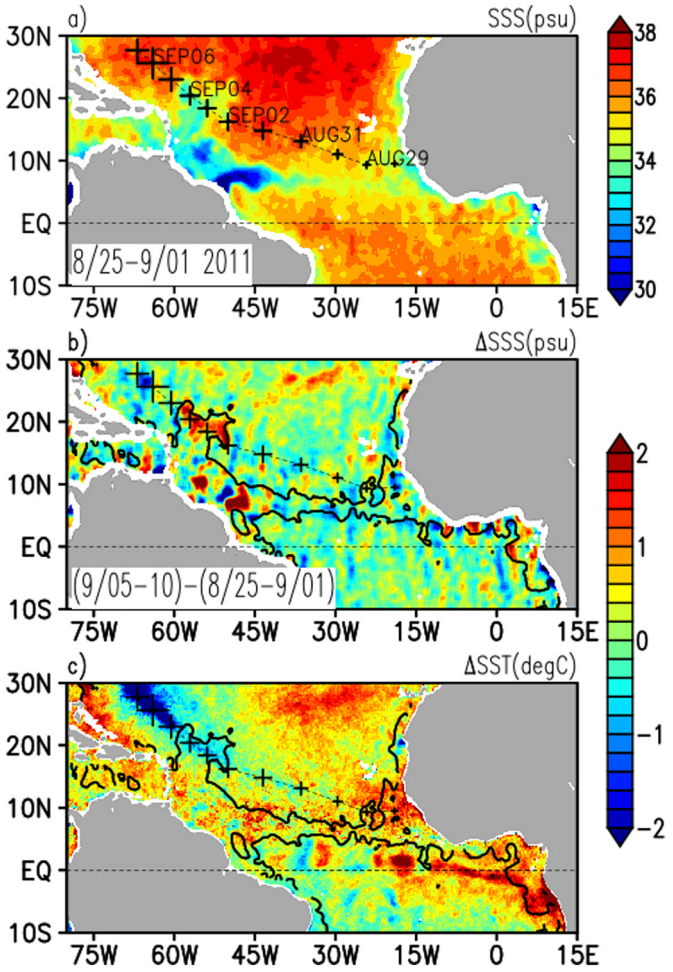

Fig. 24. (a) SSS estimated from SMOS temporally averaged over 25 august–1st September 2011, prior the passage of hurricane Katia. The storm track is indicated by crosses, the larger the more intense the storm. Map of the mean temporal evolution in SSS (b) and SST (c) from before to after the hurricane passage. The isohaline at 35 pss before the passage of Katia is indicated by the black contour.

(Balaguru et al., 2012). Grodsky et al. (2012) have first shown that SSS observations from Aquarius and SMOS satellites help to detect the ocean haline response to TCs. This was demonstrated for hurricane Katia, which crossed the Amazon plume in the early fall of 2011. Its passage over the plume produced a 1.5 pss salty wake covering > 10^5 km^2 (with density impact corresponding to a 3.5 °C SST cooling) induced by the mixing of the fresh surface layer of the plume with saltier subsurface waters. The extra work needed to destroy the BL diminishes the depth of hurricane-induced mixing penetration and decreases SST cooling in the plume, and thus preserves warmer SST and higher evaporation than outside the plume. Fig. 24 suggests this by illustrating that hurricane-induced cold wake apparently amplifies once the hurricane leaves the plume area. Reul et al. (2014c) have later found that additional stability associated with haline vertical stratification in BLs can systematically cause ocean hurricane-induced cooling reduction by ~50% over the plume area for the most intense cyclones, compared to the surrounding open-ocean waters, especially for plume vertical stratifications with shallow isothermal layers (Rudzin et al., 2018).

Alternatively, the near-surface BL physics associated with freshwater export is a key mechanism responsible for 'hot spot' SSTs in the western tropical Atlantic, which produce favorable conditions for TC rapid growth. Regional BLs are spatially correlated with the North Brazilian Current (NBC) warm core rings that is confirmed by sample aircraft-dropped profiler data (Rudzin et al., 2017). By providing a unique monitoring of the river plume extent, satellite SSS used in conjunction with SST greatly help to better quantify tropical cyclone upper ocean coupling with potentially important implications for TC intensity forecasting.

6.4.2. *Satellite SSS and equatorial upwellings*

A striking feature of the Pacific and Atlantic oceans is the equatorial SST minimum extending from the coast of the Americas into the central Pacific, and from the African coasts to approximately 20°W, respectively: the so-called equatorial 'cold' tongue (Wyrtki, 1981). Salinity, temperature, nutrient, and water color distributions (e.g., Grodsky et al., 2018a) in these vast areas of net heat uptake by the ocean are the result of geostrophic equatorward convergence into the Equatorial Undercurrent (EUC) and subsequent wind-driven upwelling above (Knauss, 1966). The upwelled subtropical water can modify the tropical SST and SSS. The upwelling thus can affect the zonal SST gradient, itself coupled to the Walker circulation via the Bjerknes feedback (Bjerknes, 1969).

Mixed layer salt budget analysis suggests that decadal Atlantic cold tongue salinity variations are driven mostly by the vertical exchanges and mixing, in turn, driven by the magnitude of the zonal wind component (e.g. Grodsky et al., 2006). However, the processes that control the sub-seasonal variability in intensity and extent of the cold tongue and its salinity variability remains poorly known. It has been shown that new satellite SSS data detect well the seasonal variability of these salty/cold tongues (Alory et al., 2012; Schlundt et al., 2014; Maes et al., 2014; Da-Allada et al., 2017). Interannual SSS signatures of the tongues are not systematically phased with the upwelling signatures observed in SST and SSH data. In the Atlantic sector, this lack of correlation is affected in part by ENSO teleconnections that modulate equatorial rainfall and SSS (Grodsky and Carton, 2018).

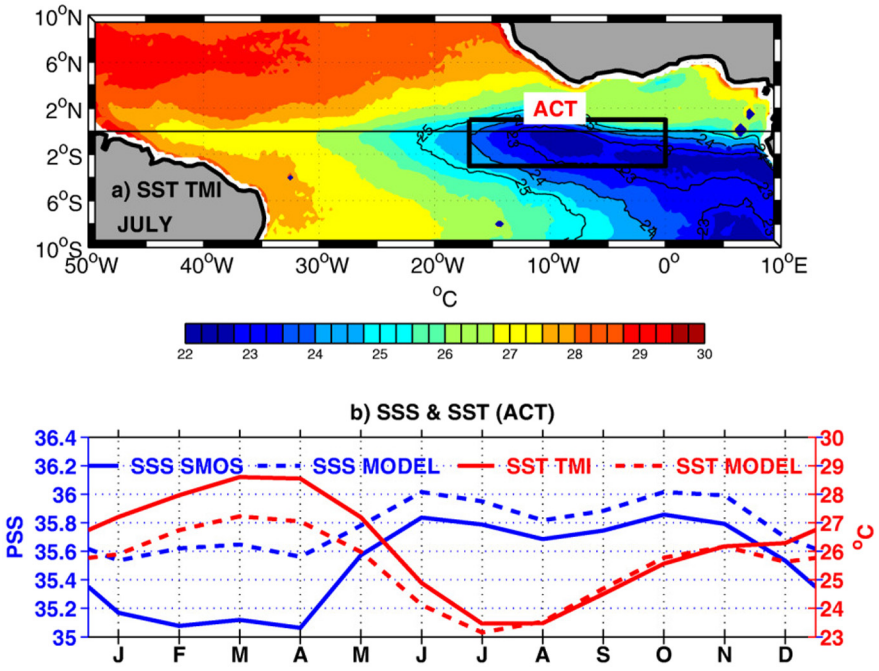

Fig. 25. (a) Averaged map of the microwave (TMI) SST [°C] in July in the equatorial Atlantic. Contour levels are at 23, 24, and 25 °C. The black contoured box indicate the equatorial Atlantic Cold tongue (ACT) study area. (b) Seasonal change of SSS (blue curves) and SST (red curves) in the ACT region averaged over 2010–2012. Satellite data (solid); Model data (dashed). From Da-Allada et al., 2017. (For interpretation of the references to color in this figure legend, the reader is referred to the web version of this article.)

More insights into the physical processes involved have been gained thanks to satellite SSS (Da-Allada et al., 2016) which help to better characterize the cold tongue subseasonal variability. The seasonal cycle of the SSS in the cold tongue and accompanying wind forcing is robust and is related to the seasonal march of the ITCZ and related changes in the strength of equatorial easterlies (Fig. 25). From December to April, when the ITCZ is close to the equator, the surface freshwater flux acts to decrease the SSS while the rest of the year, evaporation dominates in the Atlantic cold tongue and increases the SSS. The occurrence of an SSS maximum one month ahead of the SST minimum has been observed and better characterized thanks to the new satellite SSS. As found (Schlundt et al., 2014; Da-Allada et al., 2016), the boreal spring SSS maximum is mainly explained by an upward flux of high salinity originating from the core of the Equatorial Undercurrent (EUC) through vertical mixing and advection. The vertical mixing contribution to the mixed layer salt budget peaks in April–May. It is controlled primarily by (i) an increased zonal shear between the surface South Equatorial Current and the subsurface EUC and (ii) the presence of a strong salinity stratification at the mixed-layer base from December to May. This haline stratification that is due to both high precipitations below the Inter Tropical Convergence Zone and zonal advection of low-salinity water from the Gulf of Guinea explains largely the SSS seasonal cycle.

6.5. Satellite SSS and ocean bio-geochemistry

The marine ecosystem and ocean carbon cycles are both strongly influenced by ocean circulation that, in turn, is affected by salinity. The SSS is an important factor shaping the spatial distribution of upper ocean biogeochemical parameters, both through its influence on ocean circulation and its relationship with rainfall (Turk et al., 2010; Brown et al., 2015) and river discharge (Lefèvre et al., 2010; Salisbury et al., 2011). Combined with ocean color products, the satellite SSS permits documentation, in a new and improved manner, the spatial coherence among river discharge, salinity, and bio-optical properties (Colored Dissolved Organic Matter (CDOM), chl-a, light absorption parameter at 490 nm) and exploration of its nature (Salisbury et al., 2011; Reul et al., 2014b; Fournier et al., 2015; Korosov et al., 2015; Matsuoka et al., 2017; Rajabi et al., 2017; Da Silva and Castelao, 2018; Dzwonkowski et al., 2018). The combined data also help to document the temporal and spatial variability of bio-optical and salinity properties of evolving low-salinity plumes and explore their departure from the conservative mixing with open ocean waters. The relationships between SSS and bio-optical properties in river plumes can now be systematically studied from satellite observations as shown in Reul et al. (2014a) for the Amazon/Orinoco, Niger, and Congo River plumes. The absorption coefficient of colored detrital matter (acdm), chlorophyll-a concentration, and SSS were found strongly negatively correlated near to the mouth of the Congo (Hopkins et al., 2013; Reul et al., 2014a), Amazon (Reul et al., 2014a; Fournier et al., 2015; Korosov et al., 2015), Niger (Reul et al., 2014a), Mississippi (Rajabi et al., 2017; Da Silva and Castelao, 2018), and the main Arctic rivers (Matsuoka et al., 2017) rivers.

Thanks to newly established conservative mixing linear laws relating bio-optical parameters with SSS, its distribution in river plumes can now be more accurately retrieved at high resolution from proxy visible data in cloud-free conditions (Fournier et al., 2015; Korosov et al., 2015; Chen and Hu, 2017). Combined with ocean color observations, the satellite SSS can also be used to better discriminate water sources from space, such as demonstrated for the Arctic by Matsuoka et al. (2017) who have shown that seawater, ice melt water, and river water can be better identified from combined SSS and ocean color spaceborne observations than from ocean-color alone.

While it has been proven that it is difficult to use the remote sensing for direct monitoring of seawater pH and its impact on marine organisms (Sun et al., 2012), some key variables of the carbonate system can be empirically inferred from satellites SST, SSS, and Chl-a, using relationships derived from in situ data. As demonstrated, the satellite SSS provides new resources for enhancing the oceanic carbon cycle and ocean acidification studies (Sabia et al., 2015, 2018; Salisbury et al., 2011, 2015; Land et al., 2015; Brown et al., 2015; Fine et al., 2017; Land et al., 2019). In particular, Brown et al. (2015) have highlighted the dominant roles of the upwelling and freshwater fluxes in driving the air-sea CO2 flux variability in the northeastern tropical Pacific Ocean. Another key characteristic that strongly correlates with salinity is the Total Alkalinity (TA), which is an important parameter for the carbon cycle and the monitoring of ocean acidification (Lee et al., 2006). Merging SST and SSS data provides an unprecedented possibility to map the TA from space (Fig. 26), even in challenging areas such as the Mediterranean Sea (Sabia et al., 2018).

Comparison of satellite-derived TA with its climatology has shown

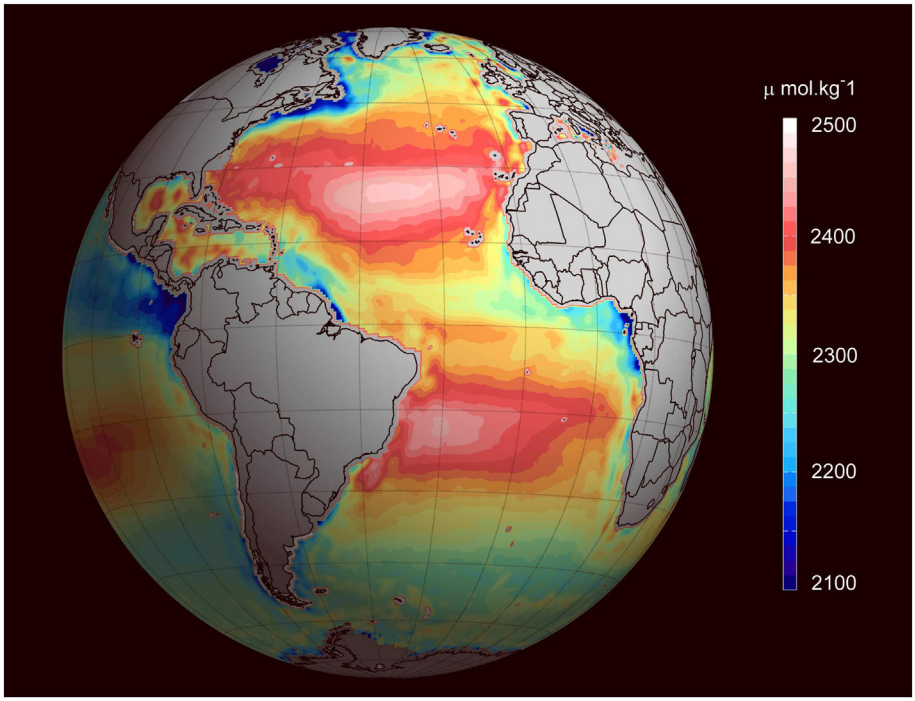

Fig. 26. Ocean total alkalinity map derived from surface temperature and salinity measurements (averaged between 2010 and 2014) from several satellites, including ESA's SMOS mission.

for the first time that TA is increasing in high evaporative subtropical regions, which is consistent with what is known about concurrent changes in the global water cycle (Fine et al., 2017). The combined use of satellite ocean color, SST, and SSS data is also exploited as a means of satellite detection of surface Dissolved Inorganic Carbon (DIC) and ocean pH in several ocean regions (Land et al., 2015; Sabia et al., 2015).

7. Synthesis on the first decade of the satellite SSS era

As initially devised, global satellite SSS observations have unlatched essential means to better reveal the influence of salinity on ocean circulation, bio-geochemistry, its relations to climate variability, air-sea interactions, and the global water cycle. In addition, satellite SSS enables better monitoring of the terrestrial and open ocean water cycle connections, through runoff and other anomalies (Li et al., 2016a, 2016b; Chen et al., 2019). Today, SSS is operationally retrieved, becoming one of the last key ocean-related ECVs.

The new satellite SSS era started with the Soil Moisture and Ocean Salinity (SMOS) mission, launched in 2009 under the auspices of the European Spatial Agency (ESA), the French Centre National d'Etudes Spatiales (CNES), and the Spanish Centre for the Development of Industrial Technology (CDTI). Followed by the National Aeronautics and Space Administration (NASA) Aquarius instrument from mid-2011 to mid-2015, it is today complemented by the NASA Soil Moisture Active-Passive (SMAP) mission. Initially dedicated to Soil Moisture measurements only, SMAP applications have been extended to include the SSS, which is available since early 2015. All instruments on-board these different missions follow an early 1970s historical heritage that demonstrated how passive microwave radiometer observations in the L-band (frequency ~1.4 GHz, wavelength ~21 cm) could be used to retrieve SSS.

As reviewed in the second section of this paper, the SSS measurement principle was successfully developed and demonstrated in the 1970s from various platforms (land-based bridge, aircrafts, towers, short-lived satellites, etc). The long delay until the final development and launch of the first satellite salinity sensor was mainly dictated by technological challenges associated with space delivery and deployment of large antennas. Indeed, to achieve a proper pixel resolution, a very large size (~3–8 m) radiometer antenna is needed for 1.4 GHz operations even from low polar orbits. As discussed (Section 3), there are major technological differences but also similarities between the three first satellite salinity missions. SMOS and SMAP spatial resolution (~40 km) is a factor 2–3 higher than Aquarius spatial resolution (~100 km - 150 km).

Moreover, with their large swaths, observations cover almost the full globe in 3 days, while 7 days were needed in the case of Aquarius. Yet, Aquarius radiometric noise was significantly lower than SMOS or SMAP radiometric noise. For SMOS, image reconstruction errors are sources of specific and variable noise in the T_B images (e.g., sun and land image aliasing in ocean scenes, noise floor errors …) and impact the quality of retrieved SSS from this sensor. But SMOS multi-angular viewing capability also provides a way to mitigate the noise in individual samples, thanks to a large number of T_B acquisition for a given ocean target pixel. The Aquarius antenna emissivity was negligibly small, while the SMAP mesh reflector has an emissivity of about 0.2%, which needs to be accounted for in salinity retrieval. Moreover, the simultaneous acquisition of scatterometer and radiometer observations by Aquarius significantly helped to improve the correction for sea surface roughness effect. For SMOS and SMAP, retrieval algorithms must rely on external surface wind vector data, not always of sufficiently high quality to well characterize the actual impact of roughness on L-band passive sensors.

The basic physical principles of SSS remote sensing from L-band radiometers have been reviewed in Section 4. The seawater dielectric constant model function at L-band, a key component of all SSS retrieval algorithms, is still uncertain, particularly at low (< 8 °C) and high (> 28 °C) SST. While new laboratory measurements have recently been presented (Lang et al., 2016; Zhou et al., 2017), additional measurements are still needed. In that context, comparative analyses between observed SMOS, Aquarius, and SMAP measurement dependencies as a function of SSS and SST are being performed in the context of the ESA Climate Change Initiative-Sea Surface Salinity project (CCI-SSS, http://cci.esa.int/salinity). This is necessary to properly combine the data from SMOS, Aquarius, and SMAP missions in order to produce the

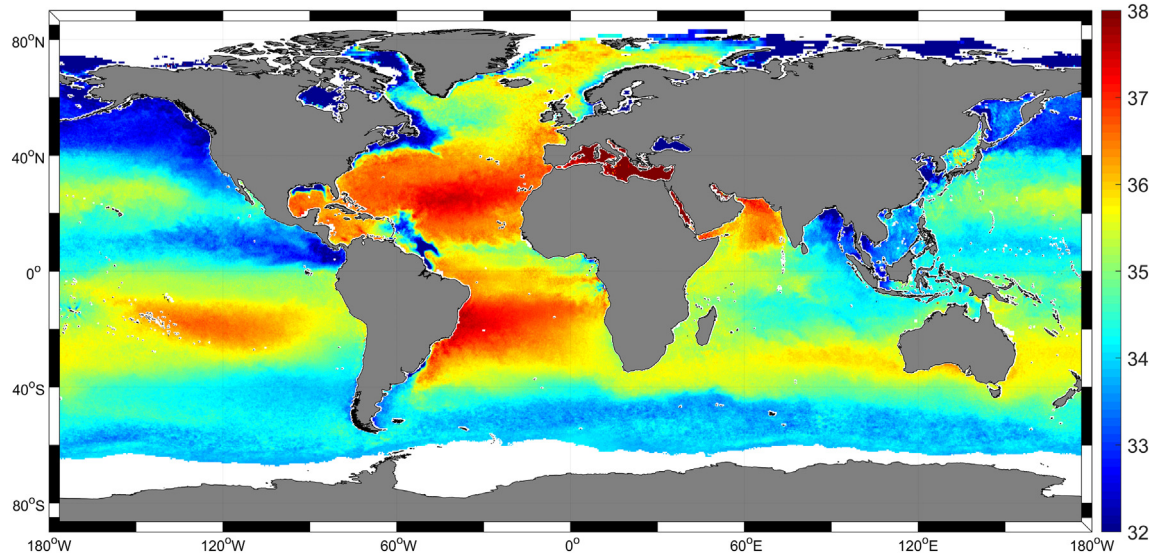

Fig. 27. Monthly average map of the ocean surface salinity for the month of July 2015 generated by the ESA Climate Change Initiative project. The 10 years-long CCI-SSS time series is obtained by merging the salinity data from the SMOS, Aquarius, and SMAP.

longest possible satellite SSS Climate Data Record. A first merged SMOS-Aquarius-SMAP product covering the full Satellite SSS era is currently being distributed by the project to the community (see Fig. 27).

Both laboratory dielectric constant measurements and the CCI-SSS efforts will help to rapidly reach a community agreement about the particular sea water dielectric constant model to be used in the L-band. The current status in the development of forward models to estimate and correct for the sea surface roughness contribution to L-band T_B measured at antenna level was also reviewed. To first order, Geophysical Model Functions (GMF) developed are dependent on the surface wind speed. There is a good agreement between L-band GMFs used in the latest versions of Aquarius, SMAP, and SMOS products (V5 for Aquarius, RSS V3 for SMAP, JPL V4 for SMAP and ESA V662 for SMOS) (Yin et al., 2016; Meissner et al., 2018).

As mentioned above, in the case of Aquarius, the direct use of scatterometer measurements significantly improves the accuracy of the surface roughness correction. While there is a consensus on the first-order wind-speed dependencies of the GMFs, the wind direction signature, the wave impact (significant wave height, wave-age), and the air/sea temperature dependencies of this correction still exhibit significant differences.

Remaining uncertainties for these second order effects are still the subject of on-going research efforts, and are also being considered within the ESA Climate Change Initiative-SSS project. Corrections associated with ionospheric, atmospheric, solar, and sky radiation contributions to the antenna measured brightness commonly involve the use of the ratio of the third Stokes (U) parameter to the difference between the vertical and horizontal polarization channels. This helps to infer the rotation angle (geometry plus Faraday) across the ionosphere. Again, accurate calibration of the third Stokes parameter is still challenging, particularly for the SMOS interferometer. The ionospheric rotation estimates also rely on the first guess data, including the total electronic content and geomagnetic field data (Vergely et al., 2014).

For L-band, sources of atmospheric attenuation are due to absorption by oxygen, water vapor, and liquid water. The contribution from the atmosphere is found to be a few Kelvins on average, rather stable in space and time, with the dominant source of signal associated with oxygen. As presently implemented, atmospheric corrections used in salinity retrieval algorithms all rely on time interpolated and integrated vertical profiles of atmospheric pressure, temperature, relative humidity, and cloud water mixing ratio obtained from numerical weather forecast models (ECMWF or NCEP).

The overall error in salinity retrievals due to the atmosphere is estimated to be < 0.2 pss (e.g., Meissner et al., 2018). Correcting for the Sun and Sky direct and reflected radiation further demands accurate characterization of the antenna patterns, and sun, and sky T_B at the time of acquisition. Models for the bi-static scattering coefficients of the sea surface at L-band are then also needed. Sun flux measurements made by the United States Air Force Radio Solar Telescope Network are used but remain uncertain to within 10%, which is significant for salinity retrieval algorithms as the Sun is an extremely bright source at 1.4 GHz ($\sim 10^6$ K). Bi-static sea surface scattering coefficient models are generally estimated using the Physical Optics (Reul et al., 2007) or the Geometric Optics approaches (Meissner et al., 2018). A practical rule for L-band measurements is to consider a reduced, by about 50%, surface slope variance as a function of wind speed, as compared to optical data. Applied corrections remove the reflected galactic radiation correctly to about 90% as estimated in the Aquarius and SMAP cases (e.g., Meissner et al., 2018). Remaining uncertainties from the rough ocean surface scattering models in the L-band, the T_B map of the celestial sky, and the antenna gain pattern appear as sources of remaining ascending-descending biases in all the satellite data. Empirical corrections to best mitigate these remaining signals are currently under investigation. They are based on either alternative antenna gain-weighted sky maps obtained from the satellite data or rely on the multiple view capabilities of the instrument (e.g., use of the fore and aft-look for SMAP). Antenna gain-weighted sky maps can be derived from the accumulated radiometer direct observation of the sky as recorded during the regular cold-sky calibration maneuvers.

Being significantly warmer than the ocean water at L-band, land surfaces can significantly impact the ocean T_B measured, and this over a 400 to 1000 km-wide band off the coasts of the major land masses. A correction for land entering the antenna side-lobes when the sensor observation gets close to the land has been derived from simulated T_B (Spurgeon et al., 2017; Meissner et al., 2018). Such empirical corrections appear to be efficient globally to reduce the land-contamination biases in satellite SSS.

Yet, uncertainties remain in the antenna gain patterns and the reference geophysical fields (e.g. coastal SSS, land T_Bs), which are used to model the expected ocean-land transition signal. Alternatively, corrections can also be successfully applied after the SSS has been retrieved from the uncorrected T_B. These corrections, based on filtering largely biased estimates, are empirical adjustments, or based on advanced

filtering of the salinity products (e.g., Boutin et al., 2018; Olmedo et al., 2017, 2018a). Accordingly, while the absolute salinity retrievals can degrade quickly as the footprint approaches land, the SSS Anomalies (SSSA) derived from satellites generally show coherent and informative signatures in many coastal zones (Boutin et al., 2018; Grodsky et al., 2018a, 2019).

An overview of the satellite SSS products quality assessment is presented in Section 5. The three sensors exhibit Root-Mean Square Differences (RMSD) with in situ data (SSS_{SAT}-SSS_{insitu}) ranging within 0.15–0.25 pss for ~2 weeks or monthly time scale and within 0.25°x0.25° to 1°X1° boxes in the mid and tropical latitudes and sufficiently far away from coasts, and thus fulfill the objectives of the GODAE requirements.

All satellite sensors show degraded SSS quality in cold waters at high latitudes. These reduced accuracies are related to the loss of sensitivity, remaining uncertainties on the dielectric constant model, the correction for roughness in the stormy high latitude conditions, and the presence of land (Arctic) and sea-ice, and to the presence of RFI (Northern latitudes).

All three sensors also show residual seasonal and latitudinal large-scale biases, due to instrument thermal drifts and solar effects which are tentatively corrected empirically using different reference fields (HYCOM, Argo Optimal Interpolation). Finally, SMOS and Aquarius data are less capable of detecting Radio Frequency Interference (RFI) than SMAP (e.g., Asia coastlines, the Bay of Bengal, Arabian and Mediterranean Seas). The SMAP sensor is equipped with a dedicated on-board RFI filtering device, hence providing unprecedented monitoring of main river plumes in the vicinity of continents (e.g. Fournier et al., 2016a, 2016b, 2017a, 2017b). On the other hand, the calibration of the SMAP instrument is more difficult than for Aquarius (Fore et al., 2016; Meissner et al., 2018) and requires empirical adjustments in the SMAP salinity retrieval algorithms. As such, the absolute value of SMAP SSS may remain imprecise to about 0.2 pss in low to mid-latitudes of the open ocean (Fore et al., 2018). While challenges still exist in the calibration, retrieval algorithms, and validation process, largely due to in situ measurement sparsity, satellite measurements now routinely provide essential means to help major scientific achievements (as reviewed in Section 6).

Thanks to their global coverage, frequent revisit time, upper ocean first centimeter-depth sampling, the unique data from SMOS, Aquarius, and SMAP missions largely transform and improve our knowledge of the global SSS field. Observations provide a piece of new information on its variability at spatial and temporal scales that were not globally accessible before. In particular, satellites reveal large-scale SSS anomalies linked to climate variability, such as ENSO, the Indian Ocean Dipole, and the Madden Julian Oscillation among many others. In addition, L-band radiometers sample the very near surface and therefore provide for the first time global information on the upper ocean response to atmospheric freshwater fluxes. In some ways, this remains a vivid challenge at the level of individual measurements to fully unravel the complex and relatively rapid geophysical processes that define the SSS in the upper 1 cm. This remains an area of on-going research (e.g., Wurl et al., 2019). Complementary to other in situ SSS observing systems, satellite salinity also provide systematic monitoring of features with both smaller spatial scales (< 100 km) and shorter periods (less than a month), crucial to help determine cross-scale ocean-land-atmosphere interactions (fronts, large-scale eddies, meanders, fresh river plume dispersal, planetary and tropical instability waves, etc.).

The SMAP and SMOS salinity products are reaching a relatively high skill level with temporal consistency to help identify anomalous mooring data and inadequate temporal sampling in the Argo-monthly-gridded and ocean circulation model products. Satellite SSS gives more uniform spatio-temporal sampling and improves the ability to estimate horizontal gradients which is important for frontal genesis, eddy-mean flow interaction, and biogeochemistry.

Despite being less sensitive to SSS in the cold waters than in the warm tropical seas, the data from L-band spaceborne radiometers have also been uniquely exploited to monitor fresh water plumes in the Arctic region, as well as large changes in fresh water content associated with seasonal changes in sea ice extent, providing an unprecedented monitoring in regions very poorly covered by in situ measurements.

Needless to say, retrieving coastal region SSS from L-band radiometers remains challenging due to land contamination and elevated level of regional RFI. These artefacts have stronger impacts on the SMOS mission that employs an interferometric L-band radiometer than on the NASA Aquarius and SMAP real aperture systems.

While often biased in the proximity of land masses, recent studies evidenced that salinity anomaly fields derived from satellites can nevertheless provide very useful information on the SSS variability in closed basins (e.g., in the western and eastern Mediterranean sea (Grodsky et al., 2019)) and in some regional shelf seas (e.g., southwestern and northwestern Atlantic shelf, Gulf of Maine).

Despite these scientific achievements and numerous demonstrations, the continuity of L-band passive microwave satellites remains uncertain. Today, satellite SSS is a key ECV for both the Global Climate Observing System (GCOS) and the Global Ocean Observing System (GOOS). As summarized by Vinogradova and co-authors (2019), the user community highlighted the essential need to provide necessary continuity for SSS measurements from space for a variety of scientific research and operational applications, with at least the same resolution and accuracy than for the current satellite missions (SMOS and SMAP).

Following a European Commission's recent user consultation, ESA is currently studying the technical feasibility and financial requirements for a fleet of High Priority Candidate Missions. The prepared missions will expand the European Union's Copernicus Programme. In that context, a five-channel wide swath (> 1900 km) conically scanning microwave radiometer called the Copernicus Imaging Microwave Radiometer (CIMR, Donlon, 2018) is being studied. CIMR will deploy a large rotating (rotation speed ~8.2 rpm) mesh antenna with a 6-8 m diameter, building on the risk-reduction activities of NASA SMAP to provide a large coverage and daily repeat. CIMR includes a dedicated L-band channel with a target NEdT of 0.3 K to provide Level 2 products including SSS, thin sea ice concentration, and surface wind speed at the spatial resolution of 40–60 km.

CIMR would further include channels at 6.9 GHz (NEdT of 0.2 K, resolution 15 km), 10.65 GHz (NEdT of 0.3 K, resolution 15 km), 18.7 GHz (NEdT of 0.3 K, resolution 5 km) and 36.5 GHz (NEdT of 0.8 K, spatial resolution 5 km) and will operate in a 06:00 dawn-dusk orbit to provide 95% global coverage every day. As foreseen, CIMR will fly in the 2027 time frame which could ensure continuity for L-band measurements at the comparable spatial resolution to the current SMOS and SMAP measurements.

Finally, new technological research is also ongoing to further improve both the spatial resolution using new interferometry techniques (Soldo, 2013; Kerr et al., 2018), as well as the accuracy of the measurement (e.g. by extending the range of wavelength to lower frequencies than L-Band, such as P-band as suggested in Lee et al., 2016).

Declaration of competing interest

The authors declare that they have no known competing financial interests or personal relationships that could have appeared to influence the work reported in this paper.

Acknowledgements

We would like to thank the contributions from three anonymous reviewers for comments and detailed editing of our draft which definitively helped to improve the paper.

The EU authors acknowledge support of ESA in the frame of the SMOS ESL Level 2 phase 3 contract (https://smos.argans.co.uk/), the

SMOS Pilot-Mission Exploitation Platform (Pi-MEP) project (https://www.salinity-pimep.org/), and the Climate Change Initiative (CCI) project (http://cci.esa.int/salinity). French authors thank the support of the Centre National d'Etudes Spatiales (CNES) in the frame of the Centre Aval de Traitement des Données SMOS (CATDS, http://www.catds.fr) and of CNES-TOSCA SMOS-Ocean projects.

US authors thank the support of the NASA Ocean Surface Salinity Team (OSST).

SMAP CAP SSS is produced at Jet Propulsion Laboratory. Thomas Meissner and Frank Wentz acknowledge funding from NASA (contracts no. NNG04HZ29C, NNH15CM44C, 80HQTR18C0015, and JPL subcontract 1602331). SMAP RSS/NASA SSS is produced at Remote Sensing Systems. It is available on https://podaac.jpl.nasa.gov/SMAP. Aquarius SSS was produced at NASA GSFC Aquarius Data Processing System. It is available on https://podaac.jpl.nasa.gov/aquarius.

Appendix A. List of satellite SSS products available in January 2020

Dataset name	Level	Spatial resolution	Temporal coverage	Variables	Version	Provider
		Temporal resolution	Update frequency			
SMOS SSS L2 v662 (ESA)	L2	30–80 km 50-minute half-orbit (granule duration)	From 2010-05-01 to present Daily	SSS1	v662	ESA
SMAP SSS L2 v4 (RSS)	L2	~70 km (grid 0.25°x0.25°) 98-minute orbit (granule duration)	From 2015-03-27 to present Daily	sss_smap	v4	RSS
SMAP SSS L2 v4.2 (JPL)	L2	~60 km (25 km swath grid) 98-minute orbit (granule duration)	From 2015-03-27 to present Daily	smap_sss	v4.2	JPL
Aquarius SSS L2 OR v5 (NASA-GSFC)	L2	96 km × 390 km 98-minute orbit (granule duration)	From 2011-08-25 to 2015-06-07 End of mission data	smap_sss	v5	NASA Aquarius project
Aquarius SSS L2 CAP v5 (JPL)	L2	96 km × 390 km 98-minute orbit (granule duration)	From 2011-08-25 to 2015-06-04 End of mission data	sss_cap	v5	JPL
SMOS SSS L3 v317 - 10 days (CATDS-CPDC)	L3	~50 km (grid 25 km × 25 km) 10 days (both ascending and descending orbits)	From 2010-01-01 to 2019-04-31 (RE06) From 2019-05-01 to present (OPER) 10 days	Mean_Sea_Surface_Salinity	v317	CATDS CPDC
SMOS SSS L3 v317 - monthly (CATDS-CPDC)	L3	~50 km (grid 25 km × 25 km) Monthly	From 2010-01-01 to 2019-04-31 (RE06) From 2019-05-01 to present (OPER) 10 days	Mean_Sea_Surface_Salinity	v317	CATDS CPDC
SMOS SSS L3 v3 - 9 days (CATDS-CECOS-LOCEAN)	L3	~50 km (grid 25 km × 25 km) 9 days (every 4 days)	From 2010-01-16 to 2017-12-31 Yearly	SSS	v3	CATDS CECOS LOCEAN
SMOS SSS L3 v3 - 18 days (CATDS-CECOS-LOCEAN)	L3	~50 km (grid 25 km × 25 km) 18 days (every 4 days)	From 2010-01-16 to 2017-12-31 Yearly	SSS	v3	CATDS CECOS LOCEAN
SMOS SSS L3 v2 - daily (CATDS-CECOS-IFREMER)	L3	0.5° Daily	From 2010-05-01 to 2017-12-31 Yearly	SSS	v2	CATDS CECOS IFREMER
SMOS SSS L3 v2 - monthly (CATDS-CECOS-IFREMER)	L3	0.25° Monthly	From 2010-05-01 to 2017-12-31 Yearly	SSS	v2	CATDS CECOS IFREMER
SMOS SSS L3 OA v1 - 9 days (BEC)	L3	0.25° 9 days	From 2010-05-01 to present Daily	oa_sss		BEC
SMAP SSS L3 v4.2 - 8-day running (JPL)	L3	~60 km (grid 0.25°x0.25°) 8-day running	From 2015-03-27 to present 8 days	smap_sss	v4.2	JPL
SMAP SSS L3 v4.2 - monthly (JPL)	L3	~60 km (grid 0.25°x0.25°) Monthly	From 2015-03-27 to present Monthly	smap_sss	v4.2	JPL
SMAP SSS L3 v4 - 8-day running (RSS)	L3	~70 km (grid 0.25°x0.25°) 8-day running	From 2015-03-27 to present Daily	sss_smap	v4	RSS
SMAP SSS L3 v4 - monthly (RSS)	L3	~70 km (grid 0.25°x0.25°) Monthly	From 2015-03-27 to present Monthly	sss_smap	v4	RSS
Aquarius SSS L3 CAP v5 - 7-day running (JPL)	L3	1° 7-day running	From 2011-08-25 (238) to 2015-06-04 (155) End of mission data	sss_cap	v5	JPL
Aquarius SSS L3 CAP v5 - monthly (JPL)	L3	1° Monthly	From 2011-08-25 to 2015-06-04 End of mission data	sss_cap	v5	JPL
Aquarius SSS L3 OR v5 - 7-day running (NASA-GSFC)	L3	1° 7-day running	From 2011-08-25 to 2015-06-07 End of mission data	SSS	v5	NASA Aquarius project
Aquarius SSS L3 OR v5 - monthly (NASA-GSFC)	L3	1° Monthly	From 2011-08-25 to 2015-06-07 End of mission data	SSS	v5	NASA Aquarius project
SMOS SSS L3 v3 - monthly (ICDC)	L3	0.5° Monthly	From 2010-05-01 to 2016-12-31 If new version or update	sss_biasadj	v3	ICDC
SMOS SSS L4 v2 - weekly (CATDS-CECOS-IFREMER)	L4	0.5° Weekly	From 2010-05-01 to 2017-02-31 Yearly	sss | SSS	v2	CATDS CECOS IFREMER
SMOS SSS L4 BEC FUSION	L4	0.05° 9 days	From 2010-05-01 to 2017-01-04 –	l4_sss quality_flag	v2	BEC
Aquarius SSS L4 OI v5 - weekly (IPRC)	L4	0.5° Weekly	From 2011-09-01 to 2015-06-03 End of mission data	sss	v5	IPRC
Aquarius SSS L4 OI v5 - monthly (IPRC)	L4	0.5° Monthly	From 2011-09-01 to 2015-06-03 End of mission data	sss	v5	IPRC
CCI SSS L4 Merged-OI v1.8 - 7-day running (ESA)	L4	0.25° 7-day running	From 2010-01-06 to 2018-11-01 –	sss	v1.8	ESA

CCI SSS L4 Merged-OI v1.8 - 30-day running (ESA)	L4	0.25° 30-day running	From 2010-01-06 to 2018-11-01	sss	v1.8	ESA

Appendix B. List of acronyms

Acronym	Meaning
acdm	absorption coefficient for color detrital matter
AMSR	Advanced Microwave Scanning Radiometer
BL	Barrier-Layer
BLT	Barrier-Layer Thickness
CAP	Combined Active-Passive
CATDS	Centre Aval de Traitement des Données SMOS
CCI-SSS	ESA Climate Change Initiative-Sea Surface Salinity project
CDTI	Spanish Centre for the Development of Industrial Technology
CIMR	Conical Imaging Microwave Radiometer
CMB	Cosmic Microwave Background
CNES	French Centre National d'Etudes Spatiales
Ch-la	Chlorophyll-a
CONAE	Comisión Nacional de Actividades Espaciales
CTD	Conductivity-Temperature-Depth
DIC	Dissolved Inorganic Carbon
EAF-FOV	Extended Alias-Free Field Of View
EASE-grid	Equal-Area Scalable Earth Grid
ECMWF	European Center for Medium-range Weather Forecast
ECV	Essential Climate Variable
ENSO	El Niño Southern Oscillations
EO	Earth Observation
E-P	Evaporation (E) minus Precipitation (P)
EPE	Eddy Potential Energy
ESA	European Space Agency
ESTAR	Electrically Scanning Thinned Array Radiometer
ESTEC	European Space Research and Technology Centre, the Netherlands
EUC	Equatorial UnderCurrent
FOV	Field Of View
GCOS	Global Climate Observing System
GOOS	Global Ocean Observing System
GMF	Geophysical Model Functions
GOSUD	Global Ocean Surface Underway Data
GODAE	Global Ocean Data Assimilation Experiment
GPM	Global Precipitation Mission
HH	Horizontally-polarized emitted Horizontally-polarized received
HYCOM	HYbrid COordinate Model
IOD	Indian Ocean Dipole
ITCZ	Inter-tropical Convergence Zone
ITU	International Telecommunication Union
JPL	Jet Propulsion Laboratory
KS	dielectric constant model for sea water from Klein and Swift (1977)
LSC	Land Sea Contamination
MIRAS	Microwave Imaging Radiometer with Aperture Synthesis
MJO	Madden-Julian Oscillation
MW	dielectric constant model for sea water from Meissner and Wentz (2004)
NASA	National Aeronautics and Space Administration
NBC	North Brazilian Current
NCEP	National Center for Environmental Prediction
NEDT	Noise Equivalent Differential Temperature
NOAA	National Oceanic and Atmospheric Administration
NODC	NOAA National Oceanic Data Center
OS	Ocean Salinity
OTT	Ocean Target Transformation
PALS	Passive-Active L-band System
PI-MEP	SMOS Pilot Mission Exploitation Platform
RMS	Root Mean Square
RMSD	Root Mean Square Difference
RFI	Radio Frequency Interferences
RR	Rain Rate
RSS	Remote Sensing System
RSTN	United States Air Force Radio Solar Telescope Network
SAMOS	Shipboard Automated Meteorological and Oceanographic System
SEPSI	Southeastern Pacific SSS Index
SIO	Scripps Institution of Oceanography
SLFMR	Scanning Low Frequency Microwave Radiometer
SMAP	Soil Moisture Active-Passive mission
SMOS	Soil Moisture and Ocean Salinity
SOI	Southern Oscillation Index
SSM/I	Special Sensor Microwave Imager
SSH	Sea Surface Height
SSS	Sea Surface Salinity

SSSA	SSS Anomalies
SST	Sea Surface Temperature
STD	STandard Deviation
SWH	Significant Wave Height
TA	Total Alkalinity
T_B	Sea surface brightness temperature
TC	Tropical Cyclones
TEC	Total Electron Content
TIW	Tropical Instability Wave
TSG	ThermoSalinoGraphs
VTEC	Vertical ionospheric Total Electron Content
VV	Vertically-polarized emitted Vertically-polarized received
WOCE	World Ocean Circulation Experiment
WOD	World Ocean Database

References

Akhil, V.P., Lengaigne, M., Durand, F., Vialard, J., Chaitanya, A.V.S., Keerthi, M.G., Gopalakrishna, V.V., Boutin, J., Montegut, C.D., 2016. Assessment of seasonal and year-to-year surface salinity signals retrieved from SMOS and Aquarius missions in the Bay of Bengal. Int. J. Remote Sens. 37 (5), 1089–1114.

Alory, G., Maes, C., Delcroix, T., Reul, N., Illig, S., 2012. Seasonal dynamics of sea surface salinity off Panama: the far Eastern Pacific Fresh Pool. J. Geophys. Res. 117, C04028.

Alory, G., Delcroix, T., Téchiné, P., Diverres, D., Varillon, D., Cravatte, S., Gouriou, Y., Grelet, J., Jacquin, S., Kestenare, E., 2015. The French contribution to the voluntary observing ships network of sea surface salinity. Deep-Sea Res. Pt. I 105, 1–18. ISSN 0967-0637. https://doi.org/10.1016/j.dsr.2015.08.005.

Alvera-Azcárate, A., Barth, A., Parard, G., Beckers, J., 2016. Analysis of SMOS sea surface salinity data using DINEOF. Remote Sens. Environ. 180, 137–145.

Anterrieu, E., 2007. On the reduction of the reconstruction bias in synthetic aperture imaging radiometry. IEEE Trans. Geosci. Remote Sens. 45 (3), 592–601.

Argo, 2000. Argo Float Data and Metadata From Global Data Assembly Centre (Argo GDAC). https://doi.org/10.17882/42182.

Balaguru, K., Chang, P., Saravanan, R., Leung, L.R., Xu, Z., Li, M., Hsieh, J.-S., 2012. Ocean barrier layers' effect on tropical cyclone intensification. PNAS 109 (36), 14,343–14,347. https://doi.org/10.1073/pnas.1201364109.

Banks, C.J., Srokosz, M.A., Cipollini, P., Snaith, H.M., Blundell, J.R., Gommenginger, C.P., Tzortzi, E., 2016. Reduced ascending/descending pass bias in SMOS salinity data demonstrated by observing westward-propagating features in the South Indian Ocean. Remote Sens. Environ. 180, 154–163.

Bayle, F., Wigneron, J.P., Kerr, Y.H., Waldteufel, P., Anterrieu, E., Orlhac, J.C., Chanzy, A., Marloie, O., Bernardini, M., Sobjaerg, S., Calvet, J.C., Goutoule, J.M., Skou, N., 2002. Two-dimensional synthetic aperture images over a land surface scene. IEEE Trans. Geosci. Remote Sens. 40 (3), 710–714.

Belonenko, T.V., Bashmachnikov, I.L., Kubryakov, A.A., 2018. Horizontal advection of temperature and salinity by Rossby waves in the North Pacific. Int. J. Remote Sens. 39 (8), 2177–2188. https://doi.org/10.1080/01431161.2017.1420932.

Bingham, F.M., Lee, T., 2017. Space and time scales of sea surface salinity and freshwater forcing variability in the global ocean (60°S–60°N). J. Geophys. Res. Oceans 122, 2909–2922. https://doi.org/10.1002/2016JC012216.

Bingham, F.M., Howden, S.D., Koblinsky, C.J., 2002. Sea surface salinity measurements in the historical database. J. Geophys. Res. 107 (C12), 8019.

Bjerknes, J., 1969. Atmospheric teleconnections from the equatorial Pacific. Mon Wea Rev 97, 163–172.

Blanch, S., Aguasca, A., 2004. Seawater dielectric permittivity model from measurements at L band. In: Proc. IGARSS, pp. 1362–1365.

Blume, H.-J., Kendall, B.M., 1982. Passive microwave measurements of temperature and salinity in coastal zone. IEEE Trans. Geosci. Remote Sens. 20, 394–404.

Blume, H.-J., Fedors, J.C., 1978. Measurement of ocean temperature and salinity via microwave radiometry. Bound.-Layer Meteor. 13, 295–308.

Boutin, J., Waldteufel, P., Martin, N., Caudal, G., Dinnat, E., 2004. Surface salinity retrieved from SMOS measurements over the Global Ocean: imprecisions due to sea surface roughness and temperature uncertainties. J. Atmos. Technol. 21 (9), 1432–1447.

Boutin, J., Martin, N., Reverdin, G., Yin, X., Gaillard, F., 2013. Sea surface freshening inferred from SMOS and Argo salinity: impact of rain. Ocean Sci. 9, 183–192.

Boutin, J., Martin, N., Reverdin, G., Morisset, S., Yin, X., Centurioni, L., Reul, N., 2014. Sea surface salinity under rain cells: SMOS satellite and *in situ* drifters observations. Journal of Geophysical Research, Oceans 119, 5533–5545.

Boutin, J., Chao, Y., Asher, W.E., Delcroix, T., Drucker, R., Drushka, K., Kolodziejczyk, N., Lee, T., Reul, N., Reverdin, G., Schanze, J., Soloviev, A., Yu, L., Anderson, J., Brucker, L., Dinnat, E., Garcia, A.S., Jones, W.L., Maes, C., Meissner, T., Tang, W., Vinogradova, N., Ward, B., 2016. Satellite and *in situ* salinity: understanding near-surface stratification and sub-footprint variability. Bull. Am. Meteorol. Soc. 97 (10). https://doi.org/10.1175/BAMS-D-15-00032.1.

Boutin, J., Vergely, J.L., Marchand, S., D'Amico, F., Hasson, A., Kolodziejczyk, N., Reul, N., Reverdin, G., Vialard, J., 2018. New SMOS sea surface salinity with reduced systematic errors and improved variability. Remote Sens. Environ. 214, 115–134.

Boyer, T.P., Levitus, S., Antonov, J.I., Locarnini, R.A., Garcia, H.E., 2005. Linear trends in salinity for the World Ocean, 1955–1998. Geophys. Res. Lett. 32, L01604. https://doi.org/10.1029/2004GL021791.

Brown, R.A., 1983. On a satellite scatterometer as an anemometer. J. Geophys. Res. 88, 1663–1673.

Brown, C.W., Boutin, J., Merlivat, L., 2015. New insights of pCO2 variability in the tropical eastern Pacific Ocean using SMOS SSS. Biogeosci. Discuss. 12 (6), 4595–4625. https://doi.org/10.5194/bgd-12-4595-2015.

Burrage, D.M., Heron, M.L., Hacker, J.M., Miller, J.L., Stieglitz, T.C., Steinberg, C.R., Prytz, A., 2003. Structure and influence of tropical river plumes in the Great Barrier Reef: application and performance of an airborne sea surface salinity mapping system. Remote Sens. Environ. 85, 204–220.

Camps, A., et al., 2004. The WISE 2000 and 2001 campaigns in support of the SMOS Mission: sea surface L-band brightness temperature observations and their application to multi-angular salinity retrieval. IEEE Trans. Geosci.Remote Sensing 42 (4), 1039–1048.

Camps, A., Vall-llossera, M., Reul, N., Chapron, B., Corbella, I., Duffo, N., Torres, F., 2005. The emissivity of foam-covered water surface at L-band: theoretical modeling and experimental results from the FROG 2003 field experiment. IEEE Trans. Geosci. Remote Sens. 43 (5), 925–937.

Chakraborty, A., Sharma, R., Kumar, R., Basu, S., 2014. A SEEK filter assimilation of sea surface salinity from Aquarius in an OGCM: implication for surface dynamics and thermohaline structure. J. Geophys. Res. Oceans 119.

Chao, Y., Farrara, J.D., Schumann, G., Andreadis, K.M., Moller, D., 2015. Sea surface salinity variability in response to the Congo river discharge Cont. Shelf Res. 99, 35–45. https://doi.org/10.1029/2010JC006937.

Chen, S., Hu, C., 2017. Estimating sea surface salinity in the northern Gulf of Mexico from satellite ocean color measurements. Remote Sens. Environ. 201, 115–132. https://doi.org/10.1016/j.rse.2017.09.004.

Chen, J., You, X., Xiao, Y., Zhang, R., Wang, G., Bao, S., 2017. A performance evaluation of remotely sensed sea surface salinity products in combination with other surface measurements in reconstructing three-dimensional salinity fields. Acta Oceanol. Sin. 36 (7), 15–31. https://doi.org/10.1007/s13131-017-1079-y.

Chen, B., Qin, H., Chen, G., Xue, H., 2019. Ocean salinity as a precursor of summer rainfall over the East Asian monsoon region. J. Clim. 32, 5659–5676. https://doi.org/10.1175/JCLI-D-18-0756.1.

Cheney, R.E., Douglas, B.C., Miller, L., 1989. Evaluation of Geosat altimeter data with application to tropical Pacific sea level variability. J. Geophys. Res. 94 (C4), 4737–4747.

Corbella, I., Duran, I., Wu, L., Torres, F., Nuria, U., Khazaal, A., Martin-neira, M., 2015. Mitigation of land-sea contamination in SMOS. In: IEEE International Geoscience and Remote Sensing Symposium (IGARSS), Milan, pp. 1433–1436.

Cox, C., Munk, W., 1954. Measurement of the roughness of the sea surface from photographs of the sun's glitter. J. Opt. Soc. Am. 44, 838–850. https://doi.org/10.1364/JOSA.44.000838.

Crapolicchio, R., Casella, D., Marque, C., 2018. Solar Radio Observations from Soil Moisture and Ocean Salinity (SMOS) Mission. pp. 4111–4114. https://doi.org/10.1109/IGARSS.2018.8518756.

Curry, R., Dickson, B., Yashayaev, I., 2003. A change in the freshwater balance of the Atlantic Ocean over the past four decades. Nature 426, 826–829. https://doi.org/10.1038/nature02206.

Da Silva, C.E., Castelao, R.M., 2018. Mississippi River plume variability in the Gulf of Mexico from SMAP and MODIS-Aqua observations. Journal of Geophysical Research: Oceans 123, 6620–6638.

Da-Allada, C.Y., Jouanno, J., Gaillard, F., Kolodziejczyk, N., Maes, C., Reul, N., Bourles, B., 2017. Importance of the equatorial undercurrent on the sea surface salinity in the Eastern Equatorial Atlantic in boreal spring. J. Geophys. Res. Oceans 122 (1), 521–538.

D'Addezio, J.M., Subrahmanyam, B., Nyadjro, E.S., Murty, V.S.N., 2015. Seasonal variability of salinity and salt transport in the northern Indian Ocean. J. Phys. Oceanogr. 45 (7), 1947–1966. https://doi.org/10.1175/JPO-D-14-0210.1.

Debye, P., 1929. Polar Molecules. The Chemical Catalog Company Inc, New York, NY, USA.

Delcroix, T., Soviadan, D., Chaigneau, A., Boutin, J., 2017. Quantifying the impact of mesoscale eddies on SSS changes in the tropical Pacific Ocean. In: EGU General Assembly Conference Abstracts. 19. pp. 8624.

Dinnat, E.P., Le Vine, D.M., 2008. Impact of sun glint on salinity remote sensing: an example with the Aquarius radiometer. IEEE Trans. Geosci. Remote Sens. 46 (10), 3137–3150.

Dinnat, E., Boutin, J., Caudal, G., Etcheto, J., Waldteufel, P., 2002. Influence of sea

surface emissivity model parameters in L-band for the estimation of salinity. Int. J. Remote Sens. 23, 5117–5122.
Dinnat, E.P., Boutin, J., Caudal, G., Etcheto, J., 2003. Issues concerning the sea emissivity modeling at L-band for retrieving surface salinity. Radio Sci. 38 (4), 8060.
Dinnat, E.P., Abraham, S., Le Vine, D.M., De Matthaeis, P., Jacob, D., 2009. Effect of emission from the moon on remote sensing of sea surface salinity: an example with the Aquarius radiometer. IEEE Geosci. Remote Sens. Lett. 6 (2), 239–243.
Dinnat, E.P., Boutin, J., Yin, X., Le Vine, D.M., 2014. Inter-comparison of SMOS and Aquarius sea surface salinity, and effects of the dielectric constant and vicarious calibration. In: 13th Specialist Meeting on Microwave Radiometry and Remote Sensing of the Environment (MicroRad), IEEE, Pasadena, Calif.
Donlon, C.J., 2018. The Copernicus Imaging Microwave Radiometer (CIMR) Mission Requirements Document v1.12. December 2018 available from the European Space Agency and http://CIMR.eu = > CIMR.
Droppelman, J.D., Mennella, R.A., Evans, D.E., 1970. An airborne Measuremtn of the salinity variations of the Mississippi River outflow. J. Geophys. Res. 75, 5909–5913.
Drushka, K., Asher, W., Jessup, A., Thompson, E., Iyer, S., Clark, D., 2019. Capturing fresh layers with the surface salinity profiler. Oceanography 32 (2), 76–85. https://doi.org/10.5670/oceanog.2019.215.
Du, Y., Zhang, Y., 2015. Satellite and Argo observed surface salinity variations in the tropical Indian Ocean and their association with the Indian Ocean dipole mode. J. Clim. 28 (2), 695–713. https://doi.org/10.1175/JCLI-D-14-00435.1.
Durack, P.J., Wijffels, S.E., 2010. Fifty-year trends in global ocean salinities and their relationship to broad-scale warming. J. Clim. 23, 4342–4362. https://doi.org/10.1175/2010JCLI3377.1.
Durack, P.J., Wijffels, S.E., Matear, R.J., 2012. Ocean salinities reveal strong global water cycle intensification during 1950 to 2000. Science 336, 455–458.
Durand, F., Alory, G., Dussin, R., Reul, N., 2013. SMOS reveals the signature of Indian Ocean Dipole events. Ocean Dyn. 63 (11–12), 1203–1212.
Dzwonkowski, B., Fournier, S., Reager, J.T., Milroy, S., Park, K., Shiller, A.M., Greer, A.T., Soto, I., Dykstra, S.L., Sanial, V., 2018. Tracking sea surface salinity and dissolved oxygen on a river-influenced, seasonally stratified shelf, Mississippi Bight, northern Gulf of Mexico. Cont. Shelf Res. 169, 25–33.
Ellison, W., et al., 1998. New permittivity measurements of seawater. Radio Sci. 33, 639–648.
Entekhabi, D., et al., 2014. SMAP Handbook. Jet Propulsion Laboratory Publ JPL 400-1567, 182 pp. [Available online at https://smap.jpl.nasa.gov/system/internal_resources/details/original/178_SMAP_Handbook_FINAL_1_JULY_2014_Web.pdf.].
Felton, C.S., Subrahmanyam, B., Murty, V.S.N., Shriver, J.F., 2014. Estimation of the barrier layer thickness in the Indian Ocean using Aquarius salinity. J. Geophys. Res.-Oceans 119 (7), 4200–4213. https://doi.org/10.1002/2013JC009759.
Fine, E.C., Bryan, F.O., Large, W.G., Bailey, D.A., 2015. An initial estimate of the global distribution of diurnal variation in sea surface salinity. J. Geophys. Res. Oceans 120, 3211–3228. https://doi.org/10.1002/2014JC010483.
Fine, R.A., Willey, D.A., Millero, F.J., 2017. Global variability and changes in ocean total alkalinity from Aquarius satellite data. Geophys. Res. Lett. 44, 261–267. https://doi.org/10.1002/2016GL071712.
Font, J., Lagerloef, G.S.E., Le Vine, D.M., Camps, A., Zanife, O.Z., 2004. The determination of surface salinity with the European SMOS space mission. IEEE Trans. Geosci. Remote Sens. 42 (10), 2196–2205. https://doi.org/10.1109/tgrs.2004.834649.
Font, J., Camps, A., Borges, A., Martin-Neira, M., Boutin, J., Reul, N., Kerr, Y.H., Hahne, A., Mecklenburg, S., 2010. SMOS: the challenging sea surface salinity measurement from space. Proc. IEEE 98 (5), 649–665.
Font, J., Boutin, J., Reul, N., Spurgeon, P., Ballabrera-Poy, J., Chuprin, A., Gabarro, C., Gourrion, J., Guimbard, S., Henocq, C., Lavender, S., Martin, N., Martinez, J., McCulloch, M., Meirold-Mautner, I., Mugerin, C., Petitcolin, F., Portabella, M., Sabia, R., Talone, M., Tenerelli, J., Turiel, A., Vergely, J.-L., Waldteufel, P., Yin, X., Zine, S., Delwart, S., 2013. SMOS first data analysis for sea surface salinity determination. Int. J. Remote Sens. 34 (9–10), 3654–3670.
Fore, A.G., Yueh, S.H., Tang, W., Stiles, B.W., Hayashi, A.K., 2016. Combined active/passive retrievals of ocean vector wind and sea surface salinity with SMAP. IEEE Trans. Geosci. Remote Sens. 54 (12), 7396–7404.
Fore, A., Yueh, S., Tang, W., Hayashi, A., 2018. SMAP Salinity and Wind Speed Data User's Guide, Amendment for Version 4.2. Jet Propulsion Laboratory, California Institute of Technology (Dec 31).
Fournier, S., Chapron, B., Salisbury, J., Vandemark, D., Reul, N., 2015. Comparison of spaceborne measurements of sea surface salinity and colored detrital matter in the Amazon plume. J. Geophys. Res. Oceans 120, 3177–3192. https://doi.org/10.1002/2014JC010109.
Fournier, S., Lee, T., Gierach, M., 2016a. Seasonal and interannual variations of sea surface salinity associated with the Mississippi River plume observed by SMOS and Aquarius. In: Remote Science of Environment, Remote Sensing of Environment. 180. pp. 431–439. 2016. ISSN 0034-4257. 10.1016.j.rse.2016.02.050.
Fournier, S., Reager, J.T., Lee, T., Vazquez-Cuervo, J., David, C.H., Gierach, M.M., 2016b. SMAP observes flooding from land to sea: the Texas event of 2015. Geophys. Res. Lett. 43 (19), 10,338–10,346.
Fournier, S., Vialard, J., Lengaigne, M., Lee, T., Gierach, M., 2017a. Modulation of the Ganges-Brahmaputra river plume by the Indian Ocean Dipole and eddies inferred from satellite observations. Journal of Geophysical Research: Oceans 122. https://doi.org/10.1002/2017JC013333.
Fournier, S., Vandemark, D., Gaultier, L., Lee, T., Jonsson, B., Gierach, M., 2017b. Interannual variation in offshore advection of Amazon-Orinoco plume waters: observations, forcing mechanisms, and impacts. Journal of Geophysical Research: Oceans 122. https://doi.org/10.1002/2017JC013103.
Fukumori, I., Heimbach, P., Ponte, R.M., Wunsch, C., 2018. A dynamically consistent, multi-variable ocean climatology. Bull. Amer. Meteor. Soc. https://doi.org/10.1175/BAMS-D-17-0213.1.
Gabarró, C., Font, J., Camps, A., Vall-llossera, M., Julià, A., 2004. A new empirical model of sea surface microwave emissivity for salinity remote sensing. Geophys. Res. Lett. 31, 309.
Gaillard, F., Diverres, D., Gouriou, Y., Jacquin, S., 2015. SSS From French Research Vessels: Inventory of Thermo-salinometer Delayed Mode Data - 2014. https://archimer.ifremer.fr/doc/00251/36231/.
Garcia-Eidell, C., Comiso, J.C., Dinnat, E., Brucker, L., 2017. Satellite observed salinity distributions at high latitudes in the Northern Hemisphere: a comparison of four products. J. Geophys. Res. Ocean. 122 (9), 7717–7736.
Garrison, J.L., Komjathy, A., Zavorotny, V.U., Katzberg, S.J., 2002. Wind speed measurement using forward scattered GPS signals. IEEE Trans. Geosci. Remote Sens. 40 (1), 50–65. https://doi.org/10.1109/36.981349.
Guan, B., Lee, T., Halkides, D.J., Waliser, D.E., 2014. Aquarius surface salinity and the Madden-Julian Oscillation: the role of salinity in surface layer density and potential energy. Geophys. Res. Lett. 41, 2858–2869. https://doi.org/10.1002/2014GL059704.
Gierach, M., Vazquez-Cuervo, J., Lee, T., Tsontos, V.M., 2013. Aquarius and SMOS detect effects of an extreme Mississippi River flooding event in the Gulf of Mexico. Geophys. Res. Lett. 40 (19), 5188–5193. https://doi.org/10.1002/grl.50995.
Gloersen, P., et al., 1984. A summary of results from the first NIMBUS 7 SMMR observations. J. Geophys. Res. 89 (D4), 5335–5344. https://doi.org/10.1029/JD089iD04p05335.
Gonrález-Gambau, V., et al., 2018. Benefits of applying nodal sampling to SMOS data over semi-enclosed seas and strongly RFI-contaminated regions. In: IGARSS 2018–2018 IEEE International Geoscience and Remote Sensing Symposium, Valencia, pp. 305–308.
Goodberlet, M.A., Swift, C.T., 1993. A remote sensing system for measuring estuarine and coastal ocean surface salinity. In: Progress Report #2 Prepared for NOAA Under Contract 50-DKNA-1-00119 to US Dept. of Commerce, 111 (Quadrant Engineering, Hadley, MA).
Goodberlet, M.A., Swift, C.T., Kiley, K.P., Miller, J.L., Zaitzeff, J.B., 1997. Microwave remote sensing of coastal zone salinity. J. Coast. Res. 13 (2), 363–372 (Fort Lauderdale (Florida), ISSN 0749- 0208).
Goutoule, J.M., Anterrieu, E., Kerr, Y.H., Lannes, A., Skou, N., 1996. MIRAS Microwave Radiometry Critical Technical Development. MMS, Toulouse, France (Executive Summary).
Grodsky, S.A., Carton, J.A., 2001. Intense surface currents in the tropical Pacific during 1996-1998. Journal of Geophysical Research: Oceans. https://doi.org/10.1029/2000jc000481.
Grodsky, S.A., Carton, J.A., 2018. Delayed and quasi-synchronous response of tropical Atlantic surface salinity to rainfall. J. Geophys. Res. Oceans 123, 5971–5985. https://doi.org/10.1029/2018JC013915.
Grodsky, S.A., Carton, J.A., Murtugudde, R., 2001. Anomalous surface currents in the tropical Indian Ocean. Geophys. Res. Lett. 28, 4207–4210. https://doi.org/10.1029/2001GL013592.
Grodsky, S.A., Carton, J.A., Provost, C., Servain, J., Lorenzzetti, J.A., McPhaden, M.J., 2005. Tropical instability waves at 0°N, 23°W in the Atlantic: a case study using Pilot Research Moored Array in the Tropical Atlantic (PIRATA) mooring data. J. Geophys. Res. 110, C08010. https://doi.org/10.1029/2005JC002941.
Grodsky, S.A., Carton, J.A., Bingham, F.M., 2006. Low frequency variation of sea surface salinity in the tropical Atlantic. Geophys. Res. Lett. 33, L14604. https://doi.org/10.1029/2006GL026426.
Grodsky, S., Reul, N., Lagerloef, G., Reverdin, G., Carton, J., Chapron, B., Quilfen, Y., Kudryavtsev, V., Kao, H., 2012. Haline hurricane wake in the Amazon/Orinoco plume: AQUARIUS/SAC-D and SMOS observations. Geophys. Res. Lett. 39 (20), L20603. https://doi.org/10.1029/2012GL053335.
Grodsky, S.A., Reverdin, G., Carton, J.A., Coles, V.J., 2014a. Year-to-year salinity changes in the Amazon plume: contrasting 2011 and 2012 Aquarius/SAC-D and SMOS satellite data. Remote Sens. Environ. 140, 14–22. https://doi.org/10.1016/j.rse.2013.08.033.
Grodsky, S.A., Carton, J.A., Bryan, F.O., 2014b. A curious local surface salinity maximum in the northwestern tropical Atlantic. J. Geophys. Res.-Oceans 119 (1), 484–495. https://doi.org/10.1002/2013JC009450.
Grodsky, S.A., Johnson, B.K., Carton, J.A., Bryan, F.O., 2015. Interannual Caribbean salinity in satellite data and model simulations. J. Geophys. Res.-Oceans 120 (2), 1375–1387. https://doi.org/10.1002/2014JC010625.
Grodsky, S.A., Reul, N., Chapron, B., Carton, J.A., Bryan, F.O., 2017. Interannual surface salinity in Northwest Atlantic shelf. J. Geophys. Res. Oceans 122 (5), 3638–3659.
Grodsky, S.A., Vandemark, D., Feng, H., 2018a. Assessing coastal SMAP surface salinity accuracy and its application to monitoring Gulf of Maine circulation dynamics. Remote Sens. 10, 1232.
Grodsky, S.A., Vandemark, D., Feng, H., Levin, J., 2018b. Satellite detection of an unusual intrusion of salty slope water into a marginal sea: using SMAP to monitor Gulf of Maine inflows. Remote Sens. Environ. 217, 550–561. https://doi.org/10.1016/J.RSE.2018.09.004.
Grodsky, S.A., Reul, N., Bentamy, A., Vandemark, D., Guimbard, S., 2019. Eastern Mediterranean salinification observed in satellite salinity from SMAP mission. J. Mar. Syst. 198, 103190. https://doi.org/10.1016/j.jmarsys.2019.103190.
Grunseich, G., Subrahmanyam, B., Murty, V.S.N., Giese, B.S., 2011. Sea surface salinity variability during the Indian Ocean Dipole and ENSO events in the tropical Indian Ocean. J. Geophys. Res.-Oceans 116 (11), C11013. https://doi.org/10.1029/2011JC007456.
Guerrero, R.A., Piola, A.R., Fenco, H., Matano, R.P., Combes, V., Chao, Y., James, C., Palma, E.D., Saraceno, M., Ted Strub, P., 2014. The salinity signature of the cross-

shelf exchanges in the Southwestern Atlantic Ocean: satellite observations. J. Geophys. Res. Oceans 119, 7794–7810. https://doi.org/10.1002/2014JC010113.
Guidice, D.A., Cliver, E.W., Barron, W.R., et al., 1981. The air force RSTN system. Bull. Am. Astronom. Soc. 553.
Guimbard, S., Gourrion, J., Portabella, M., Turiel, A., Gabarro, C., Font, J., 2012. SMOS semi-empirical ocean forward model adjustment. IEEE Trans. Geosci. Remote Sens. 50 (5), 1676–1687.
Guimbard, S., Reul, N., Chapron, B., Umbert, M., Maes, C., 2017. Seasonal and inter-annual variability of the Eastern Tropical Pacific Fresh Pool. J. Geophys. Res. Oceans 122, 1749–1771.
Hackert, E., Busalacchi, A.J., Ballabrera-Poy, J., 2014. Impact of Aquarius sea surface salinity observations on coupled forecasts for the tropical Indo-Pacific Ocean. Journal of Geophysical Research: Oceans 119 (7), 4045–4067.
Hasson, A., Delcroix, T., Boutin, J., Dussin, R., Ballabrera-Poy, J., 2014. Analyzing the 2010–2011 La Niña signature in the tropical Pacific sea surface salinity using in situ data, SMOS observations, and a numerical simulation. J. Geophys. Res. Oceans 119, 3855–3867. https://doi.org/10.1002/2013JC009388.
Hasson, A., Puy, M., Boutin, J., Guilyardi, E., Morrow, R., 2018. Northward propagation across the tropical North Pacific Ocean 25 revealed by surface salinity: how El Nino anomalies reach Hawaii? J. Geophys. Res. 123.
Helm, K.P., Bindoff, N.L., Church, J.A., 2010. Changes in the global hydrological-cycle inferred from ocean salinity. Geophys. Res. Lett. 37, L18701. https://doi.org/10.1029/2010GL044222.
Ho, W.W., Hall, W.F., 1973. Measurements of the dielectric properties of seawater and NaCl solutions at 2.65 GHz. J. Geophys. Res. 78, 6301–6315.
Ho, W.W., Love, A.W., Melle, Van, 1974. Measurements of the Dielectric Properties of Sea Water at 1.43 GHz, NASA Contractor Report CR-2458.
Hollinger, J.P., 1971. Passive microwave measurements of sea surface roughness. IEEE Trans. Geoscience Elect. GE-9, 165–169.
Hopkins, J., Lucas, M., Dufau, C., Sutton, M., Stum, J., Lauret, O., Channelliere, C., 2013. Detection and variability of the Congo River plume from satellite derived sea surface temperature, salinity, ocean colour and sea level. Remote Sens. Environ. 139, 365–385.
Hosoda, S., Suga, T., Shikama, N., Mizuno, K., 2009. Global surface layer salinity change detected by Argo and its implication for hydrological cycle intensification. J. Oceanogr. 65, 579–586.
Hovis, W.A., Clark, D.K., Anderson, F., Austin, R.W., Wilson, W.H., Baker, E.T., Ball, D., Gordon, H.R., Mueller, J.L., El Sayed, S.Y., Sturm, B., Wrigley, R.C., Yentsch, C.S., 1980. Nimbus-7 Coastal Zone Color Scanner:system description and initial imagery. Science 210, 60–63.
Isern-Fontanet, J., Olmedo, E., Turiel, A., Ballabrera-Poy, J., García-Ladona, E., 2016. Retrieval of eddy dynamics from SMOS sea surface salinity measurements in the Algerian Basin (Mediterranean Sea). Geophys. Res. Lett. 43, 6427–6434.
Johnson, J.T., Zhang, M., 1999. Theoretical study of the small slope approximation for the ocean polarimetric thermal emission. IEEE Trans. Geosci. Remote Sens. 37 (5), 2305–2316.
Kao, H.-Y., Lagerloef, G.S.E., 2015. Salinity fronts in the tropical Pacific Ocean. J. Geophys. Res. Oceans 120.
Kao, H.-Y., Lagerloef, G.S.E., Lee, T., Melnichenko, O., Meissner, T., Hacker, P., 2018. Assessment of Aquarius sea surface salinity. Remote Sens. 10, 1341. https://doi.org/10.3390/rs10091341.
Kendall, B.M., Blanton, J.O., 1981. Microwave radiometer measurement of tidally induced salinity changes off the Georgia coast. J. Geophys. Res. 86, 6435–6441.
Kerr, Y.H., et al., 2010. The SMOS mission: new tool for monitoring key elements of the global water cycle. Proc. IEEE 98 (5), 666–687.
Kerr, Y.H., Entekhabi, D., Bindlish, R., Lee, T., Yueh, S., Lagerloef, G., Wigneron, J.-P., Rodriguez-Fernandez, N., Boutin, J., Reul, N., Kaleschke, L., 2018. Present and Future of L-Band Radiometry, IGARSS 2018–2018 IEEE International Geoscience and Remote Sensing Symposium, Valencia. 2018. pp. 1994–1997.
Khazaal, A., Carfantan, H., Anterrieu, E., 2009. On the reduction of the systematic error in imaging radiometry by aperture synthesis: a new approach for the SMOS space mission. IEEE Trans. Geosci. Remote Sens. 6 (1), 47–51.
Khazaal, A., Tenerelli, J., Cabot, F., 2016. Impact of sun glint on the SMOS retrieved brightness temperature maps for almost four years of data. Remote Sens. Environ. 180. https://doi.org/10.1016/j.rse.2016.02.003.
Khazaal, A., Richaume, P., Cabot, F., Anterrieu, E., Mialon, A., Kerr, Y., 2018. Improving the spatial bias correction algorithm in SMOS image reconstruction processor: validation of soil moisture retrievals with *in situ* data. IEEE Trans. Geosci. Remote Sens. 1–14. https://doi.org/10.1109/TGRS.2018.2853619.
Klein, L.A., Swift, C.T., 1977. An improved model for the dielectric constant of sea water at microwave frequencies. IEEE Trans. Antennas Propag. 25, 104–111.
Klemas, V., 2011. Remote sensing of sea surface salinity: an overview with case studies. J. Coast. Res. 27 (5), 830–838.
Knauss, J.A., 1966. Further measurements and observations of the Cromwell current. J. Mar. Res. 24, 206–239.
Köhl, A., Sena Martins, M., Stammer, D., 2014. Impact of assimilating surface salinity from SMOS on ocean circulation estimates. J. Geophys. Res. Oceans 119, 5449–5464.
Köhler, J., Serra, N., Bryan, F.O., Johnson, B.K., Stammer, D., 2018. Mechanisms of mixed-layer salinity seasonal variability in the Indian Ocean. Journal of Geophysical Research: Oceans 123, 466–496.
Kolodziejczyk, N., Hernandez, O., Boutin, J., Reverdin, G., 2015. SMOS salinity in the subtropical North Atlantic salinity maximum: 2. Two-dimensional horizontal thermohaline variability. J. Geophys. Res. Oceans 120, 972–987.
Kolodziejczyk, N., Boutin, J., Vergely, J.L., Marchand, S., Martin, N., Reverdin, G., 2016. Mitigation of systematic errors in SMOS sea surface salinity. Remote Sens. Environ. 180, 164–177.
Korosov, A., Counillon, F., Johannessen, J.A., 2015. Monitoring the spreading of the Amazon freshwater plume by MODIS, SMOS, Aquarius, and TOPAZ. J. Geophys. Res.-Oceans 120 (1), 268–283. https://doi.org/10.1002/2014JC010155.
Kubryakov, A., Stanichny, S., Zatsepin, A., 2016. River plume dynamics in the Kara Sea from altimetry-based lagrangian model, satellite salinity and chlorophyll data. Remote Sens. Environ. 176, 177–187. https://doi.org/10.1016/j.rse.2016.01.020.
Lagerloef, G., Swift, C., Le Vine, D., 1995. Sea surface salinity: the next remote sensing challenge. Oceanography 8 (2), 44–50.
Lagerloef, G., Colomb, F.R., Le Vine, D., Wentz, F., Yueh, S., Ruf, C., Lilly, J., Gunn, J., Chao, Y., deCharon, A., Swift, C., 2008. The Aquarius/SAC-D mission – designed to meet the salinity remote sensing challenge. Oceanography Magazine 21 (1), 68–81.
Land, P., Shutler, J., Findlay, H., Girard Ardhuin, F., Sabia, R., Reul, N., Piolle, J.-F., Chapron, B., Quilfen, Y., Salisbury, J., Vandemark, D., Bellerby, R., Bhadury, P., 2015. Salinity from space unlocks satellite-based assessment of ocean acidification. Environmental Science & Technology 49 (4), 1987–1994.
Land, P.E., Findlay, H.S., Shutler, J.D., Ashton, I., Holding, T., Grouazel, A., Ardhuin, F., Reul, N., Piolle, J.-F., Chapron, B., Quilfen, Y., Bellerby, R.G.J., Bhadury, P., Salisbury, J., Vandemark, D., Sabia, R., 2019. Optimum satellite remote sensing of the marine carbonate system using empirical algorithms in the global ocean, the Greater Caribbean, the Amazon Plume and the Bay of Bengal. Remote Sens. Environ. 235, 111469. https://doi.org/10.1016/j.rse.2019.111469. (15p.).
Lang, R., Zhou, Y., Utku, C., Le Vine, D., 2016. Accurate measurements of the dielectric constant of seawater at L band. Radio Sci. 51, 2–24.
Large, W.G., Caron, J.M., 2015. Diurnal cycling of sea surface temperature, salinity, and current in the CESM coupled climate model. J. Geophys. Res. Oceans 120, 3711–3729. https://doi.org/10.1002/2014JC010691.
Le Vine, D.M., Abraham, S., 2002. The effect of the ionosphere on remote sensing of sea surface salinity from space: absorption and emission at L band. IEEE Trans. Geosci. Remote Sens. 40, 771–782.
Le Vine, D.M., Abraham, S., 2004. Galactic noise and passive microwave remote sensing from space at L-band. IEEE Trans. Geosci. Remote Sens. 42 (1), 119–129.
Le Vine, D.M., Kao, M., Tanner, A.B., Swift, C.T., Griffis, A., 1990. Initial results in the development of a synthetic aperture microwave radiometer. IEEE Trans. Geosci. Remote Sens. 28, 614–619.
Le Vine, D.M., Kao, M., Garvine, R., Sanders, T., 1998. Remote sensing of ocean salinity: results from the Delaware coastal current experiment. J. Atmos. Ocean. Technol. 15, 1478–1484.
Le Vine, D.M., Abraham, S., Wentz, F., Lagerloef, G.S.E., 2005. Impact of the sun on remote sensing of sea surface salinity from space. In: Proc. Internat. Geosci. & Remote Sens. Sympos, IGARSS05. 1https://doi.org/10.1109/IGARSS.2005.1526164. (Seoul, S. Korea).
Le Vine, D.M., Lagerloef, G.S.E., Colomb, F.R., Yueh, S.H., Pellerano, F.A., 2007. Aquarius: an instrument to monitor sea surface salinity from space. IEEE Trans. Geosci. Remote Sens. 45 (7), 2040–2050. https://doi.org/10.1109/TGRS.2007.898092.
Lee, K., Tong, L.T., Millero, F.J., Sabine, C.L., Dickson, A.G., Goyet, C., Park, G.-H., Wanninkhof, R., Feely, R.A., Key, R.M., 2006. Global relationships of total alkalinity with salinity and temperature in surface waters of the world's oceans. Geophys. Res. Lett. 33, L19605. https://doi.org/10.1029/2006GL027207.
Lee, T., Lagerloef, G., Gierach, M.M., Kao, H.-Y., Yueh, S., Dohan, K., 2012. Aquarius reveals salinity structure of tropical instability waves. Geophys. Res. Lett. 39, L12610.
Lee, T., Lagerloef, G., Kao, H.-Y., McPhaden, M.J., Willis, J., Gierach, M.M., 2014. The influence of salinity on tropical Atlantic instability waves. J. Geophys. Res. Oceans 119, 8375–8394. https://doi.org/10.1002/2014JC010100.
Lee, T., Yueh, S., Lagerloef, G., Steele, M., Thompson, A., Flexas, M., et al., 2016. Linkages of salinity with ocean circulation, water cycle, and climate variability. In: Community White Paper in Response to Request for Information #2 by the US National Research Council Decadal Survey for Earth Science and Applications from Space 2017–2027, http://surveygizmoresponseuploads.s3.amazonaws.com/fileuploads/15647/2604456/107-1abc9aa1a37ab7e77d91d86598954a50_LeeTong.pdf (accessed May 14, 2019).
Lefèvre, N., Diverrès, D., Gallois, F., 2010. Origin of CO2 undersaturation in the western tropical Atlantic. Tellus B 62, 595–607. https://doi.org/10.1111/j.1600-0889.2010.00475.x.
Lerner, R.M., Hollinger, J.P., 1977. Analysis of 1.4 GHz radiometric measurements from Skylab. Remote Sens. Environ. 6, 251–269.
Li, L., Schmitt, R.W., Ummenhofer, C.C., Karnauskas, K.B., 2016a. Implications of North Atlantic Sea surface salinity for summer precipitation over the U.S. Midwest: mechanisms and predictive value. J. Clim. 29, 3143–3159. https://doi.org/10.1175/JCLI-D-15-0520.1.
Li, L., Schmitt, R.W., Ummenhofer, C.C., Karnauskas, K.B., 2016b. North Atlantic salinity as a predictor of Sahel rainfall. Sci. Adv. 2, e1501588. https://doi.org/10.1126/sciadv.1501588.
Liang, X., Yu, L., 2016. Variations of the global net air–sea heat flux during the "Hiatus" period (2001 − 10). J. Clim. 29, 3647–3660. https://doi.org/10.1175/JCLI-D-15-0626.1.
Liebe, H.J., Rosenkranz, P.W., Hufford, G.A., 1992. Atmospheric 60-GHz oxygen spectrum: new laboratory measurements and line parameters. J. Quantitiative Spectroscopy and Radiative Transfer 48, 629–643.
Lindstrom, E., Bryan, F., Schmitt, R., 2015. SPURS: salinity processes in the upper-ocean regional study—the North Atlantic experiment. Oceanography 28 (1), 14–19. https://doi.org/10.5670/oceanog.2015.01.
Lindstrom, E.J., Edson, J.B., Schanze, J.J., Shcherbina, A.Y., 2019. SPURS-2: salinity processes in the upper-ocean regional study 2. The eastern equatorial Pacific experiment. Oceanography 32 (2), 15–19. https://doi.org/10.5670/oceanog.2019.207.
Liu, H., Grodsky, S.A., Carton, J.A., 2009. Observed subseasonal variability of oceanic

barrier and compensated layers. J. Clim. 22 (22), 6104–6119. https://doi.org/10.1175/2009JCLI2974.1.
Lu, Z., Cheng, L., Zhu, C.J., Lin, R., 2016. The complementary role of SMOS sea surface salinity observations for estimating global ocean salinity state. J. Geophys. Res. Oceans 121. https://doi.org/10.1002/2015JC011480.
Lukas, R., Lindstrom, E., 1991. The mixed layer of the western equatorial Pacific Ocean. J. Geophys. Res. 96, 3343–3357.
Maes, C., Picaut, J., Belamari, S., 2002. Salinity barrier layer and onset of El Niño in a Pacific coupled model. Geophys. Res. Lett. 29, 2206. https://doi.org/10.1029/2002GL016029.
Maes, C., Picaut, J., Belamari, S., 2005. Importance of the salinity barrier layer for the buildup of El Niño. J. Clim. 18, 104–118. https://doi.org/10.1175/JCLI-3214.1.
Maes, C., Reul, N., Behringer, D., O'Kane, T., 2014. The salinity signature of the equatorial Pacific cold tongue as revealed by the satellite SMOS mission. Geoscience Letters 1 (1), 1–7.
Martin, J.M., 2016. Suitability of satellite sea surface salinity data for use in assessing and correcting ocean forecasts. Remote Sens. Environ. 180, 305–319.
Martin, J.M., King, R.R., While, J., Aguiar, A., 2018. Assimilating satellite sea surface salinity data from SMOS, Aquarius and SMAP into a global ocean forecasting system. Q. J. R. Meteorol. Soc. https://doi.org/10.1002/qj.3461. (Accepted Author Manuscript).
Martin-Neira, M., Suess, M., Kainulainen, J., Martin-Porqueras, F., 2008. The flat target transformation. IEEE Trans. Geosci. Remote Sens. 46 (3), 613–620 (2008).
Matsuoka, A., Babin, M., Devred, E., 2016. A new algorithm for discriminating water sources from space: a case study for the southern Beaufort Sea using MODIS ocean color and SMOS salinity data. Remote Sens. Environ. 184, 124–138.
Matsuoka, A., Boss, E., Babin, M., Karp-Boss, L., Hafez, M., Chekalyuk, A., Proctor, C.W., Werdell, P., Bricaud, A., 2017. Pan-Arctic optical characteristics of colored dissolved organic matter: tracing dissolved organic carbon in changing Arctic waters using satellite ocean color data. Remote Sens. Environ. 200, 89–101.
McPhaden, M.J., Busalacchi, A.J., Anderson, D.L.T., 2010. A TOGA retrospective. Oceanography 23 (3), 86–103. https://doi.org/10.5670/oceanog.2010.26.
Mecklenburg, S., Drusch, M., Kerr, Y., Font, J., Martin-Neira, M., Delwart, S., Buenadicha, G., Reul, N., Daganzo-Eusebio, E., Oliva, R., Crapolicchio, R., 2012. ESA's soil moisture and ocean salinity mission: mission performance and operations. IEEE Trans. Geosci. Remote Sens. 50 (5), 1354–1366.
Meissner, T., Wentz, F., 2004. The complex dielectric constant of pure and sea water from microwave satellite observations. IEEE Trans. Geosci. Remote Sens. 42 (9), 1836–1849.
Meissner, T., Wentz, F., 2012. The emissivity of the ocean surface between 6 and 90 GHz over a large range of wind speeds and earth incidence angles. IEEE Trans. Geosci. Remote Sensing 50 (8), 3004–3026.
Meissner, T., Wentz, F., Ricciardulli, L., 2014. The emission and scattering of L-band microwave radiation from rough ocean surfaces and wind speed measurements from Aquarius. J. Geophys. Res. Oceans 119.
Meissner, T., Wentz, F.J., Le Vine, D.M., 2018. The salinity retrieval algorithms for the NASA Aquarius version 5 and SMAP version 3 releases. Remote Sens. 10, 1121.
Melnichenko, O.V., Amores, A., Maximenko, N.A., Hacker, P., Potemra, J.T., 2017. Signature of mesoscale eddies in satellite sea surface salinity data. J. Geophys. Res.-Oceans 122 (2), 1416–1424. https://doi.org/10.1002/2016JC012420. IPRC-1236.
Menezes, V.V., Vianna, M.L., Phillips, H.E., 2014. Aquarius sea surface salinity in the South Indian Ocean: revealing annual-period planetary waves. J. Geophys. Res. Oceans 119, 3883–3908.
Merchant, C.J., Embury, O., Bulgin, C.E., et al., 2019. Satellite-based time-series of sea-surface temperature since 1981 for climate applications. Sci Data 6, 223. https://doi.org/10.1038/s41597-019-0236-x.
Miller, J.L., Goodberlet, M., 2004. Development and applications of STARRS: a next generation airborne salinity imager. Int. J. Remote Sens. 25, 1319–1324.
Miller, J., Goodberlet, M.A., Zaitzeff, J.B., 1998. Airborne salinity mapper makes debut in coastal zone. EOS Trans. AGU 79, 173–177.
Misra, S., Ruf, C., 2008. Detection of radio-frequency interference for the Aquarius radiometer. IEEE Trans. Geosci. Remote Sens. 46, 3123–3128.
Mohammed, P.N., Aksoy, M., Piepmeier, J.R., Johnson, J.T., Bringer, A., 2016. SMAP L-band microwave radiometer: RFI mitigation prelaunch analysis and first year on-orbit observations. IEEE Trans. Geosci. Remote Sens. 54 (10), 6035–6047.
Moon, J.-H., Song, Y.T., 2014. Seasonal salinity stratifications in the near-surface layer from Aquarius, Argo, and an ocean model: focusing on the tropical Atlantic/Indian Oceans. J. Geophys. Res. Oceans 119, 6066–6077.
Morisset, S., Reverdin, G., Boutin, J., Martin, N., Yin, X., Gaillard, F., Blouch, P., Rolland, J., Font, J., Salvador, J., 2012. Surface salinity drifters for SMOS validation. In: Mercator Ocean – CORIOLIS Quarterly Newsletter. 45. pp. 33–37 Open Access version: https://archimer.ifremer.fr/doc/00114/22552/.
Nyadjro, E.S., Subrahmanyam, B., 2014. SMOS mission reveals the salinity structure of the Indian ocean dipole. IEEE Geosci. Remote Sens. Lett. 11 (9), 1564–1568. https://doi.org/10.1109/LGRS.2014.2301594.
Nyadjro, E.S.N., Subrahmanyam, B., 2016. Spatial and temporal variability of central Indian Ocean salinity fronts observed by SMOS. Remote Sens. Environ. 180, 146–153.
O'Kane, T.J., Monselesan, D.P., Maes, C., 2016. On the stability and spatiotemporal variance distribution of salinity in the upper ocean. J. Geophys. Res. Oceans 121, 4128–4148. https://doi.org/10.1002/2015JC011523.
Oliva, R., Daganzo, E., Richaume, P., Kerr, Y., Cabot, F., Soldo, Y., Anterrieu, E., Reul, N., Gutierrez, A., Barbosa, J., Lopes, G., 2016. Status of Radio Frequency Interference (RFI) in the 1400–1427 MHz passive band based on six years of SMOS mission. Remote Sens. Environ. 180, 64–75.
Olmedo, E., Martínez, J., Umbert, M., Hoareau, N., Portabella, M., Ballabrera-Poy, J., Turiel, A., 2016. Improving time and space resolution of SMOS salinity maps using multifractal fusion. Remote Sens. Environ. 180, 246–263.
Olmedo, E., Martínez, J., Turiel, A., Ballabrera-Poy, J., Portabella, M., 2017. Debiased non-Bayesian retrieval: a novel approach to SMOS sea surface salinity. Remote Sens. Environ. 193, 103–126.
Olmedo, E., Taupier-Letage, I., Turiel, A., Alvera-Azcárate, A., 2018a. Improving SMOS sea surface salinity in the Western Mediterranean sea through multivariate and multifractal analysis. Remote Sens. 10, 485.
Olmedo, E., Gabarró, C., González-Gambau, V., Martínez, J., Ballabrera-Poy, J., Turiel, A., Portabella, M., Fournier, S., Tong, L., 2018b. Seven years of SMOS sea surface salinity at high latitudes: variability in Arctic and sub-Arctic regions. Remote Sens. 10 (11), 1772.
Pant, V., Girishkumar, M.S., Bhaskar, T.V.S.U., Ravichandran, M., Papa, F., Thangaprakash, V.P., 2015. Observed interannual variability of near-surface salinity in the Bay of Bengal. J.Geophys.Res.-Oceans 120 (5), 3315–3329. https://doi.org/10.1002/2014JC010340.
Paris, J.F., 1969. Microwave radiometry and its applications to marine meteorology and oceanography. In: Texas A&M Project 286-13 (Ref. No. 69–1T), pp. 120–129.
Peake, W.H., 1959. Interaction of electromagnetic waves with some natural surfaces. IRE Trans. Antennas and Propagation AP-7, S324–S329.
Perez, T., Wesson, J., Burrage, D., 2006. Airborne remote sensing of the Plata plume using STARRS. Sea Technology 31–34.
Piepmeier, J., Mohammed, P., Peng, J., Kim, E., De Amici, G., Ruf, C., 2016. SMAP L1B Radiometer Half-orbit Time-ordered Brightness Temperatures. Version 3; CRID 13080. NSIDC, Boulder, CO, USA.
Pi-MEP, 2019. Match-up Database Analyses Report, SMOS-L3-CATDS-CECOS-LOCEAN-V3- 18DAYS-25KM, Argo, Global Ocean. Available at. https://pimep.ifremer.fr/diffusion/analyses/mdb-database/GO/smos-l3-catds-locean-v3-18d/argo/report/pimep-mdb-report_GO_smos-l3-catds-locean-v3-18d_argo_20190315.pdf.
Qu, T.D., Yu, J.Y., 2014. ENSO indices from sea surface salinity observed by Aquarius and Argo. J. Oceanogr. 70 (4), 367–375.
Qu, T., Song, Y.T., Maes, C., 2014. Sea surface salinity and barrier layer variability in the equatorial Pacific as seen from Aquarius and Argo. J. Geophys. Res. Oceans 119, 15–29.
Rajabi, S., Hasanlou, M., Safari, A.R., 2017. Spatial and temporal analysis of sea surface salinity using satellite imagery in Gulf of Mexico. Int. Arch. Photogramm. Remote Sens. Spatial Inf. Sci. XLII-4/W4, 219–223. https://doi.org/10.5194/isprs-archives-XLII-4-W4-219-2017.
Reul, N., et al., 2005. On the use of rigorous microwave interaction models to support remote sensing of natural surfaces. In: IGARSS 2005, Proc. 3, pp. 2195–2198.
Reul, N., Tenerelli, J., Chapron, B., Waldteufel, P., 2007. Modeling sun glitter at L-band for sea surface salinity remote sensing with SMOS. IEEE Trans. Geoscience and Remote Sensing 45 (7).
Reul, N., Tenerelli, J., Floury, N., Chapron, B., 2008a. Earth-viewing L-band radiometer sensing of sea surface scattered celestial sky radiation. Part II: application to SMOS. IEEE Trans. Geosci. Remote Sens. 46 (3), 675–688.
Reul, N., Tenerelli, J., Chapron, B., Guimbard, S., Picard, S.-S., Le Traon, P.-Y., Zine, S., 2008b. Preparing the potential and challenge of remote sensing-based sea surface salinity estimation: The CoSMOS airborne campaign, in Proceedings of the SPIE 7150, edited by R. J. Frouin et al. p. 715006, doi:https://doi.org/10.1117/12.804940.
Reul, N., Fournier, S., Boutin, J., Hernandez, O., Maes, C., Chapron, B., Alory, G., Quilfen, Y., Tenerelli, J., Morisset, S., Kerr, Y., Mecklenburg, S., Delwart, S., 2014a. Sea surface salinity observations from space with the SMOS satellite: a new means to monitor the marine branch of the water cycle. Surv. Geophys. 35 (3), 681–722. https://doi.org/10.1007/s10712-013-9244-0.
Reul, N., Chapron, B., Lee, T., Donlon, C., Boutin, J., Alory, G., 2014b. Sea surface salinity structure of the meandering gulf stream revealed by SMOS sensor. Geophys. Res. Lett. 41, 3141–3148.
Reul, N., Quilfen, Y., Chapron, B., Fournier, S., Kudryavtsev, V., Sabia, R., 2014c. Multisensor observations of the Amazon-Orinoco River plume interactions with hurricanes. J. Geophys. Res. -Oceans 119 (12), 8271–8295. https://doi.org/10.1002/2014JC010107.
Reynaud, T., Kolodziejczyk, N., Maes, C., Gaillard, F., Reverdin, G., Desprez De Gesincourt, F., Le Goff, H., 2015. Sea Surface Salinity from Sailing Ships: Delayed Mode Dataset, Annual Release. SEANOEhttps://doi.org/10.17882/39476.
Riser, S., Freeland, H., Roemmich, D., et al., 2016. Fifteen years of ocean observations with the global Argo array. Nat. Clim. Chang. 6, 145–153. https://doi.org/10.1038/nclimate2872.
Robinson, I.S., 1994. Satellite Oceanography. John Wiley & Sons Ltd, Chichester, U.K (451p).
Roemmich, D., Gilson, J., 2009. The 2004–2008 mean and annual cycle of temperature, salinity, and steric height in the global ocean from the Argo Program. Prog. Oceanogr. 82 (2), 81–100. ISSN 0079-6611. https://doi.org/10.1016/j.pocean.2009.03.004.
Rosenkranz, P.W., 1998. Water vapor microwave continuum absorption: a comparison of measurements and models. Radio Sci. 33 (4), 919–928.
Rosenkranz de Lasson, J., Cappellin, C., Jorgensen, R., Datashvili, L., Angevain, J., 2017. Advanced techniques for grating lobe reduction for large deployable mesh reflector antennas. In: 2017 IEEE International Symposium on Antennas and Propagation & USNC/URSI National Radio Science Meeting, San Diego, CA, pp. 993–994. https://doi.org/10.1109/APUSNCURSINRSM.2017.8072539.
Rudzin, J.E., Shay, L.K., Jaimes, B., Brewster, J.K., 2017. Upper ocean observations in eastern Caribbean Sea reveal barrier layer within a warm core eddy. Journal of Geophysical Research: Oceans. https://doi.org/10.1002/2016JC012339.
Rudzin, J.E., Shay, L.K., Johns, W.E., 2018. The influence of the barrier layer on SST response during tropical cyclone wind forcing using idealized experiments. J. Phys.

Oceanogr. 48, 1471–1478. https://doi.org/10.1175/JPO-D-17-0279.1.
Sabia, R., Fernández-Prieto, D., Shutler, J., Donlon, C., Land, P., Reul, N., 2015. Remote sensing of surface ocean pH exploiting sea surface salinity satellite observations. In: Proceedings of IGARSS 2015 (International Geoscience and Remote Sensing Symposium), Milano, Italy, (July 27–31, 2015).
Sabia, R., Olmedo, E., Turiel, A., Martinez, J., Alvera-Azcarate, A., 2018. SMOS satellite inference of alkalinity over Mediterranean Basin. In: IGARSS 2018–2018 IEEE International Geoscience and Remote Sensing Symposium, Valencia, 2018, pp. 1519–1522. https://doi.org/10.1109/IGARSS.2018.8518407.
Salisbury, J.E., Jönsson, B.F., 2018. Rapid warming and salinity changes in the Gulf of Maine alter surface ocean carbonate parameters and hide ocean acidification. Biogeochemistry 141, 401–418. https://doi.org/10.1007/s10533-018-0505-3.
Salisbury, J., Vandemark, D., Campbell, J., Hunt, C., Wisser, D., Reul, N., Chapron, B., 2011. Spatial and temporal coherence between Amazon River discharge, salinity, and light absorption by colored organic carbon in western tropical Atlantic surface waters. J. Geophys. Res. 116, C00H02. https://doi.org/10.1029/2011JC006989.
Salisbury, J., Vandemark, D., Jönsson, B., Balch, W., Chakraborty, S., Lohrenz, S., Chapron, B., Hales, B., Mannino, A., Mathis, J.T., Reul, N., Signorini, S.R., Wanninkhof, R., Yates, K.K., 2015. How can present and future satellite missions support scientific studies that address ocean acidification? Oceanography 28 (2), 108–121.
Schiller, A., Oke, P.R., 2015. Dynamics of ocean surface mixed layer variability in the Indian Ocean. J. Geophys. Res. Oceans 120, 4162–4186.
Schlundt, M., Brandt, P., Dengler, M., Hummels, R., Fischer, T., Bumke, K., Krahmann, G., Karstensen, J., 2014. Mixed layer heat and salinity budgets during the onset of the 2011 Atlantic cold tongue. J. Geophys. Res. Oceans 119, 7882–7910.
Schmitt, R.W., 2008. Salinity and the global water cycle. Oceanography 21 (1), 12–19. https://doi.org/10.5670/oceanog.2008.63.
Sengupta, D., Raj, G.N.B., Ravichandran, M., Lekha, J.S., Papa, F., 2016. Near-surface salinity and stratification in the North Bay of Bengal from moored observations. Geophys. Res. Lett. 43 (9), 4448–4456. https://doi.org/10.1002/2016GL068339.
Shinoda, T., Jensen, T.G., Flatau, M., Chen, S., Han, W., Wang, C., 2013. Large-scale oceanic variability associated with the Madden-Julian oscillation during the CINDY/DYNAMO field campaign from satellite observations. Remote Sens. 5, 2072–2092.
Shutko, A.M., Liberman, B.M., Chuhray, G.I., 1982. On the influence of dielectric property variations on the microwave radiation of a water surface. IEEE J. Ocean. Eng. 7, 35–39. https://doi.org/10.1109/JOE.1982.1145508.
Siedler, G., Church, J., Gould, J., 2001. Ocean Circulation and Climate: Observing and Modelling the Global Ocean. Academic Press, London.
Singh, A., Delcroix, T., Cravatte, S., 2011. Contrasting the flavors of El Niño-Southern Oscillation using sea surface salinity observations. J. Geophys. Res. 116, C06016. https://doi.org/10.1029/2010JC006862.
Sirounian, V., 1968. Effect of temperature, angle of observation, salinity, and thin ice on the microwave emission of water. J. Geophys. Res. 73, 4481–4486.
Skliris, N., Marsh, R., Josey, S.A., et al., 2014. Salinity changes in the World Ocean since 1950 in relation to changing surface freshwater fluxes. Clim. Dyn. 43, 709–736. https://doi.org/10.1007/s00382-014-2131-7.
Skou, N., Hoffman-Bang, D., 2005. L-band radiometers measuring salinity from space: atmospheric propagation effects. IEEE Trans. Geosci. Remote Sens. 43 (10), 2210–2217.
Smith, S.R., Rolph, J.J., Briggs, K., Bourassa, M.A., 2009. Quality-controlled Underway Oceanographic and Meteorological Data from the Center for Ocean-atmospheric Predictions Center (COAPS) - Shipboard Automated Meteorological and Oceanographic System (SAMOS). National Oceanographic Data Center, NOAAhttps://doi.org/10.7289/v5qj7f8r. Dataset.
SMOS-Ocean Expert Support Laboratories, 2016. SMOS L2 OS Algorithm Theoretical Baseline Document, SO-TN-ARG-GS-0007. available at. https://earth.esa.int/documents/10174/1854519/SMOS_L2OS-ATBD.
Soldo, Y., 2013. Optimisation de la reconstruction d'image pour SMOS et SMOS-NEXT. PhD from. Université Toulouse III Paul Sabatier, France.
Spurgeon and SMOS-Ocean Expert Support Laboratories, 2017. L2OS v662 Reprocessing 1063 Report, SO-RP-ARG-GS-0109. available on 1064 https://earth.esa.int/documents/10174/477987/SMOS-Level-2-Ocean-Salinity-v662-1065Reprocessing-Report/3587ea20-45d1-49a5-a6ca-084d1bf988b6?version=1.4.
Stoffelen, A., 1998. Toward the true near-surface wind speed: error modeling and calibration using triple collocation. J. Geophys. Res. 103, 7755–7766. https://doi.org/10.1029/97JC03180.
Stogryn, A., 1971. Equations for calculating the dielectric constant of saline water. IEEE Trans. Microw. Theory Techn. 19 (8), 733–736.
Stogryn, A.P., Bull, H.T., Rubayi, K., Iravanchy, S., 1995. The Microwave Permittivity of Sea and Fresh Water. GenCorp Aerojet, Azusa, CA, USA (Tech. Rep).
Su, H., Wu, X., Yan, X.-H., Kidwell, A., 2015. Estimation of subsurface temperature anomaly in the Indian Ocean during recent global surface warming Hiatus from satellite measurements: a support vector machine approach. Remote Sens. Environ. 160, 63–71. https://doi.org/10.1016/j.rse.2015.01.001.
Subrahmanyam, B., Murty, V.S.N., Heffner, D.M., 2011. Sea surface salinity variability in the tropical Indian ocean. Remote Sens. Environ. 115, 944–956.
Sun, Q., Tang, D., Wang, S., 2012. Remote-sensing observations relevant to ocean acidification. Int. J. Remote Sens. 33 (23), 7542–7558. https://doi.org/10.1080/01431161.2012.685978.
Supply, A., Boutin, J., Vergely, J.-L., et al., 2018. Precipitation estimates from SMOS sea-surface salinity. Q. J. R. Meteorol. Soc. 144 (Suppl. 1), 103–119.
Swift, C.T., 1974. Microwave radiometer measurements of the Cape Cod canal. Radio Sci. 9 (7), 641–653.
Swift, C.T., McIntosh, R.E., 1983. Considerations for microwave remote sensing of ocean surface salinity. IEEE Trans. Geosci. Remote Sens. 21, 480–491.
Tang, W., Yueh, S.H., Fore, A.G., Hayashi, A., 2014a. Validation of Aquarius sea surface salinity with *in situ* measurements from Argo floats and moored buoys. J. Geophys. Res. Oceans 119, 6171–6189. https://doi.org/10.1002/2014JC010101.
Tang, W., Yueh, S.H., Fore, A., Hayashi, A., Lee, T., Lagerloef, G., 2014b. Uncertainty of Aquarius sea surface salinity retrieved under rainy conditions and its implication on the water cycle study. J. Geophys. Res., Oceans 119, 4821–4839. https://doi.org/10.1002/2014JC009834.
Tang, W.Q., Yueh, S.H., Hayashi, A., Fore, A.G., Jones, W.L., Santos-Garcia, A., Jacob, M.M., 2015. Rain-induced near surface salinity stratification and rain roughness correction for Aquarius SSS retrieval. IEEE Journal Of Selected Topics In Applied Earth Observations And Remote Sensing 8 (12), 5474–5484.
Tang, W., Yueh, S., Yang, D., Fore, A., Hayashi, A., Lee, T., Fournier, S., Holt, B., 2018. The potential and challenges of using soil moisture active passive (SMAP) sea surface salinity to monitor Arctic Ocean freshwater changes. Remote Sens. 10, 869. https://doi.org/10.3390/rs10060869.
Tenerelli, J., Reul, N., Mouche, A., Chapron, B., 2008. Earth-viewing L-band radiometer sensing of sea surface scattered celestial sky radiation - part I: general characteristics. IEEE-Transactions on geoscience and remote sensing 46 (3), 659–674.
Thébault, et al., 2015. International geomagnetic reference field: the 12th generation. Earth, Planets and Space 67, 79. https://doi.org/10.1186/s40623-015-0228-9.
Thomann, G.C., 1976. Experimental results of the remote sensing of sea-surface salinity at 21 cm wavelength. IEEE Trans. Geosci.Electronics 14, 198–214.
Toyoda, T., Fujii, Y., Kuragano, T., Matthews, J.P., Abe, H., Ebuchi, N., Usui, N., Ogawa, K., Kamachi, M., 2015. Improvements to a global ocean data assimilation system through the incorporation of Aquarius surface salinity data. Q. J. Roy. Meteor. Soc. 141 (692), 2750–2759. https://doi.org/10.1002/qj.2561.
Tranchant, B., Remy, E., Greiner, E., Legalloudec, O., 2019. Data assimilation of Soil Moisture and Ocean Salinity (SMOS) observations into the Mercator Ocean operational system: focus on the El Niño 2015 event. Ocean Sci. 15, 543–563. https://doi.org/10.5194/os-15-543-2019.
Treasure, A.M., Roquet, F., Ansorge, I.J., Bester, M.N., Boehme, L., Bornemann, H., Charrassin, J.-B., Chevallier, D., Costa, D.P., Fedak, M.A., Guinet, C., Hammill, M.O., Harcourt, R.G., Hindell, M.A., Kovacs, K.M., Lea, M.-A., Lovell, P., Lowther, A.D., Lydersen, C., McIntyre, T., McMahon, C.R., Muelbert, M.M.C., Nicholls, K., Picard, B., Reverdin, G., Trites, A.W., Williams, G.D., de Bruyn, P.J.N., 2017. Marine mammals exploring the oceans pole to pole: a review of the MEOP consortium. Oceanography 30 (2), 132–138. https://doi.org/10.5670/oceanog.2017.234.
Turk, D., Zappa, C.J., Meinen, C.S., Christian, J.R., Ho, D.T., Dickson, A.G., McGillis, W.R., 2010. Rain impacts on CO2 exchange in the western equatorial Pacific Ocean. Geophys. Res. Lett. 37 (23).
Tzortzi, E., Srokosz, M., Gommenginger, C., Josey, S.A., 2016. Spatial and temporal scales of variability in tropical Atlantic Sea surface salinity from the SMOS and Aquarius satellite missions. Remote Sens. Environ. 180, 418–430. https://doi.org/10.1016/j.rse.2016.02.008.
Ulaby, F.T., Moore, R.K., Fung, A.K., 1981. Microwave remote sensing: active and passive. In: Volume 1 - Microwave Remote Sensing Fundamentals and Radiometry. Addison-Wesley Publishing company, Reading, Massachusetts.
Ulaby, F., Moore, R., Fung, A., 1986. Microwave Remote Sensing: Active and Passive, From Theory to Applications. vol. III Book-Mart, North Bergen, N. J 2162 pp.
Umbert, M., Guimbard, S., Lagerloef, G., Thompson, L., Portabella, M., Ballabrera-Poy, J., Turiel, A., 2015. Detecting the surface salinity signature of Gulf Stream cold-core rings in Aquarius synergistic products. J. Geophys. Res. Oceans 120, 859–874.
Vall-llossera, M., Miranda, J., Camps, A., Villarano, R., 2003. Sea surface emissivity modeling at L-band: an inter-comparison study. In: Proc. 1st Results Workshop EuroSTARRS WISE LOSAC, 2003, pp. 143–153 (ESA SP-525).
Vergely, J.-L., Waldteufel, P., Boutin, J., Yin, X., Spurgeon, P., Delwart, S., 2014. New total electron content retrieval improves SMOS sea surface salinity. J. Geophys. Res. Oceans 119, 7295–7307.
Vernieres, G., Kovach, R., Keppenne, C., Akella, S., Brucker, L., Dinnat, E., 2014. The impact of the assimilation of Aquarius sea surface salinity data in the GEOS ocean data assimilation system. J. Geophys. Res. Oceans 119, 6974–6987. https://doi.org/10.1002/2014JC010006.
Vine, Le, M, D., de Matthaeis, P., Ruf, C.S., Chen, D.D., 2014. Aquarius RFI detection and mitigation algorithm: assessment and examples. IEEE Trans. Geosci. Remote Sens. 52 (8), 4574–4584.
Vinogradova, N.T., 2018. Synergistic use of satellite and *in situ* observations for production of multi-platform ocean state estimates for climate research. In: NASA Hyperwall Lecture Series, 2018.
Vinogradova, N.T., et al., 2019. Satellite salinity observing system: recent discoveries and the way forward. In: Frontiers, (under review).
Vinogradova, N.T., Ponte, R.M., 2012. Assessing temporal aliasing in satellite-based surface salinity measurements. J. Atmos. Ocean. Tech. 29 (9), 1391–1400. https://doi.org/10.1175/JTECH-D-11-00055.
Vinogradova, N.T., Ponte, R.M., 2013a. Small-scale variability in sea surface salinity and implications for satellite-derived measurements. J. Atmos. Ocean. Tech. 30 (11), 2689–2694. https://doi.org/10.1175/JTECH-D-13-00110.1.
Vinogradova, N.T., Ponte, R.M., 2013b. Clarifying the link between surface salinity and freshwater fluxes on monthly to interannual time scales. J. Geophys. Res. Oceans 118, 3190–3201. https://doi.org/10.1002/jgrc.20200.
Vinogradova, N.T., Ponte, R.M., 2017. In search of fingerprints of the recent intensification of the ocean water cycle. J. Clim. 30, 5513–5528. https://doi.org/10.1175/JCLI-D-16-0626.1.
Vinogradova, N.T., Ponte, R.M., Fukumori, I., Wang, O., 2014. Estimating satellite salinity errors for assimilation of Aquarius and SMOS data into climate models. J. Geophys. Res.-Oceans 119 (8), 4732–4744. https://doi.org/10.1002/2014JC009906.
Waldteufel, P., Floury, N., Dinnat, E.P., Caudal, G., 2004. Ionospheric effect for L-band 2-

D interferometric radiometry. IEEE Trans. Geosci. Remote Sens. 42 (1), 105–118.
Webster, W.J., Wilheit, T.T., Ross, D.B., Gloersen, P., 1976. Spectral characteristics of the microwave emission from a wind-driven covered sea. J. Geophys. Res. 81 (18), 3095–3099.
Wentz, F., Meissner, T., 2016. Atmospheric absorption model for dry air and water vapor at microwave frequencies below 100 GHz derived from spaceborne radiometer observations. Radio Sci. 51, 381–391.
Wilson, W.J., Yueh, S.H., Dinardo, S., Yi, Chao, Li, Fuk, 2003. Precision ocean salinity measurements using the passive active L/S-band aircraft instrument. In: Geoscience and Remote Sensing Symposium, 2003. IGARSS '03. Proceedings. 2003 IEEE International 4. pp. 2792–2794.
Wilson, W.J., Yueh, S.H., Dinardo, S.J., Li, F.K., 2004. High-stability L-band radiometer measurements of saltwater. IEEE Trans. Geosci. And Remote Sens. 42 (9), 1829–1835.
Wurl, O., Landing, W.M., Mustaffa, N.I.H., Ribas-Ribas, M., Witte, C.R., Zappa, C.J., 2019. The ocean's skin layer in the tropics. Journal of Geophysical Research: Oceans 124. https://doi.org/10.1029/2018JC014021.
Wust, G., 1936. Oberflachensalzgehalt, Verdunstung und Niederschlag auf dem Weltmeere. Landerkundliche Forschung 347–359 Festschrift Norbert Krebs.
Wyrtki, K., 1981. An estimate of equatorial upwelling in the Pacific. J. Phys. Oceanogr. 11, 1205–1214.
Yin, X., Boutin, J., Martin, N., Spurgeon, P., 2012. Optimization of L-band sea surface emissivity models deduced from SMOS data. IEEE Trans. Geosci. Remote Sens. 50 (5), 1414–1426.
Yin, X., Boutin, J., Reverdin, G., Lee, T., Arnault, S., Martin, N., 2014. SMOS sea surface salinity signals of tropical instability waves. J. Geophys. Res. Oceans 119, 7811–7826.
Yin, X., Boutin, J., Dinnat, E., Song, Q., Martin, A., 2016. Roughness and foam signature on SMOS-MIRAS brightness temperatures: a semi-theoretical approach. Remote Sens. Environ. 180, 221–233.
Yu, L., 2014. Coherent evidence from Aquarius and Argo for the existence of a shallow low-salinity convergence zone beneath the Pacific ITCZ. J. Geophys. Res.-Oceans 119 (11), 7625–7644. https://doi.org/10.1002/2014JC010030.
Yu, L., 2015. Sea-surface salinity fronts and associated salinity-minimum zones in the tropical ocean. Journal of Geophysical Research: Oceans 120 (6), 4205–4225.
Yu, L., Jin, X., Josey, S.A., Lee, T., Kumar, A., Wen, C., Xue, Y., 2017. The global ocean water cycle in atmospheric reanalysis, satellite, and ocean salinity. J. Clim. 30, 3829–3852. https://doi.org/10.1175/JCLI-D-16-0479.1.
Yu, L., Jin, X., Liu, H., 2018. Poleward shift in ventilation of the North Atlantic subtropical underwater. Geophys. Res. Lett. 45, 258–266. https://doi.org/10.1002/2017GL075772.
Yuan, X., Salama, M.S., Su, Z., 2018. An observational perspective of sea surface salinity in the southwestern Indian Ocean and its role in the South Asia summer monsoon. Remote Sens. 10, 1930.
Yueh, S., 1997. Modeling of wind direction signals in polarimetric sea surface brightness temperatures. IEEE Trans. Geosci. Remote Sens. 35 (6), 1400–1418.
Yueh, S.H., 2000. Estimates of Faraday rotation with passive microwave polarimetry for microwave remote sensing of Earth surfaces. IEEE Trans. Geosci. Remote Sens. 38, 2434–2438.
Yueh, S.H., West, R., Wilson, W.J., Li, F.K., Njoku, E.G., Rahmat-Samii, Y., 2001. Error sources and feasibility for microwave remote sensing of ocean salinity. IEEE Trans. Geosci. Remote Sens. 39 (5), 1049–1060.
Yueh, S.H., Dinardo, S., Fore, A., Li, F., 2010. Passive and active L-band microwave observations and modeling of ocean surface winds. IEEE Trans. Geosci. and Remote Sensing 48 (8), 3087–3100.
Yueh, S., Tang, W., Fore, A., Neumann, G., Hayashi, A., Freedman, A., Lagerloef, G., 2013. L-band passive and active microwave geophysical model functions of ocean surface winds and applications to Aquarius retrieval. IEEE Trans. Geosci. Remote Sens. 51 (9), 4619–4632.
Yueh, S., Tang, W., Fore, A., Hayashi, A., Song, Y.T., Lagerloef, G., 2014. Aquarius geophysical model function and combined active passive algorithm for ocean surface salinity and wind retrieval. J. Geophys. Res. Oceans 119, 5360–5379.
Yueh, S., Tang, W., Fore, A.G., Hayashi, A., 2015. Impact of ocean wave height on L-band passive and active microwave observation of sea surfaces. IEEE Journal of Selected Topics in Applied Earth Observations and Remote Sensing 8 (12), 5491–5499.
Zhang, Y., Du, Y., Zheng, S., Yang, Y., Cheng, X., 2013. Impact of Indian Ocean dipole on the salinity budget in the equatorial Indian Ocean. J Geophys Res Oceans 118, 4911–4923.
Zhou, Y., Lang, R.H., Dinnat, E.P., Le Vine, D.M., 2017. L-band model function of the dielectric constant of seawater. IEEE TGRS 55 (12).
Zhu, J., Huang, B., Zhang, R.-H., Hu, Z.-Z., Kumar, A., Balmaseda, M.A., et al., 2014. Salinity anomaly as a trigger for ENSO events. Sci. Rep. 4.
Zika, J.D., Skliris, N., Nurser, A.J., Josey, S.A., Mudryk, L., Laliberté, F., Marsh, R., 2015. Maintenance and broadening of the ocean's salinity distribution by the water cycle. J. Clim. 28, 9550–9560. https://doi.org/10.1175/JCLI-D-15-0273.1.